

**SPRING TO SUMMER TRANSITIONS OF OZONE AND ITS PRECURSORS  
OVER NORTH AMERICA AND PHOTOCHEMISTRY OVER ANTARCTICA**

A Dissertation  
Presented to  
The Academic Faculty

By

Yunsoo Choi

In Partial Fulfillment  
Of the Requirements for the Degree  
Doctor of Philosophy in the School of Earth and Atmospheric Sciences

Georgia Institute of Technology

August 2007

Spring to Summer Transitions of Ozone and Its Precursors over North America and  
Photochemistry over Antarctica

Approved by:

Dr. Yuhang Wang, Advisor  
School of Earth and Atmospheric  
Sciences  
*Georgia Institute of Technology*

Dr. Robert Black  
School of Earth and Atmospheric  
Sciences  
*Georgia Institute of Technology*

Dr. Derek Cunnold  
School of Earth and Atmospheric  
Sciences  
*Georgia Institute of Technology*

Dr. Athanasios Nenes  
School of Earth and Atmospheric  
Sciences  
*Georgia Institute of Technology*

Dr. Armistread (Ted) Russell  
School of Civil and Environmental  
Engineering  
*Georgia Institute of Technology*

Date Approved: June 18, 2007

*To my wife, Kyungim*

## ACKNOWLEDGEMENTS

I deeply appreciate the tremendous support that I have received from many individuals during the process of obtaining my Ph.D. I thank my advisor, Dr. Yuhang Wang, for his long-term support and guidance with his scientific enthusiasm. My group members, Tao Zeng, Changsub Shim, Sangil Lee, Chun Zhao, Xueyuan Deng, Burton Gray, Bo Yao, and Shekhar Chandra, gave me great encouragement and valuable suggestions. I thank Dr. Robert Black, Dr. Derek Cunnold, Dr. Athanasios Nenes, and Dr. Armistead Russell for taking their time to serve on my thesis committee and for helpful discussions. My research has also been assisted by Dr. Derek Cunnold, Dr. Eun-Su Yang, Qing Yang, Dr. Randall Martin, Dr. Kelly Chance, Dr. Thomas Kurosu, Dr. Annmarie Eldering, Dr. Ming Luo, Dr. Eric Bucsela, Dr. Jim Gleason, Dr. Valeri Thouret, Robert Yantosca, Dr. Daniel Jacob, Dr. Mian Chin, Dr. Dale Allen, and many others. I also thank numerous former and current colleagues and friends at EAS Georgia Tech, particularly, Dr. Eun-Su Yang, Dr. Chulhan Song, Gill-Ran Jung, Saewung Kim, and Hyungjin Choi. I thank Dr. Youngdo Won at Hanyang University, Dr. Donald Blake, Dr. Sherwood Rowland and Dr. Douglas Tobias at the University of California, Irvine, and Dr. Douglas Davis at Georgia Tech for leading me to the scientific field. Above all, I have been supported by the tremendous love of my family: my wife, Kyungim Oh, our first daughter, Lindsay Choi, twin sons, Wonyoung and Sawyoung Choi, and a baby son, Jinyoung Choi, my parents, my in-laws, my brothers, and my brothers- and sisters-in-law.

Finally, my deep appreciation goes to my church family for their spiritual encouragement and support throughout the completion of my study.

## TABLE OF CONTENTS

ACKNOWLEDGEMENTS	iv
LIST OF TABLES	x
LIST OF FIGURES	xi
LIST OF SYMBOLS AND ABBREVIATIONS	xvii
SUMMARY	xx
CHAPTER I INTRODUCTION	1
1.1 Motivation	1
1.2 Space-borne Measurements and Models	4
1.2.1 Tropospheric NO <sub>2</sub> column from GOME and OMI	4
1.2.2 Total CO column from MOPITT	6
1.2.3 Tropospheric O <sub>3</sub> from TOMS-SAGE II and OMI-MLS	7
1.2.4 3-D Global chemical transport model, GEOS-CHEM	9
1.2.5 3-D Regional chemical transport model, REAM	10
1.2.5.1 Model framework	10
1.2.5.2 Model components	11
1.2.5.3 Advection and convection	12
1.2.5.4 Diffusion	13
1.2.5.5 Chemical and photolysis reactions	13
1.2.5.6 Dry and wet depositions	13
1.2.5.7 Emissions	14
1.2.5.8 Lightning NO <sub>x</sub> parameterization	15

1.3 Scope of This Dissertation	17
CHAPTER II EVIDENCE OF LIGHTNING NO <sub>x</sub> AND CONVECTIVE TRANSPORT OF POLLUTANTS IN SATELLITE OBSERVATIONS OVER NORTH AMERICA	19
2.1 Introduction	19
2.2 GOME and MOPITT Retrievals	20
2.3 Model Description	21
2.4 Results and Discussion	22
2.4.1 Is lightning NO <sub>x</sub> evident in GOME observations?	22
2.4.2 Signals of convective transport in MOPITT CO observations	24
2.5 Conclusions	29
CHAPTER III MODEL ANALYSIS OF SPRINGTIME TRANSITION OF NO <sub>2</sub> , CO, AND O <sub>3</sub> OVER NORTH AMERICA ON THE BASIS OF IN SITU AND SATELLITE MEASUREMENTS	31
3.1 Introduction	31
3.2 In situ and Satellite Measurements	34
3.2.1 Surface measurements	34
3.2.1.1 EPA AIRNow network	34
3.2.1.2 SEARCH network	35
3.2.2 Aircraft Observations	35
3.2.2.1 MOZAIC	35
3.2.2.2 TOPSE	36
3.2.3 Ozonesondes	36
3.2.4 Satellite retrievals	37

3.3 Model Descriptions	40
3.3.1 Regional chEmical trAnsport Model (REAM)	40
3.3.1.1 General description	40
3.3.1.2 Lightning NO <sub>x</sub> parameterization	41
3.3.2 Global Earth Observing System (GEOS)-CHEM	43
3.4 Seasonal Transitions of NO <sub>x</sub> , CO and O <sub>3</sub>	44
3.4.1 Nitrogen Oxides (NO <sub>x</sub> =NO+NO <sub>2</sub> )	44
3.4.1.1 Time series of SEARCH NO	44
3.4.1.2 GOME tropospheric NO <sub>2</sub> column	44
3.4.1.3 Optimization of fossil fuel NO <sub>x</sub> emissions	50
3.4.2 Carbon Monoxide	52
3.4.2.1 Time series of SEARCH CO	52
3.4.2.2 MOPITT CO	52
3.4.3 Ozone	58
3.4.3.1 Time series of SEARCH surface O <sub>3</sub>	58
3.4.3.2 Monthly mean EPA AIRNow O <sub>3</sub>	58
3.4.3.3 Mixing depth and surface O <sub>3</sub>	61
3.4.3.4 MOZAIC O <sub>3</sub>	64
3.4.3.5 Ozonesonde measurements	69
3.4.3.6 TOMS-SAGE II tropospheric column O <sub>3</sub>	70
3.4.4 Pollutant Export/import Fluxes and Budget Calculation	72
3.4.4.1 Longitudinal pollutant fluxes	72
3.4.4.2 Net fluxes in the free troposphere and boundary layer	76

3.5 Conclusions	79
CHAPTER IV EVIDENCE OF SPRING-SUMMER NORTHWARD MIGRATION OF HIGH O <sub>3</sub> OVER THE WESTERN NORTH ATLANTIC	83
4.1 Introduction	83
4.2 Satellite Measurements	84
4.3 Model Description	85
4.4 Results and Discussion	86
4.4.1 OMI-MLS tropospheric O <sub>3</sub>	86
4.4.2 OMI tropospheric column NO <sub>2</sub>	90
4.4.3 TES UT O <sub>3</sub> and CO measurements	92
4.5 Conclusions	94
CHAPTER V LATE-SPRING INCREASE OF TRANS-PACIFIC POLLUTION TRANSPORT IN THE UPPER TROPOSPHERE	96
5.1 Introduction	96
5.2 Results and Discussion	97
5.3 Conclusions	107
CHAPTER VI ASSESSING THE PHOTOCHEMICAL IMPACT OF SNOW NO <sub>x</sub> EMISSIONS OVER ANTARCTICA DURING ANTICI 2003	109
6.1 Introduction	109
6.2 3-D Model Descriptions and 1-D Model Setup	110
6.3. Snow NO <sub>x</sub> Emission Flux Parameterization	112
6.3.1 Effects of turbulence on boundary layer height	113
6.3.2 Snow NO <sub>x</sub> emission flux estimation and parameterization	116
6.4 Evaluations with Surface Reactive Nitrogen Measurements at SP	121
6.5 Comparison with Balloon and Aircraft NO Measurements	131



6.6 Conclusions	139
CHAPTER VII CONCLUSIONS	143
REFERENCES	147

## LIST OF TABLES

Table 3.1	Monthly North America (20 - 62°N) fossil fuel NO <sub>x</sub> emissions (Tg N month <sup>-1</sup> )	51
Table 3.2a	The import and export fluxes of tracers in the lower and middle troposphere (<7 km) over North America (20 - 62°N, Gmol day <sup>-1</sup> )	77
Table 3.2b	The same as table 3.2a, but in the boundary layer (<2.5 km)	77

## LIST OF FIGURES

Figure 2.1	GOME retrieved and the corresponding REAM simulated tropospheric NO <sub>2</sub> vertical column on April 20, 21, 27, and 29, 2000. GOME columns less than the spectral fitting uncertainties are not included. Simulations with and without lightning NO <sub>x</sub> production are shown. The last column shows the simulated lightning NO <sub>2</sub> enhancements.	23
Figure 2.2	Scattering weights under clear and cloudy sky conditions for the standard model NO <sub>2</sub> simulation on April 27 over the grid box indicated by the black circle in Figure 1.1. Also shown, as a function of pressure is the simulated enhancement of NO <sub>2</sub> due to lightning NO <sub>x</sub> production. The scattering weight represents the sensitivity of backscattering radiance measured by GOME to NO <sub>2</sub> concentrations at a given level.	25
Figure 2.3	Same as Figure 1 but for MOPITT retrieved and REAM simulated CO column on April 20, 21, and 27, 2000. The model results with and without convective transport have been processed with the MOPITT averaging kernel.	27
Figure 2.4	Simulated CO concentrations with and without convective transport as a function of pressure on April 27 over the grid box indicated by the orange circle in Figure 2.3.	28
Figure 3.1	Daily averaged observed and simulated NO mixing ratios (ppbv) during the afternoon (1300-1700, LT) at four SEARCH surface sites: Centerville (CTR), Oak Grove (OAK), Outlying Landing Field #8 (OLF), and Yorkville (YRK). Black solid lines are for the SEARCH measurements, and red lines are for the REAM results.	45
Figure 3.2	Monthly mean tropospheric NO <sub>2</sub> vertical columns (in molecules cm <sup>-2</sup> ) during February-May 2000 from the GOME retrievals using REAM-derived shape factor (first column), the REAM model (second), GOME retrievals using GEOS-CHEM-derived shape factor (third), and the GEOS-CHEM model (last). More details are described in the text. The model results are obtained by averaging NO <sub>2</sub> data for satellite overpass time period (1000-1200, LT).	47
Figure 3.3	Monthly mean contributions of lightning production, convection, and soil emissions to tropospheric NO <sub>2</sub> vertical columns (in molecules cm <sup>-2</sup> )	49

Figure 3.4	Same as Figure 3.1 but for hourly observed and REAM simulated CO mixing ratios at four surface SEARCH sites.	53
Figure 3.5	The monthly mean cross sections of the MOPITT CO concentrations (pptv) (left column) along TOPSE aircraft tracks, corresponding TOPSE CO concentrations processed with the MOPITT averaging kernel (middle), and TOPSE CO observations (right). Data selection criteria are described in text.	54
Figure 3.6	Regional profiles by latitudes for MOPITT measurements and TOPSE-REAM results with and without AK processing. Region 1 covers the lower-latitude region of TOPSE aircraft campaign (latitude < 52°N, in the left column), region 2 covers the middle-latitude (52°N < latitude < 57°N, in the middle column), and region 3 covers the higher-latitude (latitude > 57°N, in the right column). The scaling of REAM results with TOPSE measurements is explained in text.	56
Figure 3.7	Mean CO columns (in molecules cm <sup>-2</sup> ) from MOPITT (left panel) during April-May of 2000, the corresponding REAM CO columns processed with MOPITT averaging kernel (middle), and the GEOS-CHEM CO columns processed with averaging kernel (right). Model results are sampled at MOPITT measurement time and location.	57
Figure 3.8	Same as Figure 3.4 but for surface O <sub>3</sub> . The black lines are SEARCH measurements and the red lines are REAM results.	59
Figure 3.9	Monthly mean afternoon (1300-1700, LT) surface O <sub>3</sub> concentration (ppbv) over the United States in February-May 2000. Shown are the EPA AIRNow observations (left column), the REAM simulation results (middle), and the GEOS-CHEM simulation results (right).	60
Figure 3.10	Average afternoon (1200-1600, LT) mixing depths over North America in March-May, 2000. The data used in REAM (left column) are simulated by MM5, and those used in GEOS-CHEM (right column) are simulated by GEOS-3.	62
Figure 3.11	The comparisons of averaged afternoon (1200-1600, LT) vertical profiles of CO and NO <sub>x</sub> concentrations from REAM and GEOS-CHEM models. Solid lines are for the REAM simulations, and dotted lines are for the GEOS-CHEM simulations.	63
Figure 3.12	O <sub>3</sub> concentration (ppbv) below 350 hPa from the MOZAIC measurements during February-May 2000 (left column) and the	

corresponding REAM results (right column). The REAM data for comparison with MOZAIC are sampled along MOZAIC aircraft tracks.	65
Figure 3.13 Same as Figure 3.12 but for 250-350 hPa. The O <sub>3</sub> data >200 ppbv from MOZAIC, and REAM are filtered out.	66
Figure 3.14 Observed and simulated O <sub>3</sub> monthly mean vertical profiles (ppbv) for six ozonesonde sites at 30-55°N in February-May, 2000. Solid lines are for the ozonesonde measurements, and dotted lines are for the corresponding REAM results. Error bars represent the measurement standard deviations.	67
Figure 3.15 Monthly mean tropospheric O <sub>3</sub> columns derived from TOMS total columns and SAGE II stratospheric columns (first column), the REAM standard simulation (second), the REAM sensitivity simulation without lightning NO <sub>x</sub> production (third), and the GEOS-CHEM simulation (last).	71
Figure 3.16 The longitudinal import and export fluxes of NO <sub>x</sub> , NO <sub>y</sub> , CO, and O <sub>3</sub> over North America in the troposphere as a function of latitude. The western and eastern boundaries are the same as depicted in Figure 3.15. The solid lines are for the export fluxes, and the dotted lines are for the import fluxes.	73
Figure 3.17 Same as Figure 3.16 but for altitude.	74
Figure 4.1 Monthly mean tropospheric O <sub>3</sub> columns from April to August 2005 derived from OMI-MLS satellite measurements (first column), REAM simulations (second column), O <sub>3</sub> produced due to lightning NO <sub>x</sub> production (third column), and O <sub>3</sub> produced due to surface emissions (last column).	87
Figure 4.2 Tropospheric O <sub>3</sub> columns measured by ozonesondes, derived from OMI-MLS, and simulated by REAM at Wallops Island from April to August 2005. Coincidence criteria for OMI-MLS derived column ozone are at ±3.0° longitude, ±2.5° latitude in the same day as the ozonesonde measurements. Ozonesonde data are obtained from the World Ozone and Ultraviolet Data Center (WOUDC).	89
Figure 4.3 Monthly mean tropospheric NO <sub>2</sub> columns during summer 2005 from OMI satellite measurements (first column), REAM simulations (second column), contributed by lightning production in the model (third column). Only OMI data with cloud fraction of	

	<40% are used. Corresponding model results are sample at the same time as the OMI measurements.	91
Figure 4.4	Monthly mean tropospheric O <sub>3</sub> concentrations at 300 hPa (250-350) for July and August 2005 from TES satellite measurements (first column), REAM (second) and difference between REAM and the model turning off lightning NO <sub>x</sub> production (third). Only TES O <sub>3</sub> data with a degree of freedom of >3.5 are used. Corresponding model results are sampled at the same time as the TES measurements.	93
Figure 5.1	Observed and REAM simulated monthly mean distributions of NO <sub>x</sub> from March to May 2000. The REAM data were sampled along the TOPSE flight tracks.	99
Figure 5.2	Same as Figure 5.1, but for CO, PAN, and O <sub>3</sub> in May. When constructing the observed O <sub>3</sub> distribution, we did not include measurements with mixing ratios > 110 ppbv to filter out the effect of stratospheric O <sub>3</sub> .	101
Figure 5.3	Observed correlations between O <sub>3</sub> and NO <sub>x</sub> grouped by CO mixing ratios (ppbv) in May. Only coincidental measurements of all three species above 4 km are included.	104
Figure 5.4	Observed monthly mean distribution of CFC-12 in May.	106
Figure 6.1	Observed and simulated daily boundary layer heights at SP during ANTICI 2003. Simulation results using the original and modified ETA MYJ turbulence schemes are shown. The vertical bar shows daily standard deviation. The maximum altitude measured by SODAR is 180 m.	114
Figure 6.2	Same as Figure 6.1, but for temperature and wind speed. “T” denotes temperature and “V” denotes wind speed.	115
Figure 6.3	1-D model derived daily snow NO <sub>x</sub> emissions, and observed and simulated temperature and wind speed at SP. The black line shows model derived snow NO <sub>x</sub> emissions. “T” denotes temperature (K) and “V” denotes wind speed (m s <sup>-1</sup> ).	118
Figure 6.4	Parameterized snow pack NO <sub>x</sub> emission flux as a function of temperature (K) at a wind speed of 5 m s <sup>-1</sup> and as a function of wind speed (m s <sup>-1</sup> ) at a temperature of 250 K.	120

Figure 6.5a	Observed and 1-D and 3-D model simulated near-surface NO mixing ratios at SP. In the second 3-D simulation, parameterized snow NO <sub>x</sub> emissions are increased by 30%.	122
Figure 6.5b	Simulated surface NO <sub>x</sub> mixing ratios (pptv) and wind at 1200 UT on November 25 and 30, 2003.	122
Figure 6.6	Same as Figure 6.5a, but for HNO <sub>3</sub> . In the first 1-D simulation, surface NO is specified as observed. In the second 1-D simulation, snow NO <sub>x</sub> emission parameterization is used. In the 3-D simulation, parameterized snow NO <sub>x</sub> emissions (Eq. (1)) are increased by 30%. The measurement accuracy of HNO <sub>3</sub> is 20% [Huey <i>et al.</i> 2004].	125
Figure 6.7a	Same as Figure 6.6, but for HNO <sub>4</sub> . The measurement accuracy of HNO <sub>4</sub> is 30%.	127
Figure 6.7b	Simulated chemical production, loss, turbulent diffusion transport, and dry deposition rates for HNO <sub>4</sub> near the surface (0-10 m) in the 1-D model.	127
Figure 6.8	1-D and 3-D model simulated mean vertical profiles of NO, HNO <sub>3</sub> , and HNO <sub>4</sub> during ANTICI 2003. In the first 1-D simulation, surface NO is specified as observed. In the second 1-D simulation, snow NO <sub>x</sub> emission parameterization is used.	130
Figure 6.9	Balloon measurements of NO profiles on December 17-28 and the corresponding model results. Horizontal bar shows the standard deviation. There are 6 profiles for December 21-23 and 21 profiles for December 17-20 and 25-28.	133
Figure 6.10a	Twin Otter observed and model simulated NO mixing ratios (pptv) at 20-60 m above the surface on December 4-6. Model results are sampled along flight tracks at the time of measurements.	134
Figure 6.10b	Twin Otter observed and model simulated vertical distributions of NO on December 4-6. Model results are sampled along flight tracks at the time of measurements.	134
Figure 6.11	Simulated monthly mean near-surface HNO <sub>3</sub> fluxes for December 2003.	137
Figure 6.12	Simulated mean surface NO <sub>x</sub> and OH concentrations during ANTICI 2003.	137

Figure 6.13a Simulated cross section of OH concentrations ( $10^6$  molec  $\text{cm}^{-3}$ ) along the 90°W-90°E meridian during ANTICI 2003. 138

Figure 6.13b Simulated depth (m) of the oxidizing canopy over Antarctica ( $[\text{OH}] > 3 \times 10^6$  molec  $\text{cm}^{-3}$ ) during ANTICI 2003. 138



## LIST OF SYMBOLS AND ABBREVIATIONS

AK	averaging kernel
AMF	air mass factor
ANTCI	Antarctic Tropospheric Chemistry Investigation
ARO	Atmospheric Research Observatory
ASDC	Atmospheric Science Data Center
AVHRR	Advanced Very High Resolution Radiometer
AWS	Automatic Weather Station
CAPE	convective available potential energy
CFCs	chlorofluorocarbons
CG	cloud-to-ground
CH <sub>3</sub> OOH	methyl hydroperoxide
CO	carbon monoxide
CTM	Chemical Transport Model
DAAC	Distributed Active Archive Center
DAO	Data Assimilation Office
DFS	degree of freedom
DOAS	Differential Optical Absorption Spectroscopy
ECC	electrochemical concentration cell
ECMWF	European Centre for Medium-Range Weather Forecasts
ERBS	Earth Radiation Budget Satellite
ERS-2	European Remote Sensing-2 (satellite)
FDDA	four-dimensional data assimilation
GEIA	Global Emissions Inventory Activity
GEOS-Chem	global Goddard Earth Observing System – Chemistry (model)
GEOS-3	GEOS assimilated meteorological fields
GES	Goddard Earth Sciences
GMAO	Global Modeling Assimilation Office
GOCART	Global Ozone Chemistry Aerosol Radiation and Transport
GOME	Global Ozone Monitoring Experiment
GOMECAT	GOME cloud retrieval algorithm
GSFC	Goddard Space Flight Center
Halon-1211	Bromochlorodifluoromethane
HANK	Regional Episodic Chemical Transport Model
HCHO	formaldehyde
HNO <sub>3</sub>	nitric acid
hPa	hecto Pascal
H <sub>2</sub> O <sub>2</sub>	hydrogen peroxide
IC	intracloud
INTEX-NA	intercontinental chemical transport experiment – North America
IPCC	Intergovernmental Panel on Climate Change
ISCAT	Investigation of Sulfur Chemistry in the Antarctic Troposphere
ITCT	Intercontinental Transport and Chemical Transformation

K	temperature
LAI	leaf area index
LIDORT	linear discrete ordinary radiative transfer
LT	Local Time
MDL	method detection limits
MLS	Microwave Limb Sounder
MOPITT	Measurement of Pollution in the Troposphere
MOZAIC	Measurement of Ozone and Water Vapor by Airbus In-Service Aircraft
MOZART	Model for OZone And Related chemical Tracers
MYJ	Mellor-Yamada-Janjic
NAPAP	National Acid Precipitation Assessment Program (NAPAP)
NCEP	National Center Environmental Prediction
NEI99	EPA 1999 National Emission Inventory
NLDN	National Lightning Detection Network
NMHC	non-methane hydrocarbon
NO	nitric oxide
NO <sub>2</sub>	nitrogen dioxide
NO <sub>x</sub>	nitrogen oxides (NO + NO <sub>2</sub> )
NO <sub>y</sub>	total reactive, oxidized nitrogen
OH	hydroxyl radical
O <sub>3</sub>	ozone
OMI	Ozone Monitoring Instrument
Pa	Pascal
PAN	peroxyacetyl nitrate
PBL	periodic boundary layer
PDF	probability distribution function
ppbv	parts per billion by volume
ppmv	parts per million by volume
pptv	parts per trillion by volume
PV	potential vorticity
REAM	Regional chEmical trAnsport Model
SAGE	Stratospheric Aerosol and Gas Experiment
SCIAMACHY	Scanning Imaging Absorption spectroMeter for Atmospheric CartographY
SEARCH	Southeastern Aerosol Research and Characterization Study
SODAR	Sound Detecting and Ranging
SONEX	SASS (Subsonic Assessment) Ozone and NO <sub>x</sub> Experiment
SP	South Pole
TES	Tropospheric Emission Spectrometer
TOA	top of the atmosphere
TOPSE	Tropospheric Ozone Production about the Spring Equinox
3-D	three-dimensional
TOMS	Total Ozone Mapping Spectrometer
UT	upper troposphere
VOCs	volatile organic compounds

WCB  
WOUDC

Warm Conveylor Belt  
World Ozone and Ultraviolet Data Center

## SUMMARY

The horizontal and vertical distributions of ozone and its precursors over North America during the spring and the summer are frequently determined by several factors: cloud convection, lightning  $\text{NO}_x$  production, mixing depth, and long-range transport. The critical factors that contribute to the spatial distribution of air pollutants are studied using the Regional chEmical trAnsport Model (REAM) with diverse satellite measurements as well as in-situ surface and aircraft measurements. Among the space-borne measurements, GOME and OMI  $\text{NO}_2$  column measurements show enhanced lightning  $\text{NO}_x$  over the continent and the western North Atlantic. Concurrent convective transport-causing CO column peaks and high CO enhancements in the upper troposphere (UT) over the ocean are shown from the modeling analysis of the CO column by MOPITT and UT CO by TES. Likewise, TOMS-SAGE II and OMI-MLS  $\text{O}_3$  column peaks and TES UT  $\text{O}_3$  enhancements due to convective outflow and lightning  $\text{NO}_x$  are also observed. Lightning  $\text{NO}_x$  production in REAM is much larger than that in GEOS-CHEM, resulting in better simulations of GOME  $\text{NO}_2$  columns over the western North Atlantic. Consequently, REAM simulates larger  $\text{O}_3$  increasing trends in better agreement with TOMS-SAGE II and OMI-MLS  $\text{O}_3$  columns over the southern United States and the western North Atlantic than GEOS-CHEM. Another factor, mixing depth, is a key parameter for the boundary layer structure of the model. Simulated spring to summer transitions of  $\text{O}_3$  and its precursors over North America indicate that the simulated boundary layer structure plays a key role in differentiating REAM from GEOS-CHEM. Large enhancements of columns and upper tropospheric  $\text{O}_3$  comparable to those over the eastern United States

are found over the western North Atlantic in the satellite measurements and REAM simulations. The  $O_3$  enhancement region migrates northward from the spring to the summer. A model analysis indicates that the northward shift is driven by  $O_3$  in the stratospheric flux, convective outflow and production from lightning  $NO_x$ . In addition, long-range transport affects the spatial distributions of air pollutants, particularly during the spring. During the late spring, large enhancements of  $NO_x$ , PAN,  $O_3$ , CO, CFCs, and Halon-1211 in UT are found over North America due to a surge of trans-Pacific pollutant transport from observations during the TOPSE 2000 experiment. The transition occurs later than that of the typical low-altitude trans-Pacific transport, which peaks around March or April.

Surface and aircraft measurements show a large amount of reactive nitrogen tracers over the Antarctic plateau during the summer. These enhanced measurements are investigated, and their photochemical impact is assessed by 1-D CTM and 3-D CTM, REAM. The 1-D model and REAM reasonably simulate the surface measurements of NO,  $HNO_3$ ,  $HNO_4$ , and balloon NO measurements at the South Pole. However, compared with the Twin Otter NO measurements, REAM underestimates NO concentrations over plateau regions because parameterization based on surface measurements at the South Pole underestimates emissions in higher-elevation plateau regions. After all, around 50% of reactive nitrogen is scavenged by deposition, and the other is lost by transport. Thus, a shallow but highly active oxidizing canopy surrounds the Antarctic plateau due to snow  $NO_x$  emissions.

# CHAPTER I

## INTRODUCTION

### 1.1 Motivation

North America is a large source of  $O_3$ , aerosols, and their precursors in the Northern Hemisphere, which results in air pollution and adversely affects climate [IPCC, 2001]. Well-established as a typical climate issue, ozone in the UT functions as an efficient greenhouse gas, particularly in the mid-latitude Northern Hemisphere [Lacis *et al.*, 1990; Mickley *et al.*, 2004]. A critical aspect of determining air pollution caused by  $O_3$  and its precursors and their impact on climate is to better constrain their horizontal and vertical distributions. The spatial distributions of  $O_3$  and its precursors during the spring and the summer are affected by several factors: convection, lightning  $NO_x$  production, mixing depth, long-range transport, and their associated chemistry. Among these factors, cloud convection, along with the warm conveyor belt (WCB), is a major pathway for the outflow of North American pollution [Li *et al.*, 2005]. With cloud convection, lightning  $NO_x$  production is a dominant factor for  $O_3$  production in the UT over North America during the summer [Li *et al.*, 2005; Cooper *et al.*, 2006]. From space-borne measurements, lightning  $NO_2$  signals are evident in the Global Ozone Monitoring Experiment (GOME) [Richter and Burrows, 2002] and the Scanning Imaging Absorption spectroMeter for Atmospheric CartographY (SCIAMACHY) [Martin *et al.*, 2006]. Martin *et al.* [2006] and Hudman *et al.* [2007] quadrupled the northern mid-latitude lightning  $NO_x$  emissions in the global 3-D CTM, the Goddard Earth Observing System-CHEMistry (GEOS-CHEM) to reproduce observed lightning-caused  $NO_2$

enhancements over North America. In the model, simulating plausible lightning  $\text{NO}_x$  production consistent with in-situ and satellite observed lightning occurrence is still difficult. Another factor that affects the spatial distributions of air pollutants, the mixing depth, changes rapidly as the season advances towards the summer [Holzworth, 1964, 1967]. Since  $\text{O}_3$  concentrations over the surface are sensitive to uncertainties in the mixing depth [Rao *et al.*, 1994; Sistla *et al.*, 1996], a reliable mixing depth is critical for reasonable model performance [Berman *et al.*, 1999]. Long-range transport also affects the spatial distributions of air pollutants. Increasing pollution from Asia, driven by rapid regional economic growth, affects  $\text{O}_3$  concentration in the United States [Bernsen *et al.*, 1999; Jacob *et al.*, 1999]. Due to the subsidence of the trans-Pacific transported high  $\text{O}_3$ , the National Ambient Air Quality Standard could be significantly exceeded at California mountain sites [Hudman *et al.*, 2004].

Thus, it is imperative that a three-dimensional regional chemical transport model (CTM) be used with higher temporal and spatial resolutions that incorporate detailed cloud convection, an observation-constraint lightning scheme, regional scale mixing depth, and increased vertical resolution. Various regional and global 3-D CTM's [McKeen *et al.*, 1991; Brasseur *et al.*, 1998, Wang *et al.*, 1998; Lawrence *et al.*, 1999; Levy *et al.*, 1999; Hess *et al.*, 2000; Bey *et al.*, 2001, Song and Carmichael, 2001] have been developed to study the chemical and physical processes of air pollutants in the atmosphere. Meanwhile, to explain the various tropospheric chemistry problems, we have also developed a regional CTM. In this thesis, we apply the resulting CTM (hereafter referred to as REAM: the Regional chEmical trAnsport Model) to examine spring-to-summer transitions of  $\text{O}_3$  and its precursors, largely driven by rapid changes in the factors

and their associated photochemistry. We also examine the role of the factors on the optimization of NO<sub>x</sub> emissions and the budget of the tracers.

Even with regional-scale CTMs such as REAM, estimating the quantitative impact of the various factors on air pollutants is still difficult because of the lack of in-situ surface or aircraft measurements in extreme environments such as thunderstorms. Despite the drawback of cloud interference of space-borne measurements, satellite observations can potentially be a complementary method of overcoming this limitation [e.g., Li *et al.*, 2005; Jing *et al.*, 2006]. Therefore, the validation of REAM and an examination of the impact of these factors on O<sub>3</sub> and its precursors necessitate the following: corresponding surface observations of O<sub>3</sub>, NO<sub>x</sub>, and CO from the EPA AIRNow and the Southeastern Aerosol Research and Characterization Study (SEARCH); the vertical profiles of O<sub>3</sub> from the Measurement of Ozone and Water Vapor by Airbus In-Service Aircraft (MOZAIC) and ozonesondes; NO<sub>2</sub> tropospheric columns from the Global Ozone Monitoring Experiment (GOME) and the Ozone Monitoring Instrument (OMI); CO columns from the Measurement of Pollution in the Troposphere (MOPITT); O<sub>3</sub> and CO vertical profiles from the Tropospheric Emission Spectrometer (TES); and tropospheric O<sub>3</sub> columns from the Total Ozone Mapping Satellite (TOMS) and the Stratospheric Aerosol and Gas Experiment II (SAGE II), and OMI and the Microwave Limb Sounder (MLS).

From the Investigation of Sulfur Chemistry in the Antarctic Troposphere (ISCAT) experiments during 1998 and 2000, high concentrations of NO at the South Pole (SP) have been identified. NO concentrations reached over 500 pptv [Davis *et al.*, 2001, 2004], significantly higher than those in the Arctic [Honrath *et al.*, 1999; Ridley *et al.*,



2000]. The high NO concentrations occurred due to the emissions of NO<sub>x</sub>, resulting from nitrate photolysis inside snow pack [Davis *et al.*, 2001, and references therein]. As a result, measurements show higher 24-hour average concentrations of OH at SP than they show in the tropical marine boundary [Mauldin *et al.*, 2001, 2004]. In addition, active photochemistry driven by snow NO emissions leads to significant ozone production [e.g., Crawford *et al.*, 2001, Chen *et al.*, 2004]. Davis *et al.* [2004] further speculated that given the rate of nitrate photolysis, most of the plateau should exhibit high levels of O<sub>3</sub> as well as OH near the surface. Today, the spatial extent and overall impact of snow NO<sub>x</sub> emissions on photochemistry over Antarctica is not clear. Interestingly, flux estimated by Jones *et al.* [2001] at the German Antarctica station, Neumayer (70°S, 8°W), was only about one-third of that estimated by Onclay *et al.* [2004] at SP. Snow emissions clearly vary over Antarctica. In order to address the various issues related to reactive nitrogen and its coupling to atmospheric oxidizing species such as OH, we need to extend the measurements of NO<sub>x</sub> so that they include a larger area of Antarctica and extend the previous box model analysis to 1-D CTM and 3-D CTM, REAM analyses.

## 1.2 Space-borne Measurements and Models

### 1.2.1 Tropospheric NO<sub>2</sub> Column from GOME and OMI

The GOME instrument is on board the European Remote Sensing-2 (ERS-2) satellite that passes over the equator at 1030 AM local time and its horizontal resolution is 40 km latitude by 320 km longitude. In the Differential Optical Absorption Spectroscopy (DOAS) algorithm, an air mass factor (AMF), is used to translate a slant column to a vertical column, as described by previous studies [Palmer *et al.*, 2001;

Martin *et al.*, 2002]. AMF considers not only the geometrical configuration of the atmosphere but also its atmospheric states. In other words, AMF is mathematically expressed by an integral of the products of the relative vertical profiles, the shape factors of NO<sub>2</sub> from the two models, REAM and GEOS-CHEM, and the sensitivity of backscattered radiance to changes in tracer concentration [Martin *et al.*, 2002]. Sensitivity is estimated from the linearized discrete ordinate radiative transfer (LIDORT) model [Spurr *et al.*, 2001], one of the exact algorithms that accurately accounts for multiple scatterings in the atmosphere. The detailed retrieval method of tropospheric NO<sub>2</sub> columns from GOME measurements and the estimation of its uncertainty are described in a previous study by Martin *et al.* [2002]: First, fitting directly backscattered radiance spectra from GOME instruments produces a slant column; then a stratospheric column determined from an NO<sub>2</sub> column over the central Pacific is subtracted from the total column with an assumption that stratospheric columns are zonally constant; and finally, the subtracted slant column is converted into a vertical column using AMF. The calculation of AMF requires information about clouds and aerosols. The cloud fraction and cloud-top pressure are from GOME [Kurosu *et al.*, 1999]. Also, the monthly mean fields of aerosol mass concentrations between February and May of 2000 are from the Global Ozone Chemistry Aerosol Radiation and Transport (GOCART) model [Chin, 2002], which includes 3-D dimensional sulfate, mineral dust, sea salt, hydrophobic and hydrophilic black carbon, and organic carbon [Mian Chin, Personal Comm., 2004]. Data that show >40% cloud cover are disregarded, as suggested by Martin *et al.* [2002]. Retrieval uncertainties are mostly due to spectral fitting, spectral artifacts from a diffuser

plate, the removal of stratospheric columns, and the AMF calculation [Martin *et al.*, 2002].

OMI onboard the NASA Aura satellite, which passes over the equator at 1345 PM local time have horizontal resolutions of  $13 \text{ km} \times 24 \text{ km}$ . Algorithms for retrieving the OMI total and tropospheric NO<sub>2</sub> columns are described in previous studies by Boersma *et al.* [2001] and Bucsela *et al.* [2006]. Parameters such as viewing geometry, surface albedo, and the shape factor of NO<sub>2</sub> are needed to estimate AMF. Two AMF's are estimated using two shape factors from the Goddard Space Flight Center (GSFC) CTM and GEOS-CHEM, which are for unpolluted (the stratosphere and upper troposphere) and polluted (the lower and middle troposphere) NO<sub>2</sub> profiles, respectively. The radiance-weighted sum of clear and cloudy conditions is used to estimate each AMF. A detailed explanation about OMI NO<sub>2</sub> retrievals and total and tropospheric NO<sub>2</sub> data are available from <http://disc.gsfc.nasa.gov/Aura/OMI/omno2.shtml>.

### 1.2.2 Total CO Column from MOPITT

The MOPITT instrument on board the NASA Terra satellite provides the capability of globally monitoring CO through observations of two spectral bands: a solar band around  $2.3 \text{ }\mu\text{m}$  and a thermal band around  $4.6 \text{ }\mu\text{m}$ . The satellite passes over the equator at around 1045 AM and 2245 PM local time, and the horizontal resolution of MOPITT is  $22 \times 22 \text{ km}^2$ . MOPITT detectors measure filtered radiance from the top of the atmosphere (TOA) from a gas correlation radiometer that produces gas correlation spectroscopy composed of an average response signal (A) and a different response signal (D) rather than capturing TOA radiance directly [Pan *et al.*, 1995, 1998]. The retrieval

procedure of passive remote sensing measurements does not allow one to get delta function-type vertical profiles. Therefore, the solution of an inverse problem needs to be solved by an optimum estimate method with a priori information, filtered radiances, and data from the gas correlation radiometer [Rodgers, 2000]. If the probability distribution function (PDF) of a state vector (CO vertical profile) is proportional to that of an observed signal measured by a MOPITT instrument, an inverse problem with an ill-posed condition is resolved by minimizing the cost function.

MOPITT CO columns are obtained from a data pool of the NASA Langley Atmospheric Science Data Center (ASDC). The uncertainty of the CO columns, as reported by the data, averages  $2 \times 10^{17}$  molecules  $\text{cm}^{-2}$  for each datum. When compared to the MOPITT observations, simulated CO concentrations are processed with the MOPITT retrieval averaging kernel (AK), described in previous studies by Deeter *et al.* [2003] and Emmons *et al.* [2004]. First, corresponding simulated CO concentrations are estimated for the standard pressure levels of MOPITT: surface, 850, 700, 500, 350, 250 and 150 hPa; second, the AK matrix is estimated from the retrieval error covariance and the a priori covariance matrix; then the seven levels of CO concentrations processed with AK are calculated; and finally, the total number of CO columns is estimated with the retrieved CO concentrations at the pressure levels.

### 1.2.3 Tropospheric O<sub>3</sub> from TOMS-SAGE II and OMI-MLS

TOMS on board the Earth Probe satellite with an equator crossing time of 1116 AM local time measures incident solar radiation and backscattered ultraviolet sunlight, resulting in deriving total ozone; TOMS has a horizontal resolution of  $39 \times 39 \text{ km}^2$  and a

measurement uncertainty of about 5% (the random error is 2% and the systematic error about 3%) [[ftp://toms.gsfc.nasa.gov/pub/eptoms/EARTHPROBE\\_USERGUIDE.PDF](ftp://toms.gsfc.nasa.gov/pub/eptoms/EARTHPROBE_USERGUIDE.PDF)]. SAGE II on board the Earth Radiation Budget Satellite (ERBS) measures the Earth's limb extinction via the solar occultation technique during each spacecraft sunrise and sunset. The horizontal and vertical resolutions of SAGE are about  $30 \times 250 \text{ km}^2$  and 1 km, respectively. The scatter-plots of SAGE II (retrieval version 6.2)  $\text{O}_3$  versus potential vorticity (PV) on isentropic surfaces are used to produce the  $\text{O}_3$  profiles in the stratosphere [Jing *et al.*, 2004], which are coincident with the TOMS (version 8) total column  $\text{O}_3$  measurements in latitude, longitude, and time. When the TOMS data indicate a reflectivity less than 20%, tropospheric  $\text{O}_3$  columns are inferred by subtracting the SAGE II-based stratospheric columns from the TOMS columns. The PV values are obtained from the NCEP reanalysis data set, and the value of the 3.5 PV units is used to define the location of the tropopause. Based on comparisons with the ozonesondes, two previous studies by H. J. Wang *et al.* [2002, 2006] indicate that SAGE  $\text{O}_3$  has an accuracy of 10% or better down to the tropopause with SAGE values almost 5% higher than the ozonesondes at an altitude between 15 and 20 km. A previous study by Jing *et al.* [2004] suggested that mapping produces individual  $\text{O}_3$  values in the stratosphere with a precision of about 10%. However, this error tends to be random, and stratospheric columns averaged several days, for example, are expected to have significantly better precision.

OMI and MLS onboard the NASA Aura satellite that passes over the equator at 1345 PM local time have horizontal resolution of  $13 \text{ km} \times 24 \text{ km}$  and spatial resolution of  $30 \text{ km} \times 150 \text{ km} \times 2.5 \text{ km}$ , respectively. To derive a tropospheric  $\text{O}_3$  column by

implementing a residual method, we have used a combination of MLS profiles above 215 hPa and averaged OMI level 2 total O<sub>3</sub>, which satisfies a coincidence criterion with MLS profiles. OMI and MLS coincidence criteria are  $\pm 1.25^\circ$  longitude by  $1.25^\circ$  latitude and on the same day. The location of the tropopause is derived from the NCEP reanalysis data. Mid-latitude stratospheric O<sub>3</sub> columns for between 215 hPa and the tropopause are obtained by the SAGE II mapping profiles. Tropospheric O<sub>3</sub> columns are then obtained by subtracting the stratospheric O<sub>3</sub> columns from the OMI total columns. To prevent interference from clouds on the OMI total O<sub>3</sub> column, we use only total columns obtained under clear conditions, which is defined by a reflectivity of less than 10% based on OMI 360 nm reflectivity datasets. Yang *et al.* [2007] provide a detailed explanation.

#### 1.2.4 3-D Global Chemical Transport Model, GEOS-CHEM

In order to prepare the initial and boundary chemical conditions for and cross-validate REAM, we use the GEOS-CHEM model [Bey *et al.*, 2001] driven by the assimilated meteorological observations for 2000, updated three to six hours from the GEOS of the NASA Data Assimilation Office (DAO) [Schubert *et al.*, 1993] for the 2000 simulations, and the assimilated meteorological data from GEOS-4 at the NASA Global Modeling and Assimilation Office (GMAO) for the 2005 simulations. The horizontal resolution of the used model (GEOS-CHEM 7.2) is  $2^\circ$  latitude by  $2.5^\circ$  longitude. The model has thirty vertical layers on a sigma level, reaching from the surface to 0.01 hPa. Thirty chemical tracers describing tropospheric O<sub>3</sub> chemistry are transported. A detailed photochemistry module, algorithms for dry and wet deposition, and emissions from vegetation and soils are described in a study by Bey *et al.* [2001].

### 1.2.5 3-D Regional Chemical Transport Model, REAM

#### 1.2.5.1 Model framework

GEOS-CHEM is used to specify the initial and boundary conditions of chemical species in REAM. Lateral and top boundary conditions are updated hourly or daily. The REAM domain covers North America and the portion of the North Atlantic with a 70 km horizontal resolution. The numbers of horizontal grid points are 80 and 60, respectively, for west to east and south to north on a Lambert conformal map projection. REAM has 23 vertical layers from the surface to 10 hPa, and terrain-following  $\sigma$  coordinates are used. MM5 is run with four-dimensional data assimilation (FDDA) with the National Center Environmental Prediction (NCEP) reanalysis, rawinsonde, and surface observations [Zeng *et al.*, 2003]. Meteorological fields are also provided for 23 vertical sigma-coordinate levels from MM5. For the advection and diffusion processes, meteorological and physical variables are stored every half hour and interpolated every five minutes. The variables are archived every 2.5 minutes for cloud convection and lightning  $\text{NO}_x$  production. The integration of the chemical reaction, wet and dry deposition, and emissions are performed every hour.

For the transport of air pollutants, MM5 produces input variables (in unit): temperature (K), wind scalar velocities ( $\text{m s}^{-1}$ ), cloud water mixing ratio ( $\text{kg kg}^{-1}$ ), the rain water mixing ratio ( $\text{kg kg}^{-1}$ ), diffusion coefficients ( $\text{m}^2 \text{s}^{-1}$ ), pressure (Pa), convective precipitation (cm), non-convective precipitation (cm), surface albedo (fraction), land use (category), the periodic boundary layer (PBL), the top layer (dimensionless), PBL height (m), PBL regime (dimensionless), sensible heat flux ( $\text{Wm}^{-2}$ ), frictional velocity ( $\text{ms}^{-1}$ ), surface radiation ( $\text{Wm}^{-2}$ ), soil temperature (K), 10-meter horizontal velocities ( $\text{ms}^{-1}$ ), and

surface roughness (cm). As described, these variables are similarly used in other studies [McKeen *et al.*, 1991; Hess *et al.*, 2000]. A photochemical module, the algorithms for dry and wet deposition, and emissions from vegetation and soils are adopted from GEOS-CHEM [Bey *et al.*, 2001, and references hereafter]. REAM includes a detailed photochemical mechanism that includes about 200 reactions, the chemical concentration changes of 120 species are estimated, and 24 tracers (family or species) are transported to describe O<sub>3</sub>-NO<sub>x</sub>-hydrocarbon [Bey *et al.*, 2001]. Detailed explanations follow.

#### *1.2.5.2 Model components*

Like conservation of energy and momentum, a chemical tracer needs to be conserved during the transport and vertical mixing processes. A transport module consists of horizontal advection, deep and shallow vertical convections, and diffusion. Transport caused by diffusion includes molecular diffusion caused by molecular collisions and eddy diffusion driven by mechanical shear and thermal buoyancy. The strength of the former is substantially weaker than that of the latter, so the former is not considered in REAM. The deposition process includes dry and wet depositions. The dry deposition of oxidants and soluble gases is estimated using a resistance-in-series model [Wesely *et al.*, 1989] with some modifications [Wang *et al.*, 1998]. Large-scale wet deposition consists of washout and rainout. The former is caused by wet scavenging inside a cloud, and the latter rain scavenging below a cloud [Liu *et al.*, 2001]. The convective scavenging of soluble species is separately considered in REAM, as described by Liu *et al.*, [2001].

#### *1.2.5.3 Advection and convection*



We adopt an efficient and accurate tracer transport model scheme [Walcek, 2000, Zeng *et al.*, 2003] to treat advection. Among the four different cumulus convection schemes [Jacobson, 1999], which include the moist convective adjust, Kuo, Arakawa-Schubert, and Grell schemes, we use the Grell scheme [1993] for cumulus convection parameterization in order to be consistent with the dynamic model, MM5. Transport through a cloud, which is on a sub-grid scale, is parameterized based on earlier studies [Lin *et al.*, 1994; Jacobson, 1999]. In order to incorporate deep cumulus convections in the model, we use the top levels of cloud, originating levels, and air mass fluxes for updraft and downdraft processes from MM5. The sub-grid scale updrafts of air masses are considered during updrafts from originating levels to cloud-top levels. The convective wet scavenging of soluble tracers is also considered during an updraft process. Large-scale downward subsidence follows. In nature, the mass of species is conserved. Likewise, during a downdraft process, as in an updraft process, a downdraft flux to the bottom layer is considered, and large-scale transport follows a downdraft process. The Grell scheme assumes that an entrainment occurs at the cloud bottom, a detrainment occurs at the cloud top, and neither entrainment nor detrainment occurs between the cloud top and bottom [Grell, 1993].

For shallow convection, the top and bottom layers of a shallow convection are determined by MM5, and a cloud fraction is estimated using relative humidity, as described by Geleyn [1981] and Lin *et al.* [1994]. A shallow convection that mixes chemical tracers between the two adjacent layers at a time exhibits neither precipitation nor a downdraft process.

#### *1.2.5.4 Diffusion*

For stable and weakly unstable conditions, turbulent (i.e., eddy) diffusion transports are considered using the K-theory (i.e., the gradient transport theory) [Holton, 1992; Jacob, 1999; Jacobson, 1999], which allows mixing between two adjacent layers. Under strong, unstable conditions, a full mixing method such as a free convective-plume scheme [Blackadar, 1978; Zhang and Anthes, 1982] is used to simultaneously mix a tracer for all layers within a boundary layer. Eddy diffusivities for the K-theory are from MM5, which depend on wind speed, surface roughness, surface heating, and altitude.

#### *1.2.5.5 Chemical and photolysis reactions*

We incorporate a chemistry module using a fast and numerically accurate Gear-type solver [Jacobson and Turco, 1994] in which an original Gear's code is combined with a sparse-matrix and computer optimization technique [Jacobson, 1999]. Inside the chemistry module, one hundred twenty species are included in a chemistry mechanism. Moreover, the surface areas of sulfate aerosols are calculated using the concentrations of aerosols from Chin *et al.*, [1996], as described by Y. Wang *et al.*, [1998]. Photolysis rates are calculated with the fast and flexible FAST-J algorithm of Wild *et al.* [2000], which accounts for cloud, aerosol, and Mie scattering. Cloud optical depths are calculated using MM5 cloud water content [Stephens *et al.*, 1978; Weele *et al.*, 1993; Salby, 1996]. The source of UV surface albedo is the TOMS satellite [Herman and Celarier, 1997].

#### *1.2.5.6 Dry and wet depositions*

Dry deposition velocities are calculated using a resistance-series scheme [Wesley, 1989; Seinfeld and Pandis, 1998]. These resistances are calculated, with some modifications, using Monin-Obukhov length, momentum, temperature, friction velocity, solar irradiation, and resistance variables on the basis of the formulas of Wesely [1989] [Y. Wang *et al.*, 1998; Bey *et al.*, 2001]. Variables are calculated or directly archived from MM5. Ozone, NO<sub>2</sub>, nitric acid (HNO<sub>3</sub>), hydrocarbon peroxide (H<sub>2</sub>O<sub>2</sub>), formaldehyde (HCHO), peroxyacetic acid (PAN), and NO are considered in the dry deposition process. For the wet scavenging process, two scavenging processes are considered: One accounts for scavenges that occur during the updraft convection of deep cumulus convection [Hess *et al.*, 2000; Liu *et al.*, 2001], and the other is from large-scale precipitation due to rainout and washout by stratiform and convective anvil precipitation, respectively [Giorgi and Chameides, 1986; Liu *et al.*, 2001]. Wet scavenging accounts for the scavenging of tracers with high solubility, which include HNO<sub>3</sub>, H<sub>2</sub>O<sub>2</sub>, HCHO, and methyl hydroperoxide (CH<sub>3</sub>OOH).

#### *1.2.5.7 Emissions*

For NO<sub>x</sub> emissions, the EPA 1999 National Emission Inventory (referred to as NEI99) Version 2, the National Acid Precipitation Assessment Program (NAPAP), and the Global Emission Inventory Activity (GEIA) [Benkovitz *et al.*, 1996; Yienger and Levy, 1995] are used in the United States, Canada, and Mexico, respectively. For CO emissions, NEI99 is used in the United States, and CO emissions developed at Harvard [Bey *et al.*, 2001] are used in the other regions. Industrial non-methane hydrocarbon (NMHC) emissions are based on a study by Y. Wang *et al.* [1998]. For biogenic

emissions, the emission rates of isoprene and monoterpene are estimated by a modified version by Y. Wang *et al.* [1998] using an algorithm by Guenther *et al.* [1995]. The biogenic emissions of acetone are by Jacob *et al.* [2002]. Propene and CO productions due to the oxidation of isoprene and monoterpene are scaled to isoprene and monoterpene emissions as described by Bey *et al.* [2001]. The monthly averaged leaf area index (LAI) is from 1 km Advanced Very High Resolution Radiometer (AVHRR) data between April 1992 and March 1993 [Bonan *et al.*, 2002]. A detailed explanation of lightning NO<sub>x</sub> production parameterization follows.

#### 1.2.5.8 Lightning NO<sub>x</sub> parameterization

NO<sub>x</sub> production due to lightning flash is estimated, and the produced NO molecules are distributed vertically to the top cloud layer in the model. There are two flash types, cloud-to-ground (CG) and intracloud (IC) flashes. Lightning consists of a number of strokes, but NO<sub>x</sub> is primarily produced during the high-energy return stroke phase of the flash [Price *et al.*, 1997]. The NO molecules per IC flash are estimated to be one-tenth that of a CG flash ( $6.7 \times 10^{26}$  NO molecules flash<sup>-1</sup>) in some previous studies [Prince *et al.*, 1997; Pickering *et al.*, 1998; Allen *et al.*, 2000; Allen and Pickering, 2002]. Compared with the NO production rates of CG flash, equivalent rates are used for IC flash in several more recent studies [DeCaria *et al.*, 2000; Ott *et al.*, 2003; Zhang *et al.*, 2003; Fehr *et al.*, 2004; Choi *et al.*, 2005, 2007a, 2007b]. Based on cloud-resolving modeling output compared with anvil aircraft NO<sub>x</sub> observations over the U.S., the average NO production per flash for both IC and CG flashes is about  $2\text{-}4 \times 10^{26}$  NO molecules [K. Pickering, Personal Comm., 2005]. Ott *et al.* [2003] use  $3.0 \times 10^{26}$

molecules per flash for IC and CG flashes. We assume that NO production per IC flash is the same as that per CG flash. The NO production rate per flash used by Choi *et al.* [2005, 2007a] is  $6.0 \times 10^{26}$  NO molecules during the spring of 2000 and  $3.0 \times 10^{26}$  molecules [Choi *et al.*, 2007b] during the summer of 2005. Sensitivity results suggest that these values show better agreement with GOME and OMI measurements. Lightning NO<sub>x</sub> is distributed vertically following a mid-latitude profile by Pickering *et al.* [1998].

Two separate parameterizations are constructed for continental and oceanic regions [Price and Rind, 1993] using measurements from the National Lightning Detection Network (NLDN). The detection efficiency reported by Cummins *et al.* [1981] is used. We parameterize the lightning NO<sub>x</sub> production rate as a function of meteorological variables so that the emissions are consistent with the dynamic model, MM5. We experiment with cloud top height [Price and Rind, 1993], convective mass flux [Allen and Pickering, 2002], and convective available potential energy (CAPE) [Choi *et al.*, 2005, 2007a, 2007b]. We use both CAPE and cloud mass fluxes to take advantage of the different distributions of the two variables. However, the two meteorological variables must be normalized. The CG flashing rate for continental and oceanic regions are mathematically expressed in terms of normalized convective mass flux (M) and CAPE (C):

$$LF_{cg} = a_0 + aM + bM^2 + cM^3 + dC + eC^2 + fC^3 + gMC + hM^2C + iMC^2 + jM^4 + kM^3C + lM^2C^2 + mMC^3 + nC^4,$$

where for a continental region,  $a_0 = 0.00495$ ,  $a = 4.219$ ,  $b = 15.5064$ ,  $c = -112.492$ ,  $d = -2.089$ ,  $e = 48.143$ ,  $f = -53.983$ ,  $g = -121.956$ ,  $h = 358.118$ ,  $i = 208.105$ ,  $j = 108.613$ ,  $k = -$

216.226,  $l = -330.354$ ,  $m = -134.307$ ,  $n = 16.742$  and for an ocean region,  $a_0 = 0.126$ ,  $a = 2.669$ ,  $b = -0.854$ ,  $c = -61.793$ ,  $d = -2.482$ ,  $e = 24.35$ ,  $f = 26.739$ ,  $g = -31.732$ ,  $h = 288.129$ ,  $i = -185.419$ ,  $j = 63.089$ ,  $k = -178.063$ ,  $l = -151.659$ ,  $m = 204.120$ ,  $n = -34.408$ .

Once the CG flashing rate is estimated, the IC to CG flash rate ratio is calculated following Y. Wang *et al.* [1998].

### 1.3 Scope of This Dissertation

This dissertation focuses on the modeling analysis of the transitions of  $O_3$  and its precursors over North America from the spring to the summer and the photochemistry over Antarctica from in-situ and satellite observations. Chapter 2 provides evidence from satellite observations over North America of lightning  $NO_x$  production and the convective transport of pollutants. Column observations of  $NO_2$  and CO by GOME and MOPITT, measured separately over North America for April 2000, are investigated using REAM and the transient enhancements in these measurements due to lightning  $NO_x$  production and the convective process are examined. Chapter 3 presents the modeling analysis of the transition of air pollutants over North America from late winter to spring on the basis of in situ and satellite measurements. Trace gas simulations using REAM over North America between February and May of 2000 are analyzed to elucidate the impact of the springtime transition derived by the following factors: cloud convection, lightning  $NO_x$  production, soil  $NO_x$  emissions, and mixing depth on the concentrations and exports of key tracers. In situ observations from the EPA AIRNow and SEARCH ground network, aircraft observations from the TOPSE and MOZAIC experiments,

ozonesondes, and space-borne observations from GOME, MOPITT, TOMS and SAGE II satellite measurements are analyzed.

Chapter 4 presents a modeling analysis of the spring to summer transitions of  $O_3$  and its precursors over North America between April and August of 2005 on the basis of satellite observations and examines the seasonal trend of tropospheric  $O_3$  from OMI-MLS satellite observations.  $O_3$  column peaks are generally constrained by the stratospheric input, convective outflows of the  $O_3$  precursors and lightning  $NO_x$  production during the spring and the summer. Chapter 5 shows the late-spring increases of the transport of trans-Pacific pollution in UT using  $O_3$  and other key tracers. In this chapter, large enhancements of air pollutants such as  $NO_x$ , PAN, CO, CFCs, and Halon-1211 in UT are shown over North America in the late spring. An analysis of these observations and model results indicates that enhancements are driven by trans-Pacific pollutant transport. Chapter 6 presents a modeling analysis that assesses the photochemical impact of snow  $NO_x$  emissions over Antarctica during ANTCI 2003. 1-D CTM and 3-D CTM, REAM are used to analyze these measurements and assess the photochemical impact of snow emissions. The polar version of MM5 with a modification of the ETA turbulence scheme is used to simulate the heights of the boundary layer from Sound Detecting and Ranging (SODAR) measurements at SP. Daytime snow  $NO_x$  emissions are parameterized as a function of temperature and wind speed. The emission fluxes, deposition fluxes, and transported fluxes of nitrogen tracers over Antarctica are also estimated. Chapter 7 concludes.

## CHAPTER II

### EVIDENCE OF LIGHTNING NO<sub>x</sub> AND CONVECTIVE TRANSPORT OF POLLUTANTS IN SATELLITE OBSERVATIONS OVER NORTH AMERICA

#### 2.1 Introduction

Convective outflow is an important pathway for ventilating pollutants from the boundary layer to the free troposphere; subsequent transport of these pollutants has significant ramifications for hemispheric and global air quality. The effects of such processes over North America have been previously investigated using 3-D chemical transport simulations and surface and aircraft observations<sup>1</sup>ns [e.g., Thompson *et al.*, 1994; Horowitz *et al.*, 1998; Liang *et al.*, 1998; Park *et al.*, 2004b; Li *et al.*, 2005]. However, in situ observations of convective outflow are limited because of the sporadic nature of convection and aircraft operational difficulties. Recent advancements in satellite observations could potentially provide additional constraints on model simulated convective outflow.

Satellite observations of trace gases and aerosols have been used to detect forest fire plumes [Thomas *et al.*, 1998; Spichtinger *et al.*, 2001; Lamarque *et al.*, 2003]. In comparison, convective outflow is more difficult to detect due in part to cloud interference. Li *et al.* [2005] showed that despite this interference, satellite observations of CO and aerosol optical depth are useful for mapping convective outflow from North America to the western North Atlantic. In addition, indications were found for lightning

---

<sup>1</sup> This chapter is for “Evidence of lightning NO<sub>x</sub> and convective transport of pollutants in satellite observations over North America,” published at *Geophysical Research Letter* in January 2005 (32, L02805, doi:10.1029/2004GL021436). Authors are Y. Choi, Y. Wang, T. Zeng, R. Martin, T. Kurosu, and K. Chance.



activity in the monthly/seasonally averaged  $\text{NO}_2$  columns over the tropical Atlantic observed by the Global Ozone Monitoring Experiment (GOME) [Richter and Burrows, 2002; Edwards *et al.*, 2003].

In this work, we make use of GOME  $\text{NO}_2$  observations and Measurements Of Pollution In The Troposphere (MOPITT) observations of CO to evaluate the simulations of REAM. Both  $\text{NO}_2$  and CO are good chemical tracers for convection. Lightning during convection provides a major source of  $\text{NO}_x$  ( $\text{NO} + \text{NO}_2$ ) in the free troposphere [e.g., Price and Rind, 1993].

We analyze model simulations and satellite observations for April 2000 because of frequent cyclonegenesis and convective events over North America during that period. The analysis is carried out on a daily basis to emphasize the transient nature of convection. We conduct two model simulations with and without lightning  $\text{NO}_x$  production and compare these results with GOME observations. Carbon monoxide has much higher concentrations near the surface due to combustion and industrial emissions over North America. To test the effects of convection on CO concentrations, we conduct a sensitivity simulation in which convective transport of CO is turned off and then the standard and sensitivity simulations in light of MOPITT observations are compared.

## **2.2 GOME and MOPITT Retrievals**

The retrieval of tropospheric  $\text{NO}_2$  columns from GOME measurements and its uncertainty are calculated using the algorithms by Martin *et al.* [2002]. The retrieval uncertainties are due to spectral fitting, spectral artifact from the diffuser plate, the removal of the stratospheric column, and the calculation of the air mass factor. The

MOPITT CO columns are obtained from the data pool at the NASA Langley Atmospheric Science Data Center (ASDC). Only MOPITT retrievals with an a priori fraction of <50% were used. The uncertainty of CO columns as reported by the data is about  $2 \times 10^{17}$  molecules  $\text{cm}^{-2}$  in this work. When compared with the observations, the simulated CO results were processed using the MOPITT retrieval averaging kernel described by Deeter *et al.* [2003] and Emmons *et al.* [2004]. The horizontal resolutions of GOME and MOPITT are  $40 \times 320$  and  $22 \times 22 \text{ km}^2$ , respectively.

### 2.3 Model Description

REAM has a horizontal resolution of 70 km with 20 vertical layers below 100 hPa. The National Center for Atmospheric Research/Penn State MM5 was used to simulate the meteorological fields using four-dimensional data assimilation with the National Center for Environmental Prediction reanalysis, surface, and rawinsonde observations. Most meteorological variables were archived every 2.5 minutes. The horizontal domain of MM5 has five extra grids beyond that of REAM on each side to minimize potential transport anomalies near the boundary. As in the work by Zeng *et al.* [2003], spring 2000 simulations using the global GEOS-CHEM model [Bey *et al.*, 2001] provide the initial and boundary conditions for trace gases. The regional simulations were spun up during the last week of March.

REAM was updated from the previous model by McKeen *et al.* [1991]. The transport scheme by Walcek [2000] was adopted. Twenty-four chemical tracers describing tropospheric  $\text{O}_3$  chemistry [Bey *et al.*, 2001] were transported. The convective scheme by Grell [1993] was implemented so that it was consistent with the

meteorological model. The photochemistry module, and the algorithms for dry and wet deposition and emissions from vegetation and soils are adopted from GEOS-CHEM [Bey *et al.* 2001, and references therein]. Biogenic emissions of hydrocarbons are limited to the regions south of 30°N in April. The monthly mean leaf area index distribution was derived from the Advanced Very High Resolution Radiometer data by Bonan *et al.* [2002]. Emission inventories for combustion and industrial sources were also taken from GEOS-CHEM [Bey *et al.*, 2001], except that fossil fuel NO<sub>x</sub> and CO emissions over the United States were taken from the 1999 US Environmental Protection Agency National Emission Inventory. The lightning NO<sub>x</sub> algorithm is described in Appendix 2.A. Cloud-to-ground flashes in the model are constrained by observations from the National Lightning Detection Network (NLDN).

## **2.4 Results and Discussion**

### **2.4.1 Is Lightning NO<sub>x</sub> Evident in GOME Observations?**

Monthly mean-simulated tropospheric NO<sub>2</sub> column compares well with the GOME observations (not shown). We find a correlation coefficient of 0.95 with little mean bias (-3%). Our main goal in this work is to determine if transient convection features such as lightning NO<sub>x</sub> production can be detected in the GOME observations. Large convective or cyclonegenesis events were simulated on April 7-10, 14-16, 18-22, 25-27, and 29-30. Generally, we find corresponding NO<sub>2</sub> column enhancements associated with these events. We illustrate four specific days of April 20, 21, 27, and 29 (Figure 2.1).

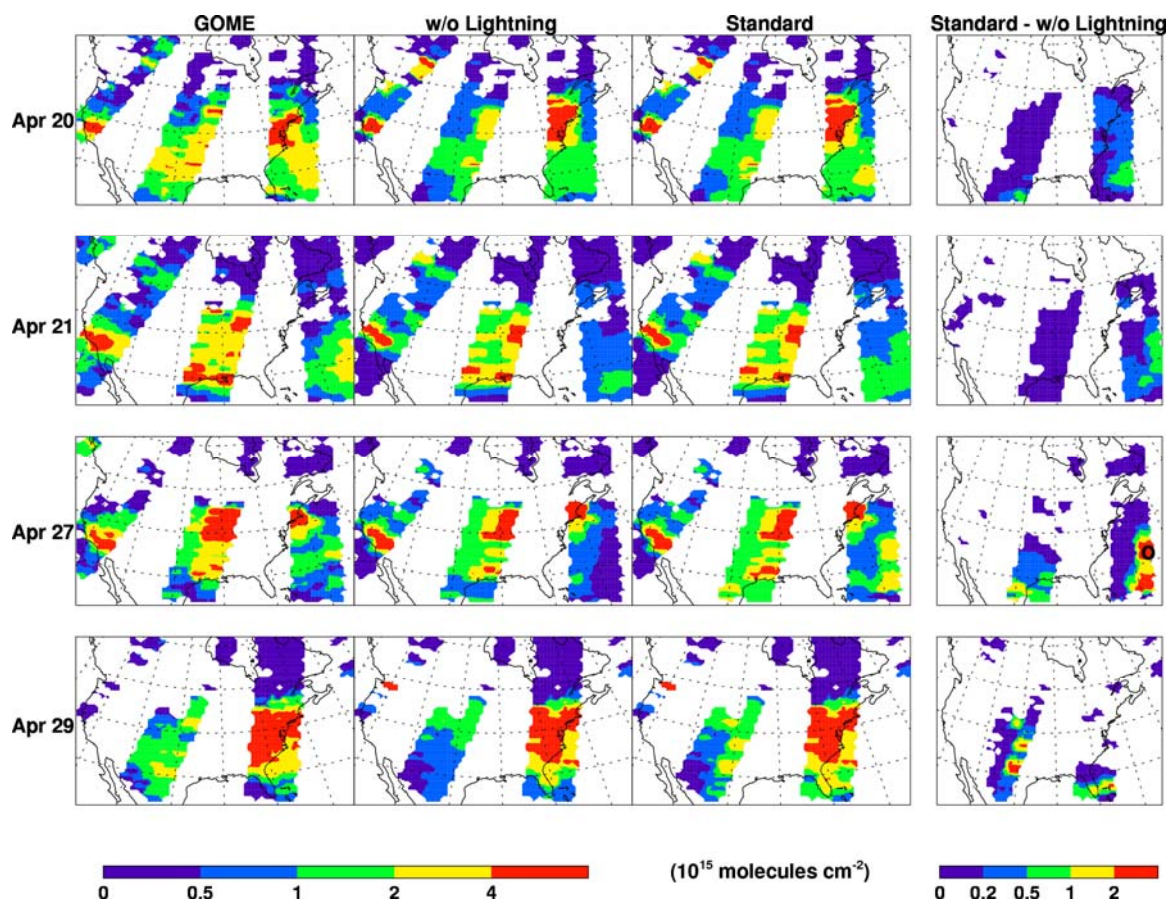


**Figure 2.1** GOME retrieved and the corresponding REAM simulated tropospheric NO<sub>2</sub> vertical column on April 20, 21, 27, and 29, 2000. GOME columns less than the spectral fitting uncertainties are not included. Simulations with and without lightning NO<sub>x</sub> production are shown. The last column shows the simulated lightning NO<sub>2</sub> enhancements.

The model simulations with lightning  $\text{NO}_x$  are clearly in much better agreement with the observations. All four cases show various degrees of lightning enhancements over the western North Atlantic. The April 29 case also shows significant continental enhancements from western Texas to Kansas. However, the lightning signals are more difficult to detect over the continent because of surface emissions. The standard model underestimates  $\text{NO}_x$  concentrations over the western North Atlantic on April 20 and 21 but tends to overestimate them on April 27.

The lightning enhancements are  $0.5\text{--}1 \times 10^{15}$  molecules  $\text{cm}^{-2}$  on April 20 and 21 and  $>1 \times 10^{15}$  molecules  $\text{cm}^{-2}$  on April 27 and 29. Following Martin *et al.* [2002], we estimate the uncertainties of GOME  $\text{NO}_2$  vertical columns to be 50-100% of the lightning enhancements simulated in the model. The relative uncertainties are at the high end for April 20 and 21, when the model underestimates lightning  $\text{NO}_x$  enhancements over the western North Atlantic. Satellite observations with improved spatial coverage and lower uncertainty than GOME should provide better quantitative constraints on lightning production of  $\text{NO}_x$ .

We select a grid box with large lightning  $\text{NO}_x$  enhancements on April 27 to illustrate the altitude dependence of the lightning  $\text{NO}_x$  contribution to the  $\text{NO}_2$  column (Figure 2.2).  $\text{NO}_2$  lightning enhancements are in the lower and upper troposphere, corresponding to the “C”-shaped  $\text{NO}_x$  profile by Pickering *et al.* [1998]. Enhancement of the upper tropospheric NO is far more prominent than that of  $\text{NO}_2$  because the  $\text{NO}/\text{NO}_2$  ratio increases with decreasing temperature. The large enhancements in the lower troposphere are due to convective downdrafts. The contribution to column enhancement

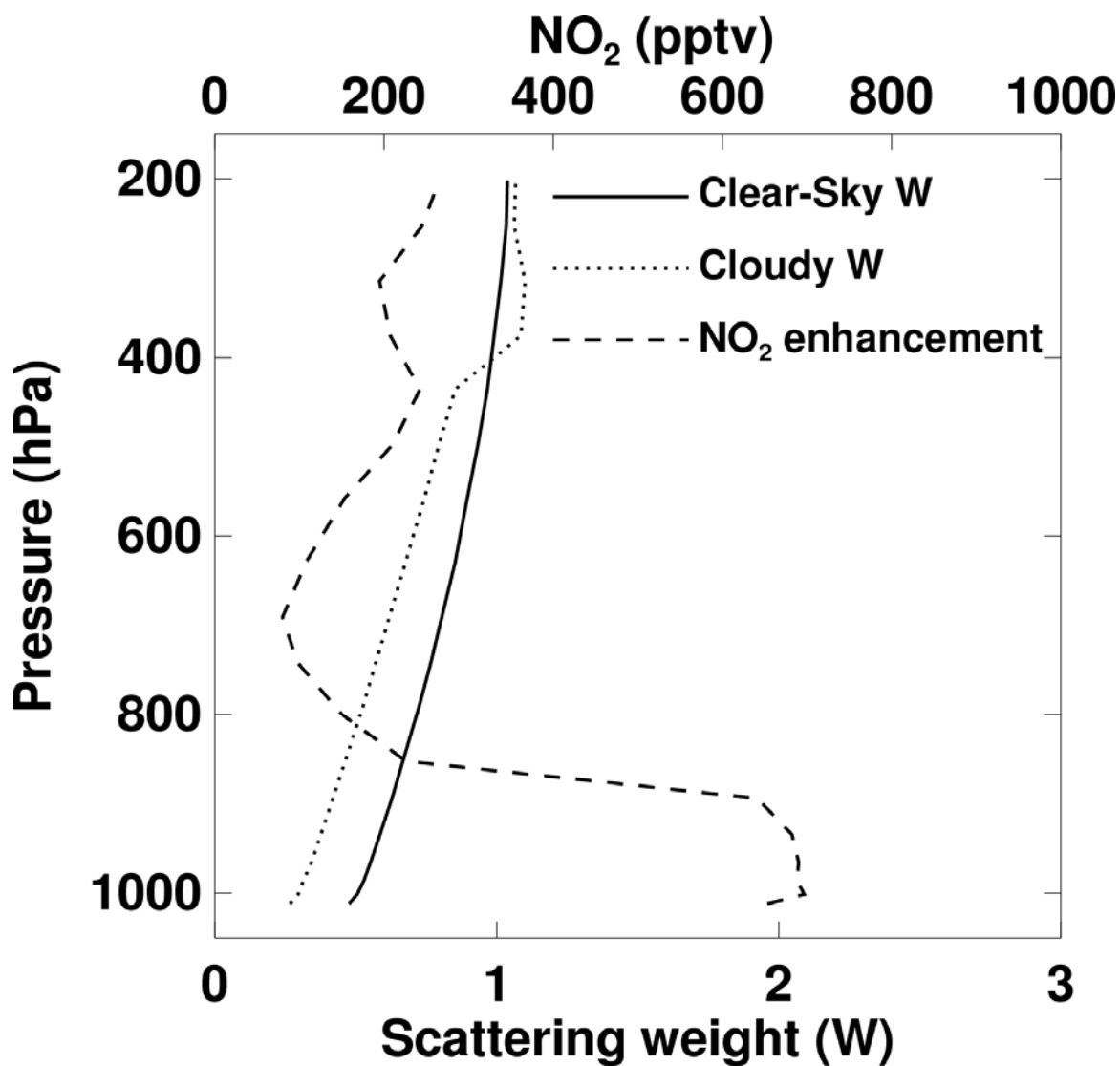


**Figure 2.2** Scattering weights under clear and cloudy sky conditions for the standard model NO<sub>2</sub> simulation on April 27 over the grid box indicated by the black circle in Figure 2.1. Also shown as a function of pressure is the simulated enhancement of NO<sub>2</sub> due to lightning NO<sub>x</sub> production. The scattering weight represents the sensitivity of backscattering radiance measured by GOME to NO<sub>2</sub> concentrations at a given level.

by NO<sub>2</sub> above 600 hPa is larger than in the lower troposphere (below 850 hPa) in part because of the larger scattering weight at higher altitudes (Figure 2.2).

#### 2.4.2 Signals of Convective Transport in MOPITT CO Observations

The simulated monthly mean CO column also compares well with MOPITT observations (not shown). We find a linear correlation coefficient of 0.88 with little mean bias (-2%). As in the previous section, we select three cases on April 20, 21, and 27 to illustrate the effects of convection on CO column concentrations (Figure 2.3). The effects are found over the ocean because the only difference between standard and sensitivity simulations is the convective transport of CO. Its effect is to lift CO, emitted from the surface, into a higher altitude, where wind speeds are higher than they are near the surface. As a result, higher-altitude CO lifted by convection is carried over the ocean faster in a more westerly flow compared to that near the surface, creating the enhancements seen in Figure 2.3. The April 29 case is not shown because the convection is mostly limited to land (Figure 2.1).

The simulations without the convective transport of CO clearly underestimate CO columns over the western North Atlantic. The standard simulations agree much better with the observations. The model tendencies that underestimate CO enhancements on April 20 and 21 but overestimate CO enhancements on April 27 are consistent with the results for lightning NO<sub>x</sub> enhancements. The simulated CO column enhancements are above the MOPITT retrieval uncertainty of  $2 \times 10^{17}$  molecules cm<sup>-2</sup>.

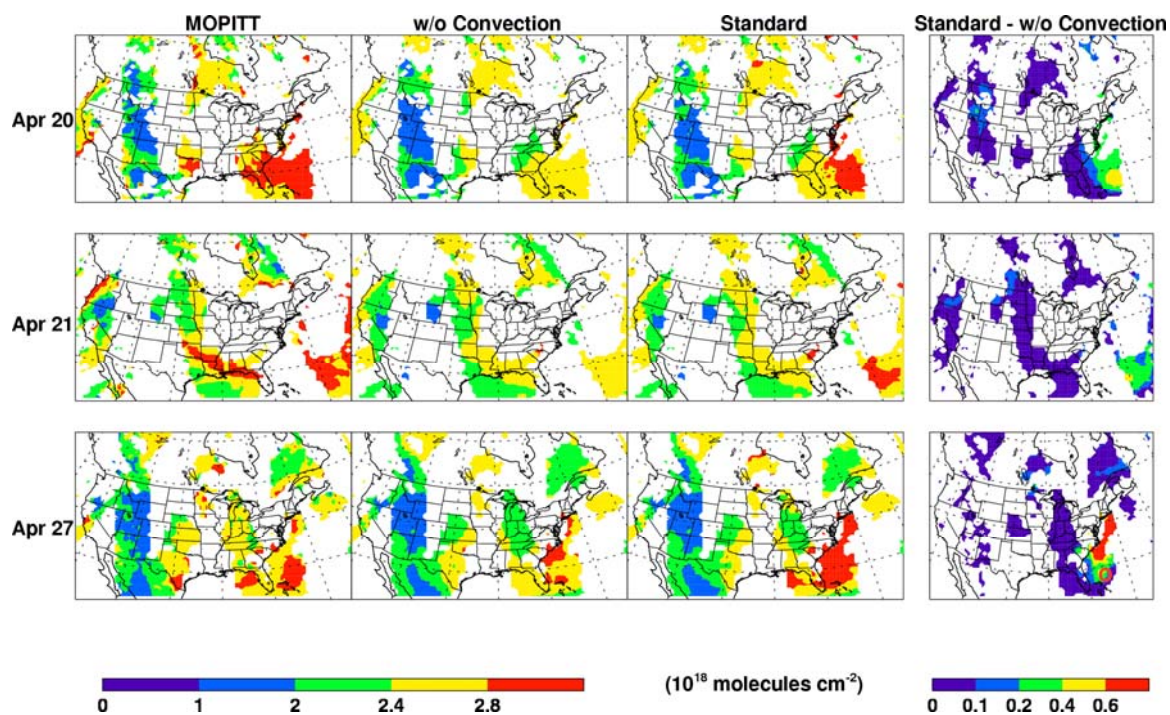


**Figure 2.3** The same as Figure 2.1, but for MOPITT-retrieved and REAM-simulated CO columns on April 20, 21, and 27, 2000. The model results with and without convective transport have been processed with the MOPITT averaging kernel.



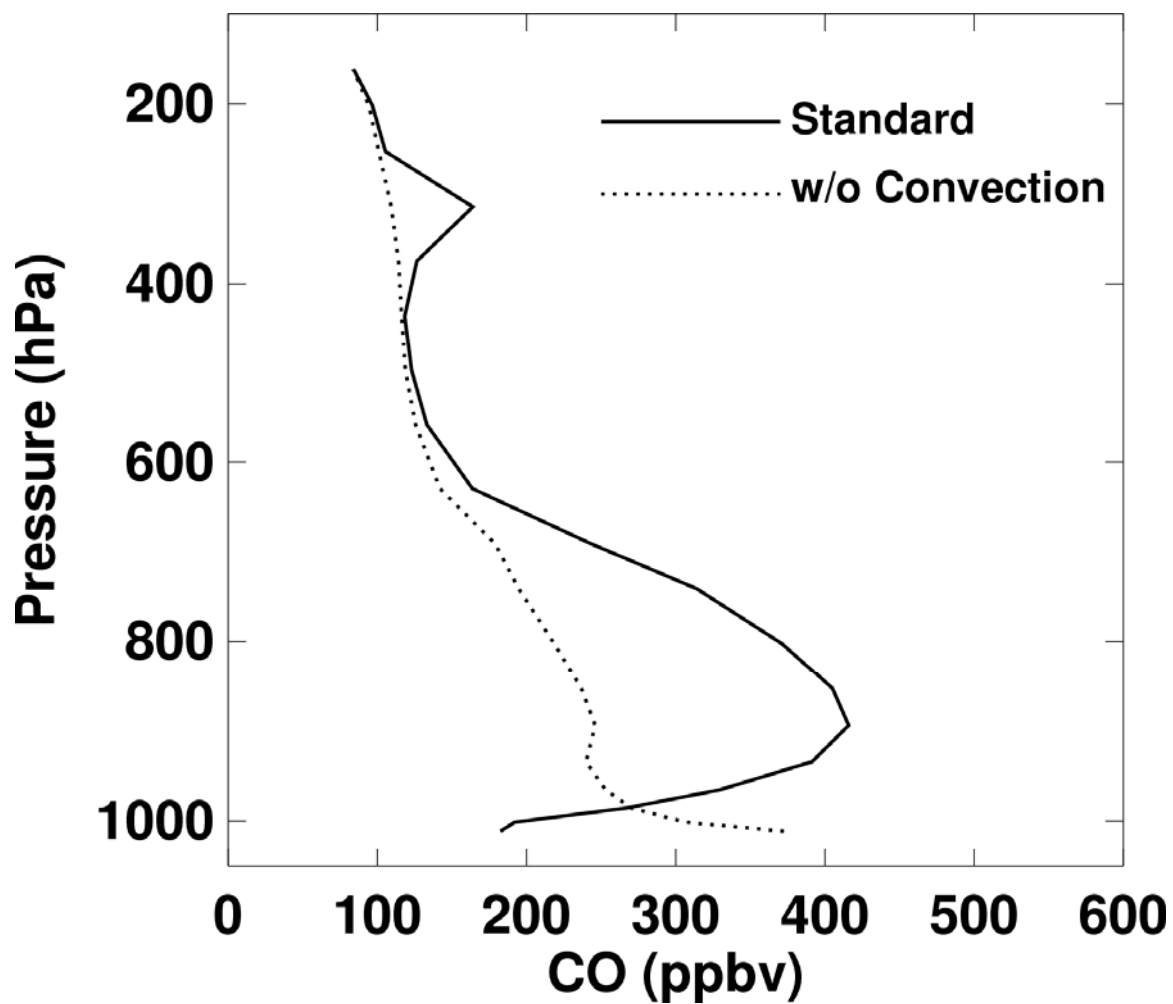


**Figure 2.4** Simulated CO concentrations with and without convective transport as a function of pressure on April 27 over the grid box indicated by the orange circle in Figure 2.3.

The altitude dependence of the CO enhancement contribution for a selected grid box on April 27 is shown in Figure 2.4. The profile with the convective transport of CO compared to that without is much higher at 300 hPa and 700-980 hPa, but it is lower near the surface due to the redistribution of CO by convective transport. The 700-980 hPa enhancement due to shallow convection is much larger than that at 300 hPa due to deep convection. This result is consistent with our finding that mass fluxes of shallow convection are much larger than deep convection in MM5 simulations during this period.

## 2.5 Conclusions

Chemical tracer distributions are strongly affected by convective transport and, in the case of  $\text{NO}_x$ , lightning production. We show that column observations of  $\text{NO}_2$  by GOME and CO by MOPITT can be used to identify these transient features when used in combination with 3-D chemical transport model simulations. The two independent measurements show consistent convection related enhancements in terms of geographic location and model bias. While the middle and upper tropospheric contribution from lightning  $\text{NO}_2$  to the column enhancements is more significant, the major contribution to CO column enhancements is from the lower troposphere. The model results indicate large enhancements in the lower atmosphere of lightning  $\text{NO}_2$  (due to convective downdrafts) and transported CO (due to shallow convection), suggesting that low-altitude aircraft in situ observations can potentially provide valuable and critical observations for evaluating model simulations and validating satellite observations.

### *Appendix 2.A: Lightning $\text{NO}_x$ parameterization*

We parameterize the lightning NO<sub>x</sub> production rate as a function of meteorological variables so that this emission is consistent with model dynamics. In our work, we experimented with cloud top height [Price and Rind, 1993], convective mass flux [Allen and Pickering, 2002], and convective available potential energy (CAPE). We found that the parameterization with CAPE produces a similar but better lightning flash distribution than cloud top height when compared with NLDN observations and that CAPE is a better variable for parameterizing lightning flashes than convective mass flux over the southern part of North America and the western Atlantic. To take advantage of the distribution difference between CAPE and convective mass flux, both variables are used in the parameterization (up to the 4<sup>th</sup> order, including cross terms). Two parameterizations are created separately for the land and the ocean. The intracloud (IC) to cloud-ground (CG) flash ratio is calculated following Y. Wang *et al.* [1998]. We assume that IC and CG flashes have the same energy [Ott *et al.*, 2003]. The rate of NO produced per unit energy is that of Pickering *et al.* [1998]. Lightning NO<sub>x</sub> is distributed vertically following the mid-latitude profile by Pickering *et al.* [1998].

## CHAPTER III

### MODELING ANALYSIS OF SPRINGTIME TRANSITION OF NO<sub>2</sub>, CO, AND O<sub>3</sub> OVER NORTH AMERICA ON THE BASIS OF IN SITU AND SATELLITE MEASUREMENTS

#### 3.1 Introduction

Ozone (O<sub>3</sub>), carbon monoxide (CO) and nitric oxides (NO<sub>x</sub> = NO+NO<sub>2</sub>), which are regulated under EPA's National Ambient Air Quality Standards, are among the six EPA criterion pollutants that adversely affect human health and biological ecosystems [NRC, 1991]. Ozone is a major precursor of the hydroxyl radical (OH), which plays a key role in oxidation chemistry in the troposphere. It is also considered a greenhouse gas, particularly in the upper troposphere. NO<sub>x</sub> and CO are major O<sub>3</sub> precursors produced during combustion. NO<sub>x</sub> is also emitted from soils and lightning, and CO is produced during the oxidation of anthropogenic and biogenic hydrocarbons.

Previous studies show that spring is the season of rapid transitions in trace gas concentrations and photochemical activity [Blake *et al.*, 2003; Cantrell *et al.*, 2003; Davis *et al.*, 2003; Emmons *et al.*, 2003; Y. Wang *et al.*, 2003; Kondo *et al.*, 2004]. Besides changes in solar insolation, a number of physical processes change drastically during the spring. Among them, we are particularly interested in NO<sub>x</sub> emissions from lightning and soils, convective transport, and the mixing depth in the boundary layer. These factors lead to higher surface concentrations and tropospheric columns of ozone. They also affect the

---

<sup>2</sup>This chapter is for "Modeling analysis of springtime transition of NO<sub>2</sub>, CO, and O<sub>3</sub> over North America on the basis of in situ and satellite measurements," prepared for the submission to *Journal of Geophysical Research* in 2007. Authors are Y. Choi, *et al.*

export of pollutants from North America. The following will discuss each factor and its observational constraints.

Warmer temperature and the increasing abundance of water vapor result in more frequent convection and lightning [Rind, 1998; Price, 2000; Soden, 2000]. Choi *et al.* [2005] showed that day-to-day enhancements of lightning NO<sub>x</sub> can be detected from Global Ozone Monitoring Experiment (GOME) measurements but stressed that satellite retrieval uncertainties [Martin *et al.*, 2002] must be taken into account. Edward *et al.* [2003] showed a linkage between lightning NO<sub>x</sub> over southern Africa and South America, and the Total Ozone Mapping Spectrometer (TOMS) measured O<sub>3</sub> in the tropical southern Atlantic. Therefore, lightning NO<sub>x</sub> production could be a major contributor to the increase in the tropospheric O<sub>3</sub> column over North America during the spring. In this study, we use TOMS total ozone columns and the Stratospheric Aerosol and Gas Experiment (SAGE) II stratospheric ozone columns to derive tropospheric ozone columns and investigate any trends. We then evaluate the derived tropospheric ozone columns with ozonesonde measurements. We find that CO is a good tracer for convective transport [e.g., Choi *et al.*, 2005]. In situ observations of free tropospheric CO are available from the Tropospheric Ozone Production about the Spring Equinox (TOPSE) experiment of 2000. Although the measurement region is not affected by convective transport, these measurements can be used to evaluate the results of the Measurement of Pollution In The Troposphere (MOPITT). Soil NO<sub>x</sub> emissions also increase during spring as temperature increases [Yienger and Levy II, 1995]. Although no direct in situ measurements are available to constrain this source, GOME measurements may be useful to constrain this source [e.g., Martin *et al.*, 2003; Jaegle *et al.*, 2005]. It

remains to be seen if this source is large enough to detect in the satellite measurements in the spring.

For the identification of seasonal changes in ozone, CO, and NO<sub>x</sub>, a large number of surface in situ measurements from AIRNow and Southeastern Aerosol Research and Characterization Study (SEARCH) observation networks can be examined. These networks show that one key process that affects pollutant surface concentrations is the rapid change of mixing depth during the spring [Holzworth, 1964, 1967]. Although routine meteorological measurements do not provide measurements of daytime mixing depth, 3-D CTMs can be used to determine this effect.

Regional [McKeen *et al.*, 1991; Hess *et al.*, 2000; Song and Carmichael, 2001; Choi *et al.*, 2005] and global 3-D CTM [Brasseur *et al.*, 1998; Y. Wang *et al.*, 1998; Lawrence *et al.*, 1999; Levy *et al.*, 1999; Lelieveld and Denter, 2000; Bey *et al.*, 2001; Park *et al.*, 2004a] have been developed to explain chemical and physical processes in the atmosphere. In this work, we apply the Regional chEmical trAnsport Model (REAM) [Zeng *et al.*, 2003, 2006; Choi *et al.*, 2005; Jing *et al.*, 2006; Y. Wang *et al.*, 2006, 2007] to simulate the seasonal transition of ozone and its precursors over North America during spring 2000. The model results will be evaluated based on surface, balloon, aircraft, and satellite measurements.

Through the combination of model simulations and satellite measurements, “top-down” estimates of emissions have been used to constrain “bottom-up” inventories [Leue *et al.*, 2001; Martin *et al.*, 2003, 2006; Arellano *et al.*, 2004; Jaegle *et al.*, 2004, 2005]. In this work, we apply the same approach to estimate surface NO<sub>x</sub> emissions and compare them with the a priori inventories. In particular, we test the sensitivities of the a posteriori

inventories to the air mass factor (AMF), which is calculated using the vertical profiles of  $\text{NO}_2$  from the model results. For this purpose, two model results will be used in the comparison. Finally, using the results of the REAM model, we examine the export of  $\text{O}_3$  and its precursors from the boundary layer of North America [Horowitz *et al.*, 1998; Liang *et al.*, 1998; Park *et al.*, 2004b] and the springtime transitions of pollutant exports. We also examine the vertical profiles of the import and export fluxes of these tracers and the factors affecting the fluxes.

We first described the measurement data, including the surface measurements of  $\text{O}_3$  from the EPA AIRNow network and of  $\text{NO}$ ,  $\text{CO}$ , and  $\text{O}_3$  from the surface SEARCH, aircraft measurements of  $\text{CO}$  from the TOPSE experiment and of  $\text{O}_3$  from the Measurement of Ozone and Water Vapor by Airbus In-Service Aircraft (MOZAIC) program, and ozonesondes. Satellite measurements include GOME  $\text{NO}_2$ , MOPITT  $\text{CO}$ , and TOMS-SAGE II  $\text{O}_3$ . The regional REAM and global GEOS-CHEM models are described in Section 3.3. We evaluate the REAM simulated springtime transitions of  $\text{O}_3$  and its precursors with surface, ozonesonde, aircraft, and satellite measurements in Section 3.4. In this section, we also analyze the top constraints of surface  $\text{NO}_x$  emissions and the exports of  $\text{O}_3$  and its precursors from North America. Conclusions are given in Section 3.5.

## **3.2 In situ and Satellite Measurements**

### **3.2.1 Surface Measurements**

#### ***3.2.1.1 The EPA AIRNow network***

Hourly  $O_3$  concentrations are obtained from the EPA AIRNow data archives [[www.epa.gov/ttnairs1/airsaqs/detaildata/downloadaqsddata.htm](http://www.epa.gov/ttnairs1/airsaqs/detaildata/downloadaqsddata.htm)]. The EPA network contains considerably more  $O_3$  measurement sites than  $NO_x$  and CO sites. The sites are divided into three categories: urban, suburban, and rural. Since they are more representative of the region, the 291 rural sites are used. The CO and  $NO_x$  measurements are not used because of their high method detection limits (MDL) of 0.5 ppmv of CO and 5 ppbv of  $NO_x$  [Jake Summers, Personal Comm., 2004]. However, rural CO and  $NO_x$  measurements are usually below the MDL values, reported at one-half the MDL. The MDL value for  $O_3$  was 5 ppbv. We focus on the afternoon (1300 to 1700 LT) when surface observations are more representative due to strong turbulent mixing in the planetary boundary layer (PBL).

#### *3.2.1.2 The SEARCH network*

Hourly  $O_3$ , NO, and CO are measured at eight SEARCH sites: Yorkville (YRK, rural), Jefferson Street (JST, urban), Centreville (CTR, rural), Outlying Landing Field #8 (OLF, suburban), Pensacola (PNS, urban), Gulfport (GFP, urban), Oak Grove (OAK, rural), and North Birmingham (BHM, urban). The SEARCH data of trace gases are obtained from the web [[www.atmospheric-research.com/public/index.html](http://www.atmospheric-research.com/public/index.html)]. For our analysis, we use observations from the following rural and suburban sites: YRK, CTR, OLF, and OAK. The detection limits of  $O_3$ , NO, and CO are 1 ppbv, 50 pptv, and 10 ppbv, respectively [E. S. Edgerton, Personal Comm., 2007].

#### *3.2.2 Aircraft Observations*



### 3.2.2.1 MOZAIC

The MOZAIC program was designed to automatically collect O<sub>3</sub> and water vapor data on five commercial Airbus A340 aircraft [Marenco *et al.*, 1998]. For recent updates, see <http://www.aero.obs-mip.fr/mozaic/>. We use MOZAIC O<sub>3</sub> measurements recorded from February to May 2000. For the ascent and descent portions of the flights, MOZAIC raw data (4s time resolution) are averaged over 150 m height intervals. The MOZAIC analyzer is the dual-beam UV absorption Model 49-103 from Thermo Environment Instruments [Thouret *et al.*, 1998]. The instruments are laboratory-calibrated before and after flight and re-calibrated every 12 to 18 months. During any flight operation, each instrument is checked for zero and the calibration factor using a built-in ozone generator.

### 3.2.2.2 TOPSE

The TOPSE experiment took place from February to May 2000 [Atlas *et al.*, 2003]. The objective of TOPSE was to investigate the chemical and dynamical changes in the tropospheric chemical components over North America covering the region from Colorado to north of Thule, Greenland, during the late winter to spring transition. Thirty-eight science flights were conducted in seven deployments that were one to two weeks apart. Diverse trace gases related to tropospheric O<sub>3</sub> chemistry were measured from the surface up to 8 km. Several aircraft flights between March and May are concurrent with MOPITT overpasses.

### 3.2.3 Ozonesondes

We use ozonesonde data from February to May of 2000 from six mid-latitude stations located between 35°N and 53°N: Huntsville (35°N, 87°W), Wallops Island (38°N, 75°W), Boulder (40°N, 105°W), Trinidad Head (41°N, 124°W), Richland (46°N, 119°W), and Goose Bay (53°N, 50°W). The electrochemical concentration cell (ECC) sensor is typically used and the accuracy is about  $\pm 6\%$  on the ground and -7% to 17% in the middle and upper troposphere [Komhyr *et al.*, 1995]. The ozonesonde data are mainly obtained from the World Ozone and Ultraviolet Data Center (WOUDC) [<http://www.woudc.org>].

#### 3.2.4 Satellite Retrievals

The GOME instrument is on board the European Remote Sensing-2 (ERS-2) satellite that passes over the equator at 1030 AM local time, and its horizontal resolution is 40 km latitude by 320 km longitude. The DOAS algorithm with AMF calculation is described by Chance *et al.* [2000] and Martin *et al.* [2002]: First, the slant column is determined by fitting directly backscattered radiance spectra from GOME; then a stratospheric column determined from the NO<sub>2</sub> column over the central Pacific [Martin *et al.*, 2002] is subtracted from the total column; and finally, the subtracted columns are converted to a vertical column with AMF, which is an integral of the product of the shape factor from model-calculated vertical profiles and the perturbation of backscattered radiance of NO<sub>2</sub>. The radiance perturbation due to the change of NO<sub>2</sub> is calculated from the Linearized Discrete Ordinate Radiative Transfer (LIDORT) model [Spurr *et al.*, 2001], which considers multiple scattering in the atmosphere. Data of the cloud optical depth and fraction are from GOME [Kurosu *et al.*, 1999]. The monthly mean fields of

aerosol mass concentrations are taken from the Global Ozone Chemistry Aerosol Radiation and Transport (GOCART) model [Chin, 2002], which simulates 3-D distributions of sulfate, mineral dust, sea salt, hydrophobic and hydrophilic black carbon, and organic carbon [Mian Chin, Personal Comm., 2004]. We do not use the measurements when the cloud cover is >40% [Martin *et al.*, 2002]. The retrieval uncertainties are mostly due to spectral fitting, spectral artifact related to the diffuser plate, removal of the stratospheric column, and AMF calculations [Martin *et al.*, 2002; Choi *et al.*, 2005]. The uncertainties are generally  $0.6-1.2 \times 10^{15}$  molecules  $\text{cm}^{-2}$  over the ocean and  $1.0-3.5 \times 10^{15}$  molecules  $\text{cm}^{-2}$  over the continent.

The MOPITT instrument on board the NASA Terra satellite is capable of globally monitoring CO through observations of two spectral bands: a solar band around 2.3  $\mu\text{m}$  and a thermal band around 4.6  $\mu\text{m}$ . The satellite passes over the equator at around 1045 AM and 2245 PM local time, and the horizontal resolution of MOPITT is  $22 \times 22 \text{ km}^2$ . MOPITT measures filtered radiance from the top of the atmosphere (TOA) from a gas correlation radiometer that produces gas correlation spectroscopy composed of an average response signal (A) and a different response signal (D) rather than capturing TOA radiance directly [Pan *et al.*, 1995, 1998]. If the probability distribution function (PDF) of a state vector (CO vertical profile) is proportional to that of an observed signal measured by a MOPITT instrument, an inverse problem with an ill-posed condition is resolved by minimizing a cost function. MOPITT CO columns are obtained from the data pool of the NASA Langley Atmospheric Science Data Center (ASDC). The uncertainty of CO columns, as reported by the data, averages  $2 \times 10^{17}$  molecules  $\text{cm}^{-2}$ . In our model evaluation, simulated CO concentrations are processed with the MOPITT

retrieval averaging kernel (AK), described in previous studies [Deeter *et al.*, 2003, Emmons *et al.*, 2004].

TOMS on board the Earth Probe satellite that crosses the equator at 1116 AM local time measures incident solar radiation and backscattered ultraviolet sunlight, resulting in deriving total ozone. TOMS has a horizontal resolution of  $39 \times 39 \text{ km}^2$  and a measurement uncertainty of about 5% (the random error is 2% and the systematic error is about 3%) [[ftp://toms.gsfc.nasa.gov/pub/eptoms/EARTHPROBE\\_USERGUIDE.PDF](ftp://toms.gsfc.nasa.gov/pub/eptoms/EARTHPROBE_USERGUIDE.PDF)]. SAGE II on board the Earth Radiation Budget Satellite (ERBS) measures the Earth's limb extinction via the solar occultation technique during each spacecraft sunrise and sunset. The horizontal and vertical resolutions of SAGE are about  $30 \times 250 \text{ km}^2$  and 1 km, respectively. Scatter-plots of SAGE II (retrieval version 6.2)  $\text{O}_3$  versus Potential Vorticity (PV) on isentropic surfaces are used to produce the  $\text{O}_3$  profiles in the stratosphere [Jing *et al.*, 2004], which are coincident in latitude, longitude, and time with TOMS (version 8) total column  $\text{O}_3$  measurements. When the TOMS data indicate a reflectivity less than 20%, tropospheric ozone columns are inferred by subtracting the SAGE II-based stratospheric from the TOMS columns. The PV values are obtained from the NCEP reanalysis data set, and a value of 3.5 PV units is used to define the location of the tropopause.

By comparison with the ozonesonde measurements, two previous studies [H.-J. Wang *et al.*, 2002, 2006] indicate that SAGE  $\text{O}_3$  has an accuracy of 10% or better down to the tropopause, the SAGE values being almost 5% higher than the ozonesonde values at an altitude between 15 and 20 km. A previous study [Jing *et al.*, 2004] suggested that PV mapping produces individual  $\text{O}_3$  values in the stratosphere with a precision of about

10%. Thus, the measurement uncertainties of TOMS-SAGE become about 21%. However, this error tends to be random, and stratospheric columns averaged for several days, for example, are expected to have significantly better precision, resulting in smaller measurement uncertainties of TOMS-SAGE II.

### **3.3 Model Descriptions**

#### **3.3.1 Regional chEmical trAnsport Model (REAM)**

##### *3.3.1.1 General description*

In this work, REAM has a horizontal resolution of 70 km with 23 vertical layers reaching 10 hPa, 20 of which are below 100 hPa. The National Center for Atmospheric Research/Penn State MM5 is used to simulate meteorological fields using four-dimensional data assimilation (FDDA) [Stauffer *et al.*, 1991] with the National Center for Environmental Prediction reanalysis, surface, and rawinsonde observations. Most of the meteorological variables are archived every 30 minutes, except convection and lightning, which are archived every 2.5 minutes because of the highly variable nature of these processes. The horizontal domain of MM5 has five extra grids beyond that of REAM on each side to minimize potential transport anomalies near the boundary. We use the ETA Mellor-Yamada-Janjic (MYJ) 2.5-order closure scheme [Black, 1994] for turbulent calculations.

The photochemical, dry, and wet deposition modules of REAM are adopted from the GEOS-CHEM model [Bey *et al.*, 2001]. The altitude-dependent cloud optical depth is calculated using MM5 liquid water content [Stephens *et al.*, 1978]. The UV surface albedo for photolysis rate calculations is obtained from TOMS observations [Herman and

Celarier, 1997]. The transport scheme is from Walcek [2000]. The convective scheme by Grell [1993] is implemented to be consistent with the meteorological model; sub-grid scale updraft and downdraft processes and large-scale subsidence are considered. The top and bottom layers of shallow convection are determined by MM5 simulations; the cloud fraction is determined using the scheme described by Geleyn [1981]. Previously, the model was used to analyze the effects of lightning and convection [Choi *et al.*, 2005], the trans-Pacific transport [Y. Wang *et al.*, 2006], the tropospheric O<sub>3</sub> column [Jing *et al.*, 2006], and polar tropospheric chemistry [Zeng *et al.*, 2003; Y. Wang *et al.*, 2007].

Spring 2000 GEOS-CHEM model simulations provide initial and boundary conditions for trace gases. Regional simulations are spun up in the last week of January 2000. Emission inventories for combustion and industrial sources are taken from GEOS-CHEM [Bey *et al.*, 2001], except the fossil fuel NO<sub>x</sub> and CO emission inventories over the United States, which are taken from the 1999 US Environmental Protection Agency National Emission Inventory (NEI99). These values are scaled with the national total emissions of 2000 [EPA, 2003]. Emission algorithms for vegetation and soils are taken from GEOS-CHEM, but meteorological inputs are from MM5. The monthly mean leaf area index (LAI) distribution is derived from 1-km Advanced Very High Resolution Radiometer data [Bonan *et al.*, 2002]. The lightning NO<sub>x</sub> algorithm follows.

#### *3.3.1.2 Lightning NO<sub>x</sub> parameterizations*

NO<sub>x</sub> production due to lightning is estimated and distributed vertically up to the cloud top layer in the model. NO<sub>x</sub> is primarily produced during the high-energy return stroke phase of a flash [Price *et al.*, 1997]. There are two flash types: cloud-to-ground

(CG) and intracloud (IC) flashes. The NO produced per IC flash is estimated to be one-tenth that of a CG flash ( $6.7 \times 10^{26}$  NO molecules flash<sup>-1</sup>) in some previous studies [Price *et al.*, 1997; Pickering *et al.*, 1998; Allen *et al.*, 2000; Allen and Pickering, 2002]. Higher or equivalent NO production per IC as CG flash is used in several more recent studies [DeCaria *et al.*, 2000; Ott *et al.*, 2003; Zhang *et al.*, 2003; Fehr *et al.*, 2004; Choi *et al.*, 2005]. Based on cloud-resolving modeling output compared with anvil aircraft NO<sub>x</sub> observations over the U.S., the average NO production per flash for both IC and CG flashes is about  $2\text{--}4 \times 10^{26}$  molecules [K. Pickering, Personal Comm., 2005]. Ott *et al.* [2003] use  $3.0 \times 10^{26}$  NO molecules per flash for IC and CG flashes. We assume that NO production per IC flash is the same as that per CG flash. The NO production rate per flash used by Choi *et al.* [2005] is  $6 \times 10^{26}$  NO molecules per flash. Sensitivity results suggest that this value gives better agreement with GOME measurements. Lightning NO<sub>x</sub> is distributed vertically following the mid-latitude profile by Pickering *et al.* [1998].

Two separate parameterizations are constructed for continental and oceanic regions [Price and Rind, 1993] using measurements from the National Lightning Detection Network (NLDN). The detection efficiency reported by Cummins *et al.* [1998] is used. We parameterize the lightning NO<sub>x</sub> production rate as a function of meteorological variables so that this emission is consistent with the dynamic model. Using the parameterizations, we experimented with cloud top height [Price and Rind, 1993], convective mass flux [Allen and Pickering, 2002], and convective available potential energy (CAPE) [Choi *et al.*, 2005]. To take advantage of the different distributions, we use both CAPE and cloud mass flux and had to normalize them. The CG

flashing rate for continental and oceanic regions are mathematically expressed in terms of normalized convective mass flux (M) and CAPE (C):

$$LF_{cg} = a_o + aM + bM^2 + cM^3 + dC + eC^2 + fC^3 + gMC + hM^2C + iMC^2 + jM^4 + kM^3C + lM^2C^2 + mMC^3 + nC^4,$$

where for continental regions,  $a_o = 0.00495$ ,  $a = 4.219$ ,  $b = 15.5064$ ,  $c = -112.492$ ,  $d = -2.089$ ,  $e = 48.143$ ,  $f = -53.983$ ,  $g = -121.956$ ,  $h = 358.118$ ,  $i = 208.105$ ,  $j = 108.613$ ,  $k = -216.226$ ,  $l = -330.354$ ,  $m = -134.307$ ,  $n = 16.742$  and for ocean regions,  $a_o = 0.126$ ,  $a = 2.669$ ,  $b = -0.854$ ,  $c = -61.793$ ,  $d = -2.482$ ,  $e = 24.35$ ,  $f = 26.739$ ,  $g = -31.732$ ,  $h = 288.129$ ,  $i = -185.419$ ,  $j = 63.089$ ,  $k = -178.063$ ,  $l = -151.659$ ,  $m = 204.120$ ,  $n = -34.408$ . Once the CG flashing rate is determined, the IC to CG flash rate ratio is calculated following Y. Wang *et al.* [1998].

### 3.3.2 Global Earth Observing System (GEOS)-CHEM

GEOS-CHEM is driven by GEOS assimilated meteorological fields (GEOS-3) for 2000 [Schubert *et al.*, 1993]. The horizontal resolution of GEOS-CHEM is 2° latitude by 2.5° longitude. Thirty chemical tracers describing tropospheric O<sub>3</sub> chemistry are transported. Detailed algorithms for photochemistry, dry and wet deposition, and emissions are described by Bey *et al.* [2001]. Chemical initial and hourly boundary conditions for REAM are taken from GEOS-CHEM model simulations (version 7.2) [Bey *et al.*, 2001]. In addition, the results of GEOS-CHEM are compared with those of the REAM simulations.



### 3.4 Seasonal Transitions of NO<sub>x</sub>, CO, and O<sub>3</sub>

#### 3.4.1 Nitrogen Oxides (NO<sub>x</sub> = NO+NO<sub>2</sub>)

##### 3.4.1.1 Time series of SEARCH NO

We compare REAM simulated NO mixing ratios with SEARCH observations at four rural or suburban sites, CTR, OAK, OLF, and YRK, during February and May of 2000, in order to examine the seasonal trends of surface NO data. Hourly NO concentrations vary significantly between day and night because of the shallow boundary layer at night. We show only daily 1-5 pm (LT) NO comparisons between SEARCH and REAM (Figure 3.1). Simulated mean NO concentrations during the four months (CTR: 290 pptv, OAK: 216 pptv, OLF: 314 pptv, YRK: 936 pptv) agree with the observed means (240 pptv, 241 pptv, 275 pptv and 1048 pptv) to within 10% and 20%. The correlation coefficients between REAM and SEARCH NO are 0.66, 0.56, 0.40, and 0.23 at the sites. High NO peaks at YRK are due to nearby power plant emissions [B. Hartsell and E. S. Edgerton, Personal Comm., 2006]. The model resolution is too coarse to simulate the influence of power plant plumes. As a result, of the four sites, YRK has the lowest correlation coefficient. Decreasing NO concentrations from spring to summer are clear from both observations and REAM simulations, reflecting in part an increasing photochemical loss of NO<sub>x</sub>.

##### 3.4.1.2 GOME tropospheric NO<sub>2</sub> column

###### 3.4.1.2.1 Dependence of GOME NO<sub>2</sub> retrievals on the a priori profiles

The monthly means of tropospheric NO<sub>2</sub> columns derived from GOME measurements are calculated between February and May 2000 in order to investigate

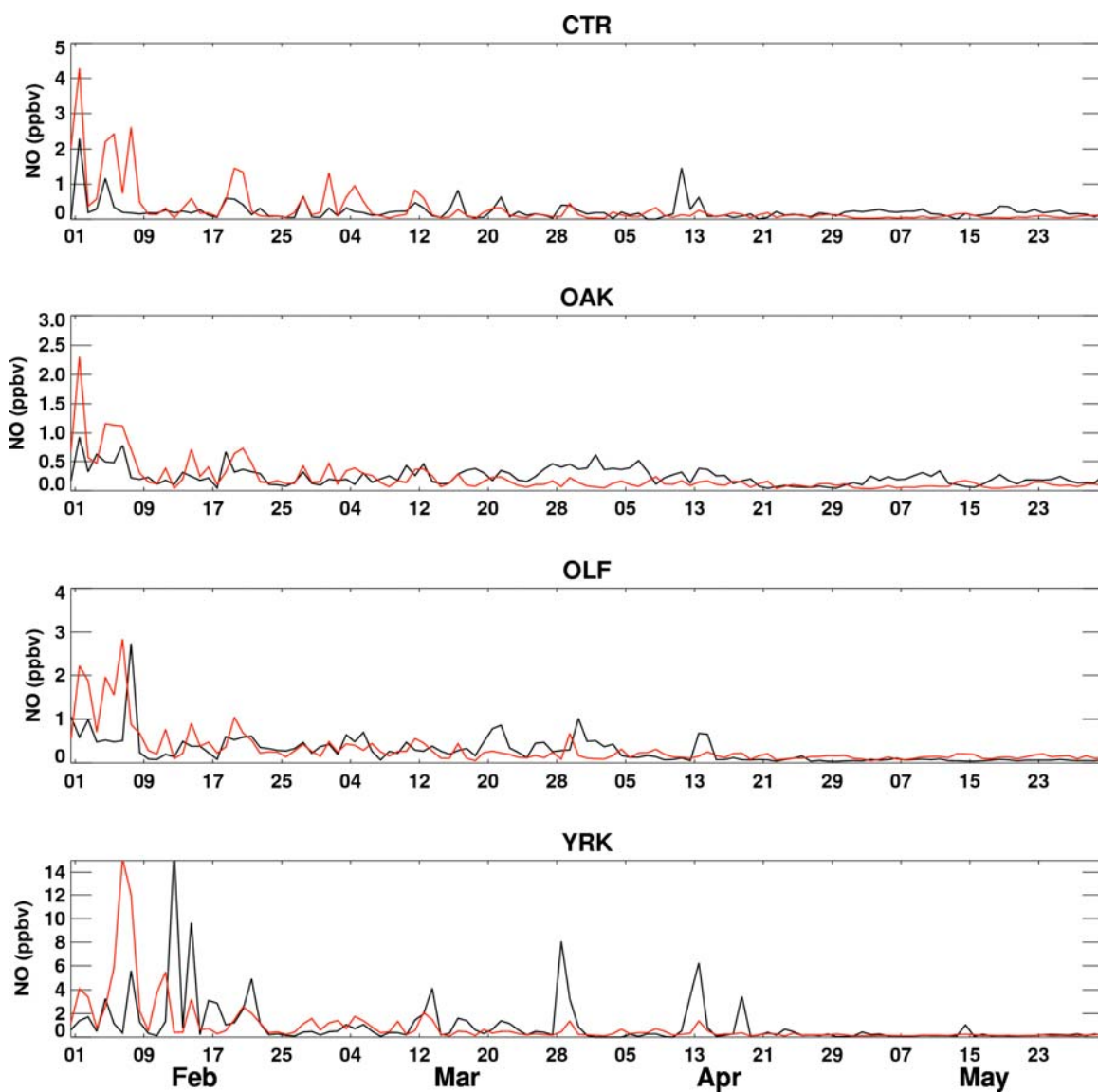


**Figure 3.1** Averaged observed and simulated NO mixing ratios (ppbv) during the afternoon (1300-1700, LT) at four SEARCH surface sites: Centerville (CTR), Oak Grove (OAK), Outlying Landing Field #8 (OLF), and Yorkville (YRK). The solid black lines represent the SEARCH measurements and red lines the REAM results.

seasonal changes in tropospheric NO<sub>2</sub> patterns. The retrieval process is described in Section 3.2.4. Both GEOS-CHEM and REAM vertical profiles are applied to calculate the AMFs as a way of examining the sensitivity of GOME retrievals to the simulated NO<sub>2</sub> vertical profiles. GEOS-CHEM and REAM have different profiles due in part to the shallower boundary layers in MM5 than GEOS-3 (to be discussed in Section 3.4.3.3). Despite the differences in the NO<sub>x</sub> profiles (to be shown in Figure 3.11), Figure 3.2 shows good agreement between GOME NO<sub>2</sub> column retrievals using the REAM and GEOS-CHEM profiles. The correlation coefficient is > 0.99. The monthly mean NO<sub>2</sub> columns of the retrievals using REAM profiles are higher by 6.1, 12.0, 5.5, and 0.4% from February to May than that using GEOS-CHEM because the AMF values are smaller. Generally, about 40% is used to calculate the AMF-associated retrieval uncertainty for each datum [Martin *et al.*, 2002], which is in agreement with our results.

#### 3.4.1.2.2 Comparisons of the model results with GOME NO<sub>2</sub> retrievals

Figure 3.2 also shows that the REAM and GEOS-CHEM simulated NO<sub>2</sub> columns are generally in agreement with the GOME NO<sub>2</sub> retrievals. The mean biases are within 11%, and the correlations are high ( $R > 0.85$ ). In February, compared with GOME observations, both models overestimate the NO<sub>2</sub> columns due to the negative retrieval values over high-latitude regions. While REAM tends to overestimate GOME NO<sub>2</sub> columns in April and May due to larger lightning NO<sub>x</sub> productions in REAM, GEOS-CHEM tends underestimate them in the same months.

Due to its coarse spatial resolution, the GEOS-CHEM model fails to capture NO<sub>2</sub> column peaks ( $> 5 \times 10^{15}$  molecules cm<sup>-2</sup>) in California, but REAM captures GOME NO<sub>2</sub>

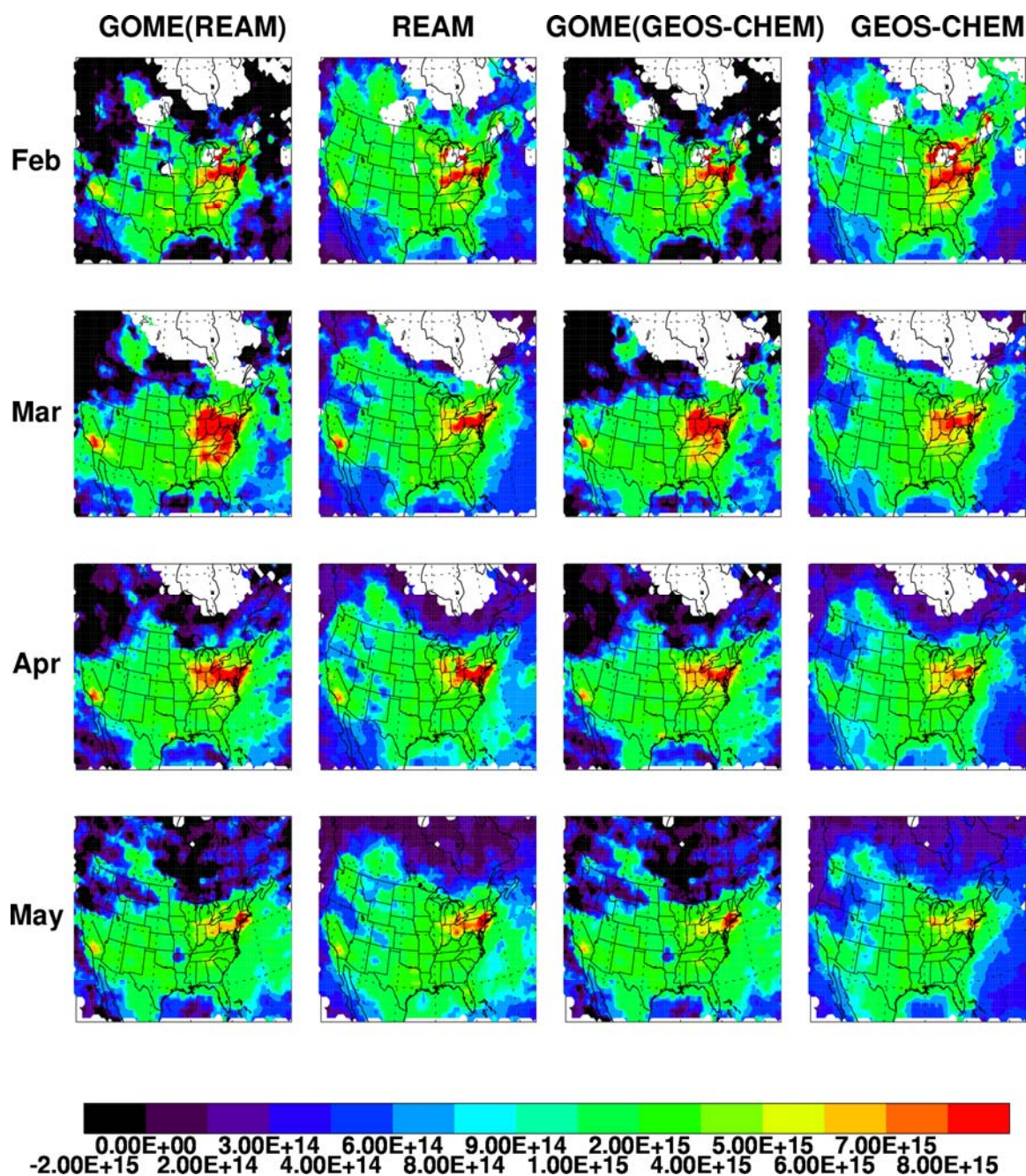


**Figure 3.2** Monthly mean tropospheric NO<sub>2</sub> vertical columns (in molecules cm<sup>-2</sup>) during February-May 2000 from GOME retrievals using the REAM-derived shape factor (first column), the REAM model (second), GOME retrievals using the GEOS-CHEM-derived shape factor (third), and the GEOS-CHEM model (last). The text provides more details. The model results are obtained by averaging NO<sub>2</sub> data during the satellite overpass time period (1000-1100, LT).

columns. In April and May, both models slightly underestimate NO<sub>2</sub> columns in the western United States likely due to underestimated soil NO<sub>x</sub> emissions [Martin *et al.*, 2003; Bertram *et al.*, 2005; Jaegle *et al.*, 2005]. The GEOS-CHEM model also underestimates NO<sub>2</sub> columns in GOME over the western North Atlantic due to their lower lightning NO<sub>x</sub> production over the region.

#### 3.4.1.2.3 NO<sub>2</sub> column sensitivities to lightning and soil emissions and convection

We compute the contributions of lightning production, convective transport, and soil emissions by comparing sensitivity simulations with each process turned off and the standard REAM simulation. Figure 3.3 shows monthly mean column differences between the standard model and sensitivity simulations. The largest impact on the tropospheric NO<sub>2</sub> column appears to be from lightning production, and enhancements are found over the southern United States, the Gulf, and the western North Atlantic. The smallest impact is from convection, and some enhancements are seen over western Texas and some regions of the western North Atlantic Ocean. Enhancements from soil emissions are seen over the central United States.

In contrast to the decreasing trend of tropospheric NO<sub>2</sub> columns (Figure 3.2), lightning and soil contributions increase significantly as solar insolation and atmospheric moisture increase. Surface heating and abundant moisture, which lead to more convection and lightning and soil emissions, are driven in part by surface temperature. The lightning and soil emission contributions increase to about 10% and 7%, respectively, in May. The contribution of lightning is larger than that of soil emission, except in February.



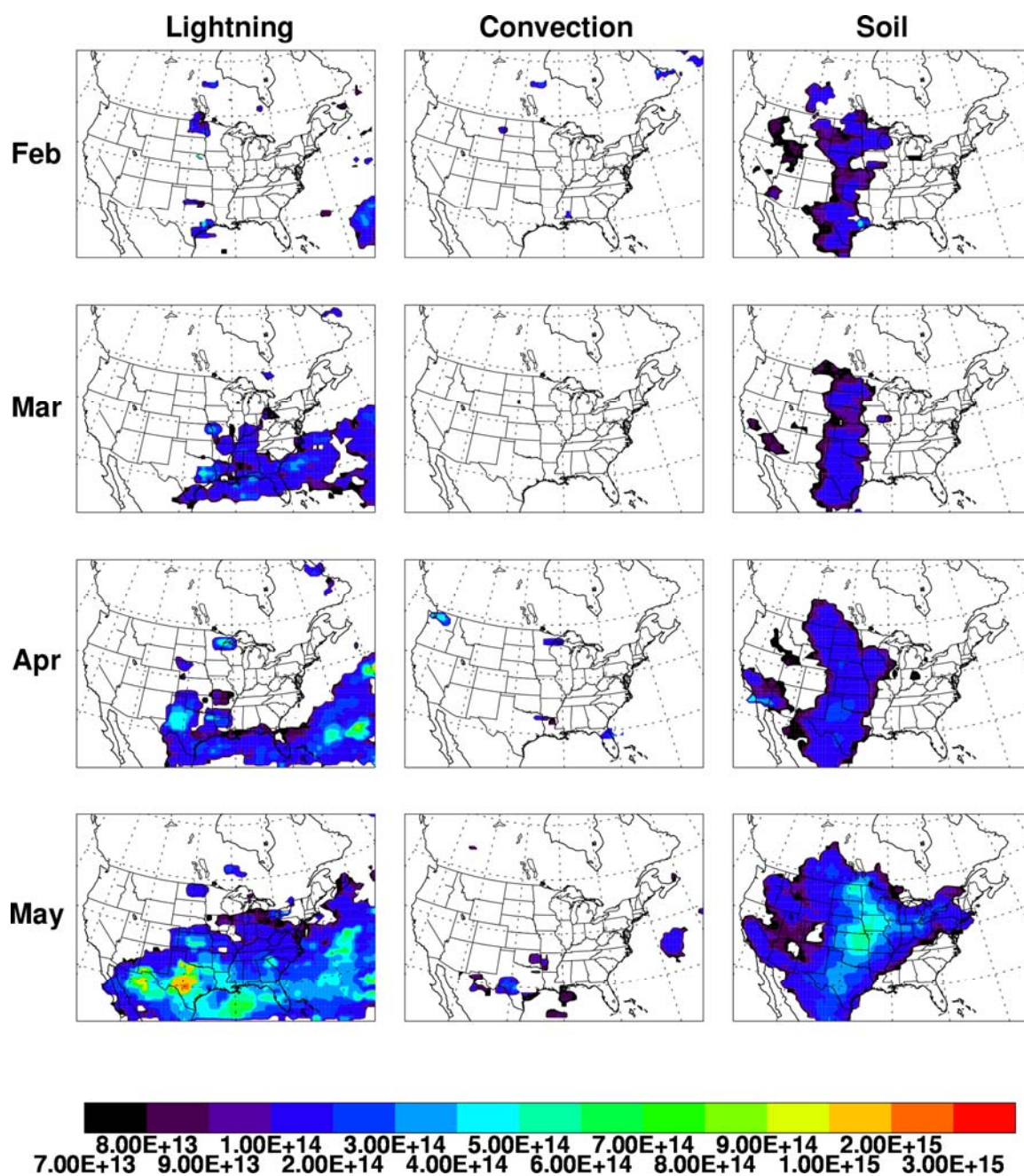


**Figure 3.3** The monthly mean contributions of lightning production, convection, and soil emissions to tropospheric  $\text{NO}_2$  vertical columns (in molecules  $\text{cm}^{-2}$ ).

In February and March, lightning NO<sub>2</sub> enhancements are typically less than  $3.0 \times 10^{14}$  molecules cm<sup>-2</sup>, but in April and May, they increase to  $0.5 - 2.0 \times 10^{15}$  molecules cm<sup>-2</sup> over the southern United States, the Gulf, and the western North Atlantic. By using an algorithm in Martin *et al.* [2002], we estimate monthly mean uncertainties for GOME retrievals to  $1 - 2 \times 10^{14}$  molecules cm<sup>-2</sup> over the ocean and  $1 - 8 \times 10^{14}$  molecules cm<sup>-2</sup> over the continent. Therefore, the detection of lightning enhancements is much easier over the ocean than it is on land. Large enhancements from lightning and soil emissions simulated in May are larger than the retrieval errors on a monthly mean basis.

#### 3.4.1.3 Optimization of fossil fuel NO<sub>x</sub> emissions

Optimized NO<sub>x</sub> emissions are estimated by combining top-down NO<sub>x</sub> emissions from satellite measurements with a priori bottom-up emissions, weighted by relative errors for the two estimates [Martin *et al.*, 2003]. NO<sub>x</sub> emission inventories used in REAM [Choi *et al.*, 2005; Jing *et al.*, 2006; Y. Wang *et al.*, 2006] and GEOS-CHEM [Bey *et al.*, 2001; Martin *et al.*, 2002, 2003; Jaegle *et al.*, 2005] are used as a priori bottom-up emissions. REAM and GEOS-CHEM use the same EPA 1999 NEI inventory for surface fossil fuel NO<sub>x</sub> emissions in the United States.

The top-down NO<sub>x</sub> fossil fuel emission inventory ( $E_t$ ) is first calculated following Martin *et al.* [2003] by fitting  $E_t$  to a priori bottom-up emission  $E_a$  with the ratio of the retrieved NO<sub>2</sub> column ( $\Omega_r$ ) to the simulated column ( $\Omega_s$ ):

$$E_t = E_a \times \Omega_r / \Omega_s . \quad (3.1)$$

Monthly a posteriori emissions ( $E$ ) are then calculated by the weighted averages of  $E_a$  and  $E_t$  [Martin *et al.*, 2003]:

$$\ln E = \frac{(\ln E_t)(\ln \varepsilon_a)^2 + (\ln E_a)(\ln \varepsilon_t)^2}{(\ln \varepsilon_a)^2 + (\ln \varepsilon_t)^2}, \quad (3.2)$$

where  $\varepsilon_a$  and  $\varepsilon_t$  are the a priori inventory and retrieval errors, respectively. The inventory errors are from a study by Martin *et al.* [2003]. Table 3.1 shows the monthly a priori, top-down, and a posteriori emissions derived using REAM and GEOS-CHEM results, respectively. The a priori emissions from REAM and GEOS-CHEM are almost the same, but the top-down estimates sometimes differ significantly. The top-down emissions

**Table 3.1** Monthly North America (20 - 62°N) fossil fuel NO<sub>x</sub> emissions (Tg N month<sup>-1</sup>)

	REAM derived			GEOS-CHEM derived		
	A priori	Top-down	A posteri	A priori	Top-down	A posteri
Feb	0.57	0.49	0.52	0.55	0.41	0.47
Mar	0.61	0.76	0.69	0.61	0.66	0.64
Apr	0.59	0.66	0.63	0.58	0.64	0.61
May	0.61	0.59	0.60	0.60	0.71	0.66
Avg.	0.60	0.63	0.61	0.59	0.61	0.60

derived by REAM are larger by 3% to 16% than those of GEOS-CHEM between February and April, but lower by 20% than those of GEOS-CHEM in May. REAM generally has lower mixing depths than GEOS-CHEM, which results in lower AMFs and higher NO<sub>2</sub> retrievals (discussed previously). Therefore, the emissions derived by REAM are usually larger than those derived by GEOS-CHEM. In May, however, REAM has larger lightning NO<sub>x</sub> production than GEOS-CHEM, which results in smaller top-down emissions.

Optimized emissions derived by REAM are 3% to 9% higher than those derived by GEOS-CHEM during the period of February to April, but lower by 10% in May. Differences between the two a posteriori emissions are caused by top-down emissions.



The seasonal agreement between top-down and a posteriori emissions are fortuitous because the boundary layer height and lightning  $\text{NO}_x$  production differences in the models are not correlated. We note that the difference between the two model-derived a posteriori emissions is well within the uncertainties of the GOME  $\text{NO}_2$  retrievals. The large month-to-month variation in top-down emissions also suggests that this approach requires that GOME measurements be taken throughout the entire season.

### 3.4.2 Carbon Monoxide

#### 3.4.2.1 *Time series of SEARCH CO*

Figure 3.4 shows a comparison of REAM simulations with SEARCH surface CO measurements between February and May. The seasonal change in CO is small during the spring. Increasing CO loss due to increasing OH oxidation is compensated by faster CO production from VOC oxidation. Observations show that simulated seasonal change is small. REAM also simulates multi-day variations in CO observations reasonably well, but the simulated mean CO concentrations (CTR: 242 ppbv, OAK: 213 ppbv, OLF: 228 ppbv and YRK: 261 ppbv) are higher than the observed concentrations (CTR: 226 ppbv, OAK: 187 ppbv, OLF: 168 ppbv and YRK: 193 ppbv). The EPA NEI emissions used in the model may also have a high bias. The correlation coefficients between hourly REAM simulations and SEARCH CO observations are 0.52, 0.56, 0.63, and 0.48 at the four sites, respectively.

#### 3.4.2.2 *MOPITT CO*

##### 3.4.2.2.1 *Evaluation of MOPITT CO with TOPSE observations*

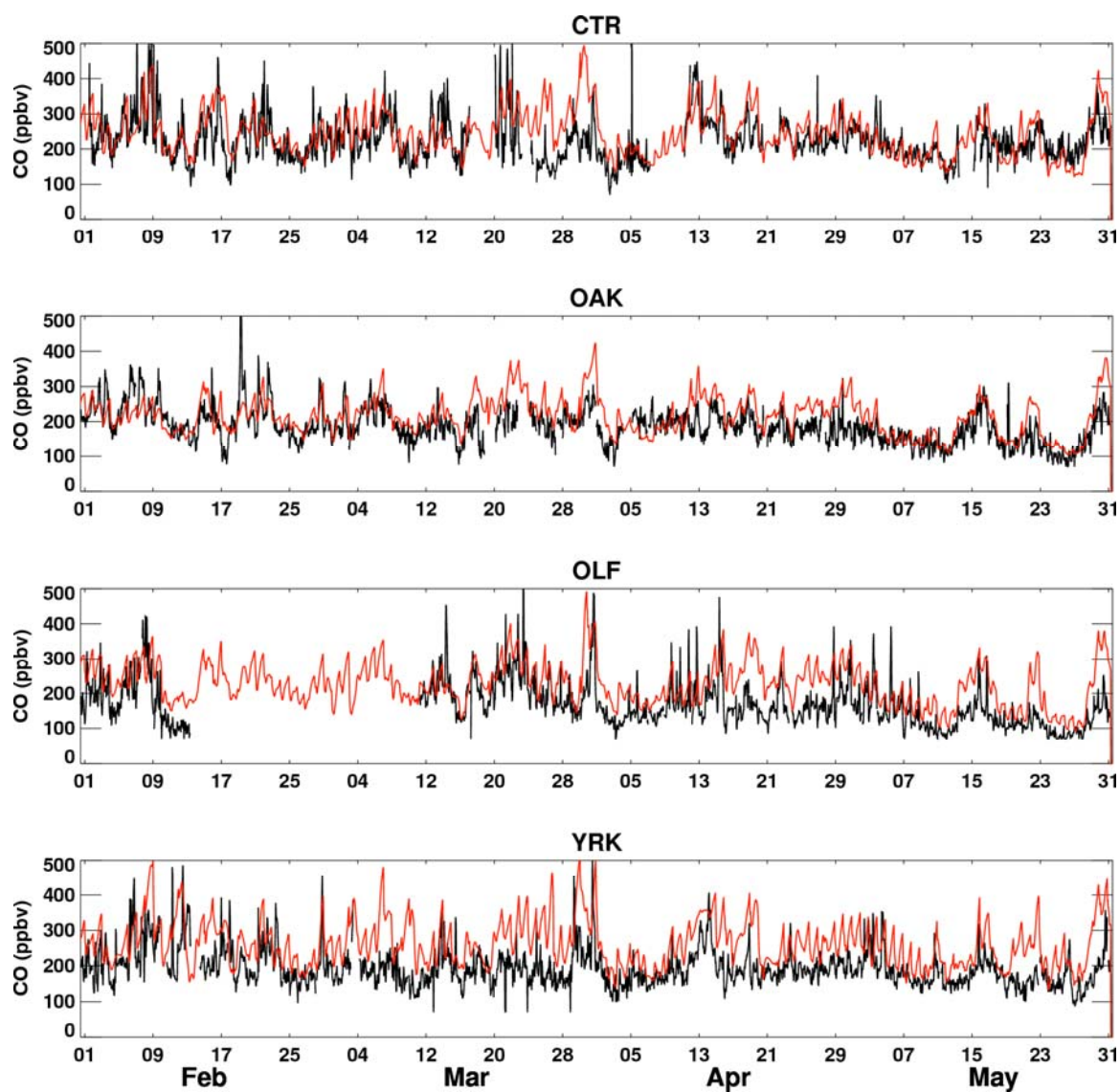


**Figure 3.4** The same as Figure 3.1, but for hourly observed and REAM simulated CO mixing ratios at four surface SEARCH sites.

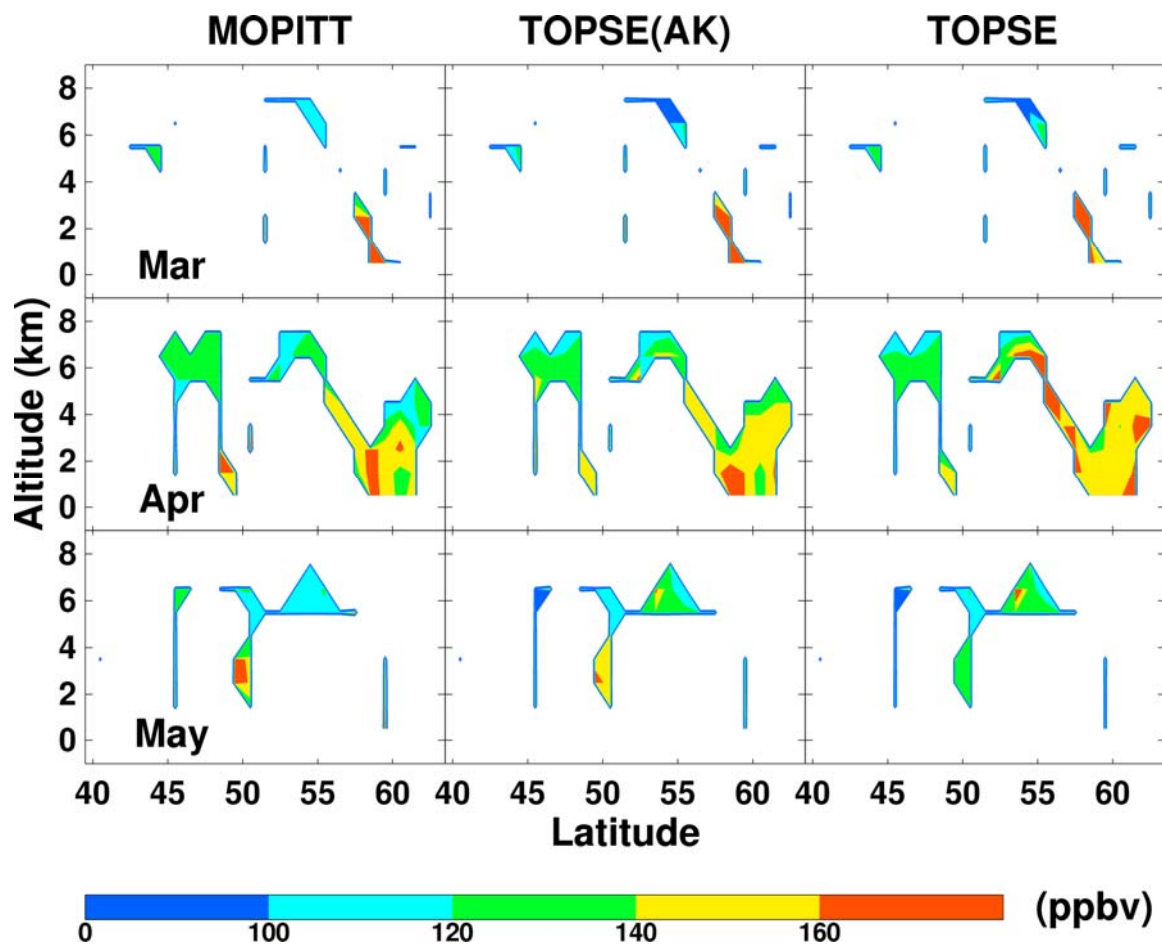


**Figure 3.5** The monthly mean cross sections of the MOPITT CO concentrations (ppbv) (left column) along TOPSE aircraft tracks, corresponding TOPSE CO concentrations processed with the MOPITT averaging kernel (middle), and TOPSE CO observations (right). Data selection criteria are described in the text.

TOPSE CO observations processed with MOPITT AK are compared with MOPITT CO observations (Figure 3.5) in order to validate MOPITT retrievals. In order to maximize data coverage, we use TOPSE observations as long as MOPITT passing over the same region was within a day. MOPITT retrievals with a priori fraction <60 % are used. MOPITT CO retrievals are in reasonably good agreement with AK-processed TOPSE CO concentrations, although high CO peaks from TOPSE observations near 6 km, particularly in May. Those high peaks are caused by long-range trans-Pacific transports in the upper troposphere [Y. Wang *et al.*, 2006]. These upper tropospheric enhancements are not captured by MOPITT mostly likely due to the low vertical resolution of MOPITT measurements [Deeter *et al.*, 2004].

To further illustrate the AK effects, we group the MOPITT CO profiles along the TOPSE flight tracks into three latitudinal bins ( $< 52^{\circ}\text{N}$ ,  $52\text{-}57^{\circ}\text{N}$ ,  $>57^{\circ}\text{N}$ ), as a vertical sampling by TOPSE is inadequate to construct the profiles (Figure 3.5). We obtain a ratio of TOPSE measurements to REAM simulations at the measurement altitudes and then apply the ratio-to-scale REAM simulations for the altitudes without measurements. Figure 3.6 shows the regional profile comparison for March to May 2000. Close agreement between MOPITT and TOPSE-REAM is found except in May at higher latitudes because very few TOPSE measurements went into the profile. In addition, after AK processing, the vertical information in the TOPSE-REAM profiles is clearly lost.

#### *3.4.2.2.2 Comparison of simulated CO columns with MOPITT*

For the model evaluation, we compare only the column concentrations because of insufficient vertical information obtained from MOPITT measurements. During March

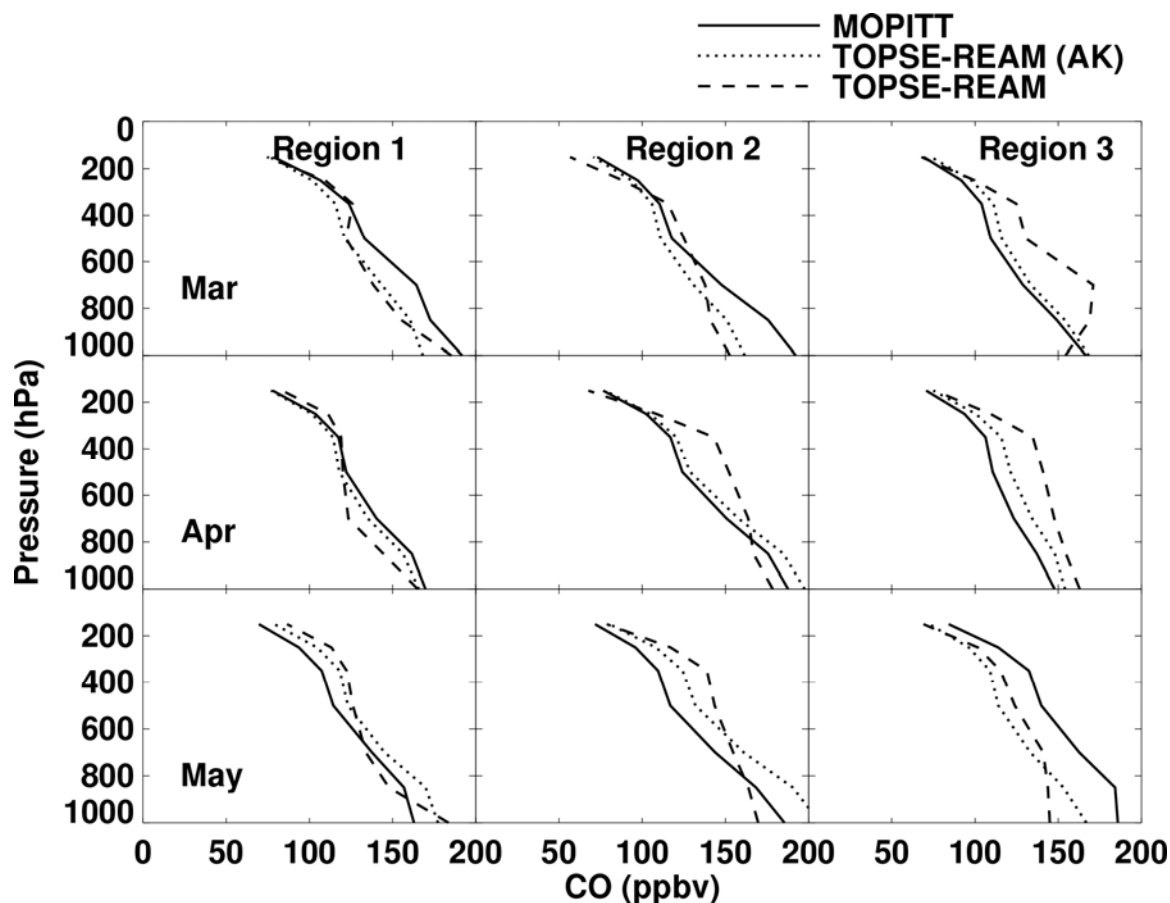


**Figure 3.6** Regional profiles by latitudes for the MOPITT measurements and the TOPSE-REAM results with and without AK processing. Region 1 covers the lower-latitude region of the TOPSE aircraft campaign (latitude  $< 52^{\circ}\text{N}$ , in the left column), region 2 the middle-latitude region ( $52^{\circ}\text{N} < \text{latitude} < 57^{\circ}\text{N}$ , in the middle column), and region 3 the higher-latitude region (latitude  $> 57^{\circ}\text{N}$ , in the right column). The scaling of the REAM results with the TOPSE measurements is explained in the text.

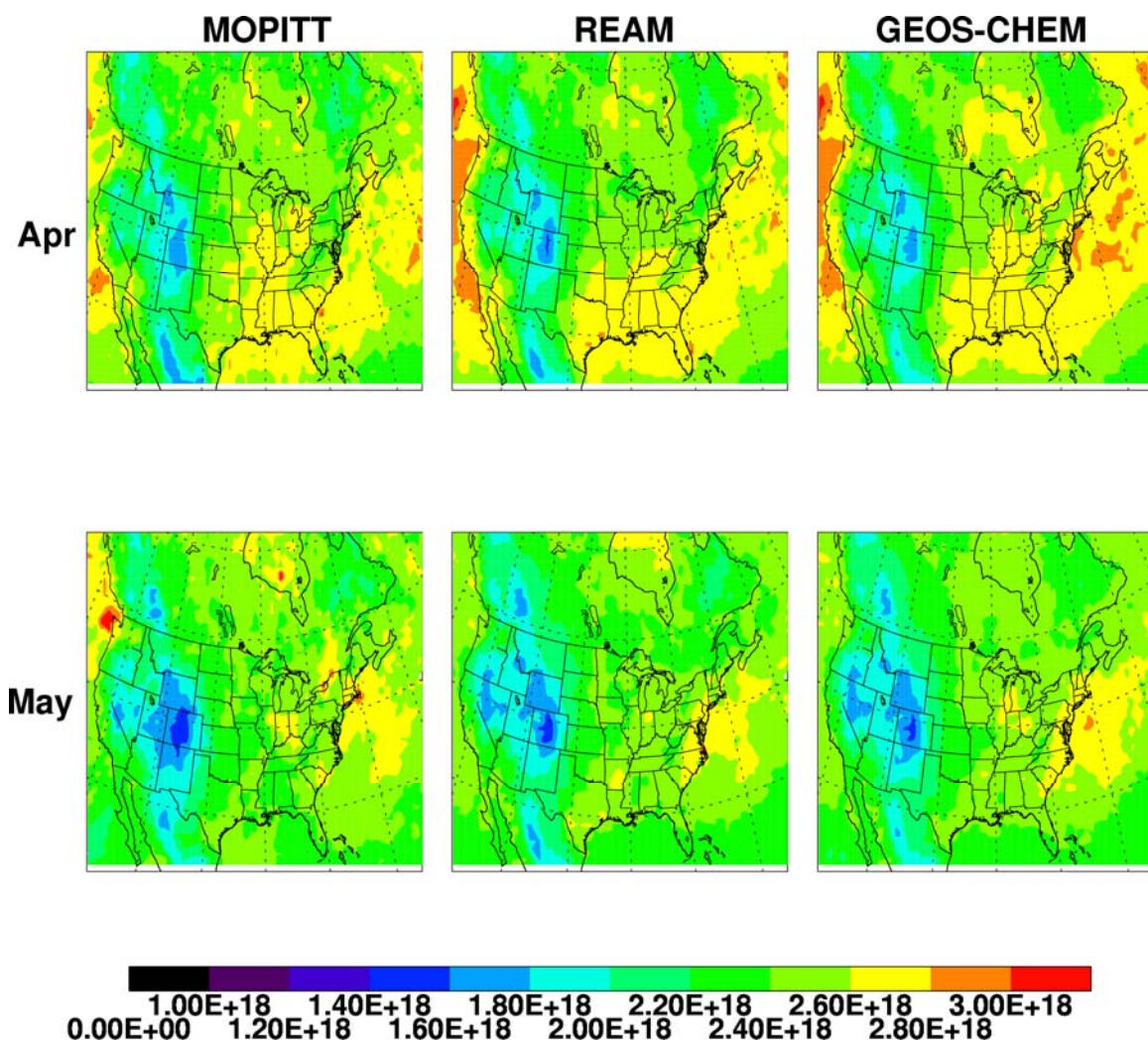


**Figure 3.7** Mean CO columns (in molecules  $\text{cm}^{-2}$ ) from MOPITT (left panel) during April-May of 2000, the corresponding REAM CO columns processed with the MOPITT averaging kernel (middle), and the GEOS-CHEM CO columns processed with the averaging kernel (right). Model results are sampled at the MOPITT measurement time and location.

2000, the first month when MOPITT data were collected, large amounts of data are missing due to calibrations. Therefore, we show only comparisons in April and May 2000. REAM and GEOS-CHEM CO columns processed using MOPITT AK reproduce MOPITT CO retrievals well (Figure 3.7). The correlation coefficients between simulated and MOPITT monthly mean CO columns are about 0.9 for both REAM and GEOS-CHEM. REAM mean biases are 1.1 and -1.1% in April and May, respectively. The GEOS-CHEM mean biases are 2.45% and -0.49%, respectively. REAM mean columns are slightly lower than GEOS-CHEM due to the lower mixing depth in REAM (to be discussed in Section 3.4.3.3).

### 3.4.3 Ozone

#### 3.4.3.1 Time series of SEARCH surface $O_3$

REAM simulated  $O_3$  concentrations are compared with SEARCH observations from February to May 2000 (Figure 3.8). In addition to capturing background concentrations and multi-day episodes of  $O_3$ , REAM reproduces the gradual increase in surface  $O_3$  at SEARCH sites well from spring to early summer. Simulated mean  $O_3$  concentrations during the four months (CTR: 34 ppbv, OAK: 38 ppbv, OLF: 42 ppbv and YRK: 33 ppbv) are in good agreement with observed mean concentrations (CTR: 38 ppbv, OAK: 43ppbv, OLF: 40 ppbv and YRK: 36 ppbv). The correlation coefficients between hourly REAM simulations and SEARCH observations at these sites are 0.69, 0.69, 0.65 and 0.68, respectively.

#### 3.4.3.2 Monthly mean EPA AIRNow $O_3$



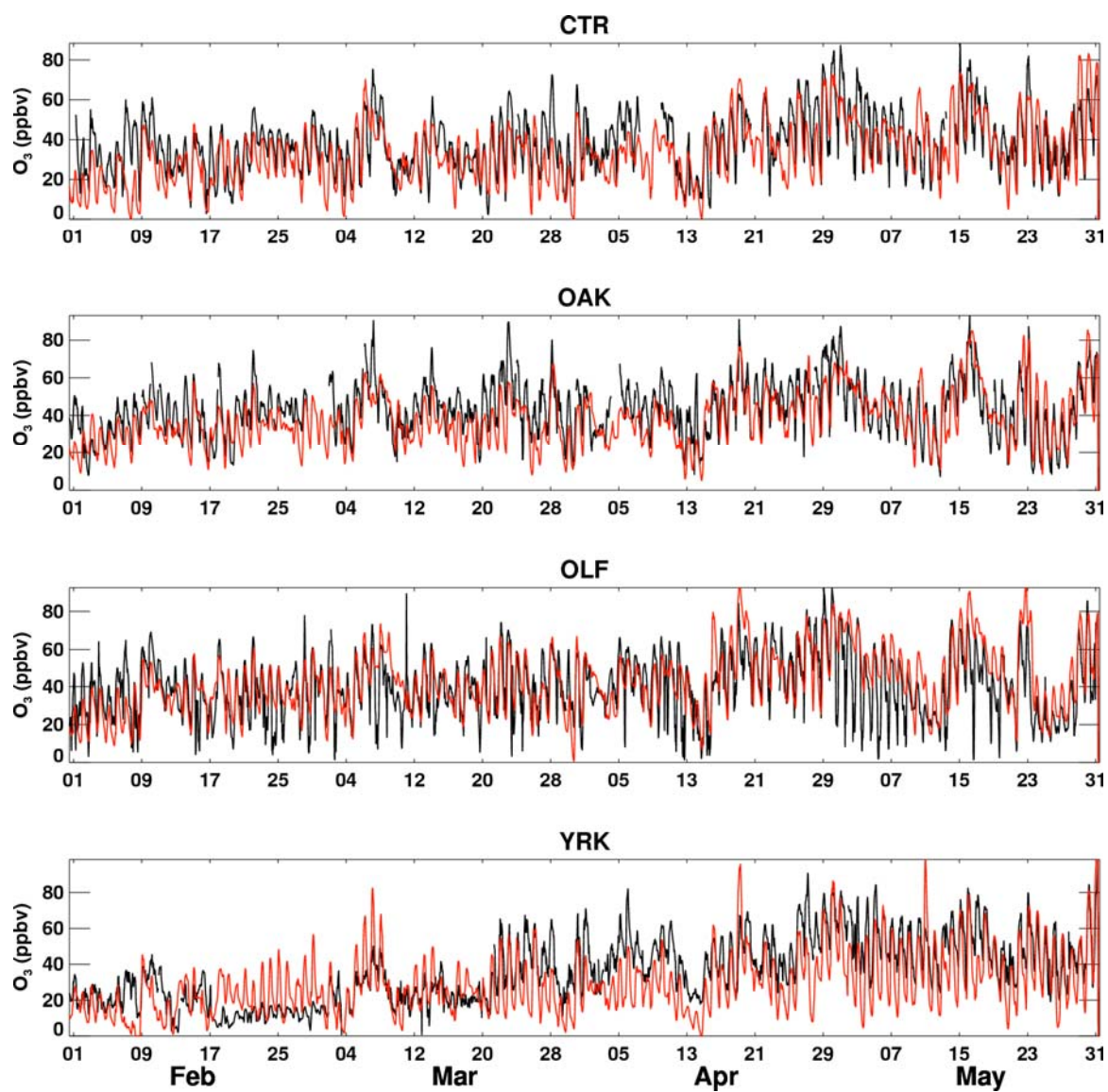


**Figure 3.8** The same as Figure 3.4 but for surface  $O_3$ . The black lines are SEARCH measurements, and the red lines are REAM results.



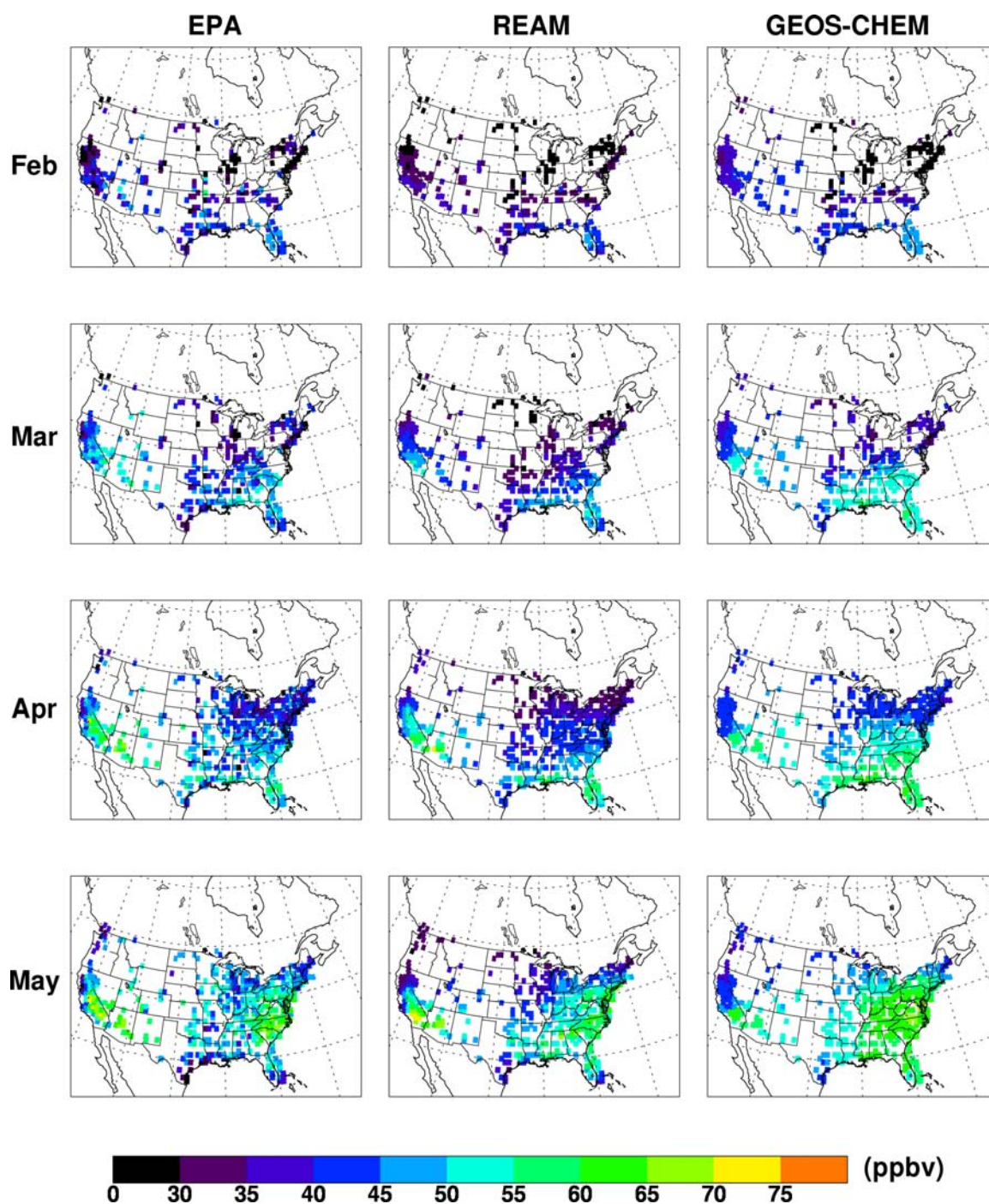


**Figure 3.9** Monthly mean afternoon (1300-1700, LT) surface  $O_3$  concentrations (ppbv) over the United States in February-May 2000. Shown are the EPA AIRNow observations (left column), the REAM simulation results (middle), and the GEOS-CHEM simulation results (right).

Monthly mean afternoon (1300-1700, LT) O<sub>3</sub> concentrations measured by the EPA AIRNow surface sites are compared with REAM and the GEOS-CHEM simulations from February to May (Figure 3.9). High O<sub>3</sub> peaks are generally captured by REAM to within 10 ppbv. The correlation coefficients of the REAM results and the EPA measurements range between 0.56 and 0.65. The correlation coefficients of the GEOS-CHEM results and the EPA observations range from 0.44 to 0.68. The correlations of the GEOS-CHEM and EPA observations decrease as the season progresses towards summer. Surface O<sub>3</sub> concentrations are low in February in part because weak solar influx limits photochemical activity. In addition, the titration of O<sub>3</sub> by high NO emissions from automobiles and power plants can occur. As the season progresses towards summer, increasing solar influx and water vapor activates photochemistry [Y. Wang *et al.*, 2003]. Both REAM and GEOS-CHEM simulate a resulting increase in surface O<sub>3</sub>. The rate of photochemical activation and surface O<sub>3</sub> increase are better simulated in REAM than in GEOS-CHEM. The global model simulates higher O<sub>3</sub> concentrations over the eastern United States in April and May than the EPA observations. Inspections of the model difference between REAM and GEOS-CHEM reveal that a major contributing factor is the differences in the mixing heights used in the model.

#### 3.4.3.3 *Mixing depth and surface O<sub>3</sub>*

From February to May, both MM5 and GEOS-3 predict increasing boundary layer mixing depths as solar insolation increases (Figure 3.10). However, MM5 predicted mixing depths used in REAM are in general lower than GEOS-3 predictions used in GEOS-CHEM. The difference is particularly large over the eastern United States, where

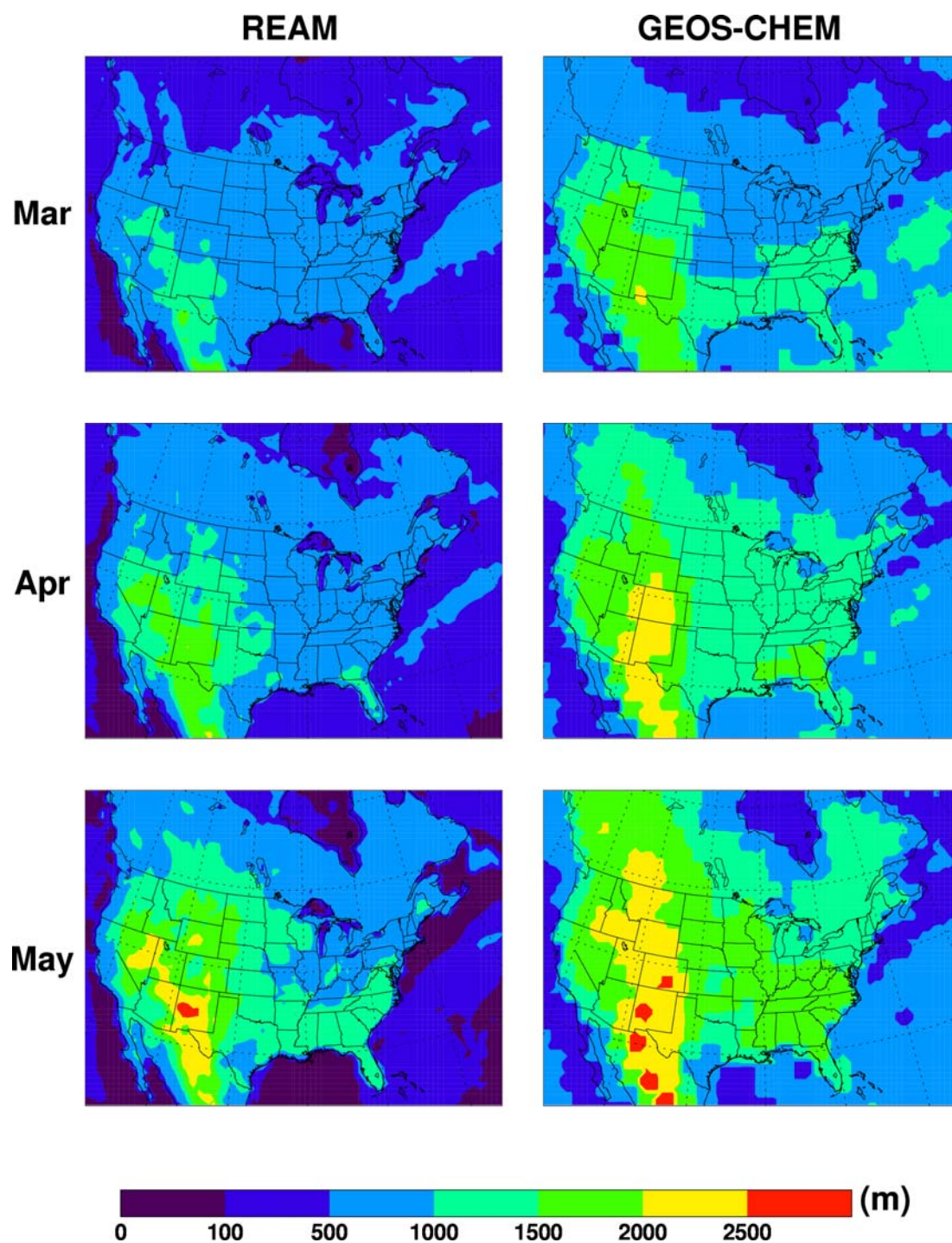


**Figure 3.10** Average afternoon (1200-1600, LT) mixing depths over North America in February-May 2000. The data used in REAM (left column) are simulated by MM5, and those used in GEOS-CHEM (right column) are simulated by GEOS-3.

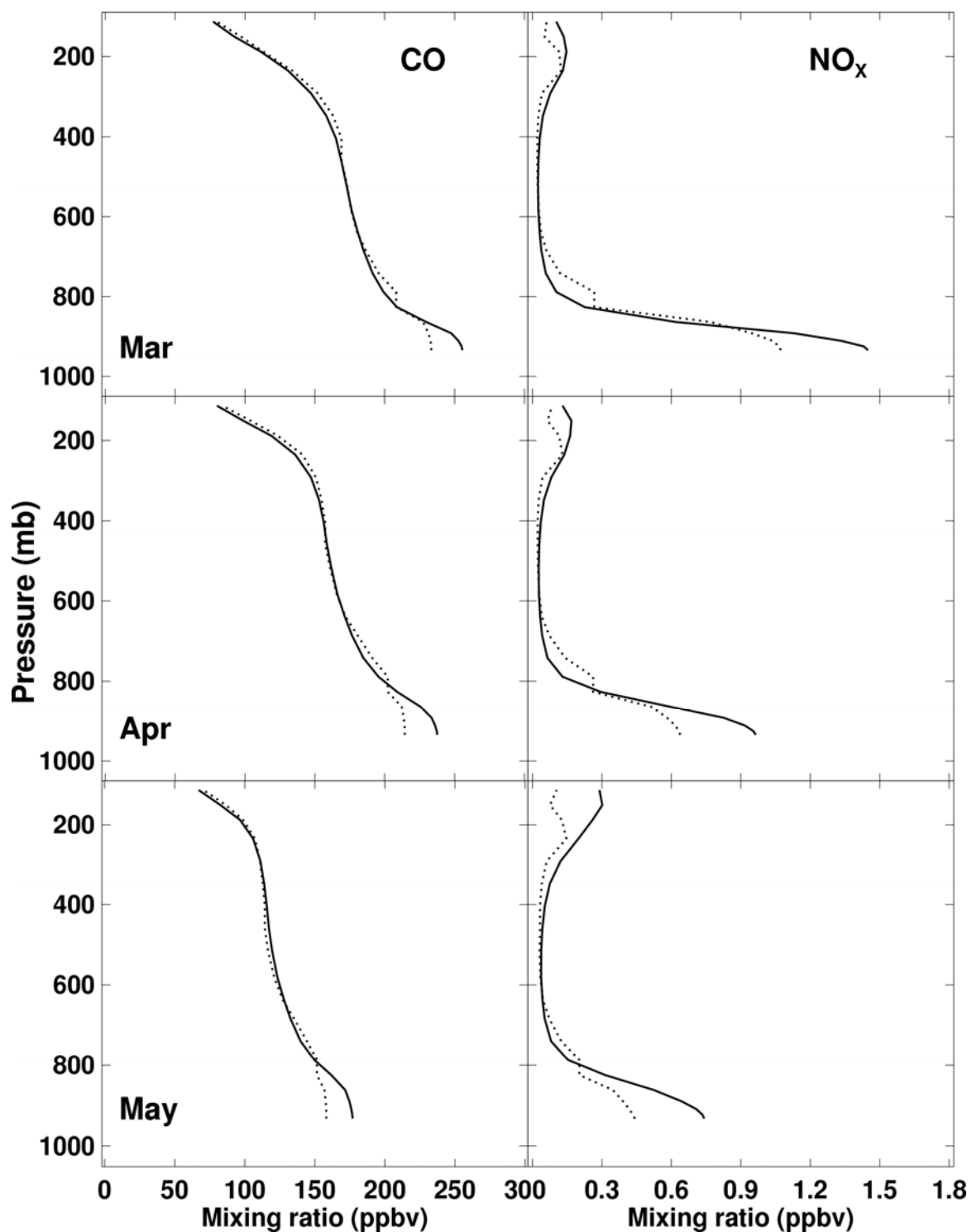


**Figure 3.11** The comparisons of averaged afternoon (1200-1600, LT) vertical profiles of CO and NO<sub>x</sub> concentrations from the REAM and GEOS-CHEM models. The solid lines represent the REAM simulations, and the dotted lines represent the GEOS-CHEM simulations.

of difference up to a factor of 2 is observed. The shallower mixing depth in REAM results in a stronger boundary layer vertical gradient and higher surface concentrations of CO and NO<sub>x</sub> than GEOS-CHEM (Figure 3.11). Surface CO and NO<sub>x</sub> over North America are larger by 15-20 ppbv and 200-300 pptv in the REAM results. In contrast, GEOS-CHEM CO and NO<sub>x</sub> are generally higher at the pressure altitudes of 600-800 hPa. During the spring, when the radical source largely driven by photon flux and water vapor [Y. Wang *et al.*, 2003] is limited, high concentrations of NO<sub>x</sub> decrease photochemical activity because of increasing radical loss through the reaction of OH and NO<sub>2</sub>. Thus, less active mixing in REAM predicts lower surface O<sub>3</sub> concentrations than in GEOS-CHEM, and the simulated O<sub>3</sub> concentration in REAM is in better agreement with the EPA surface measurements (Figure 3.9).

#### 3.4.3.4 MOZAIC O<sub>3</sub>

Most of the MOZAIC flights are in the upper troposphere. We first look at the measurements below 350 hPa. The data coverage is limited in these take-off and landing flights. Figure 3.12 shows a comparison of the MOZAIC data and the REAM results. Most of the data are for the eastern United States because the measurements are taken on commercial flights between the United States and Europe. Tropospheric O<sub>3</sub> mixing ratios are between 30 and 80 ppbv, showing a clear O<sub>3</sub> increase as the season shifts towards summer, which is consistent with the ozone climatology by Thouret *et al.* [2006]. REAM results reproduce reasonably well MOZAIC observations, except in the southern United States in March and May, when REAM overestimates O<sub>3</sub> (<10 ppbv) in the lower troposphere.



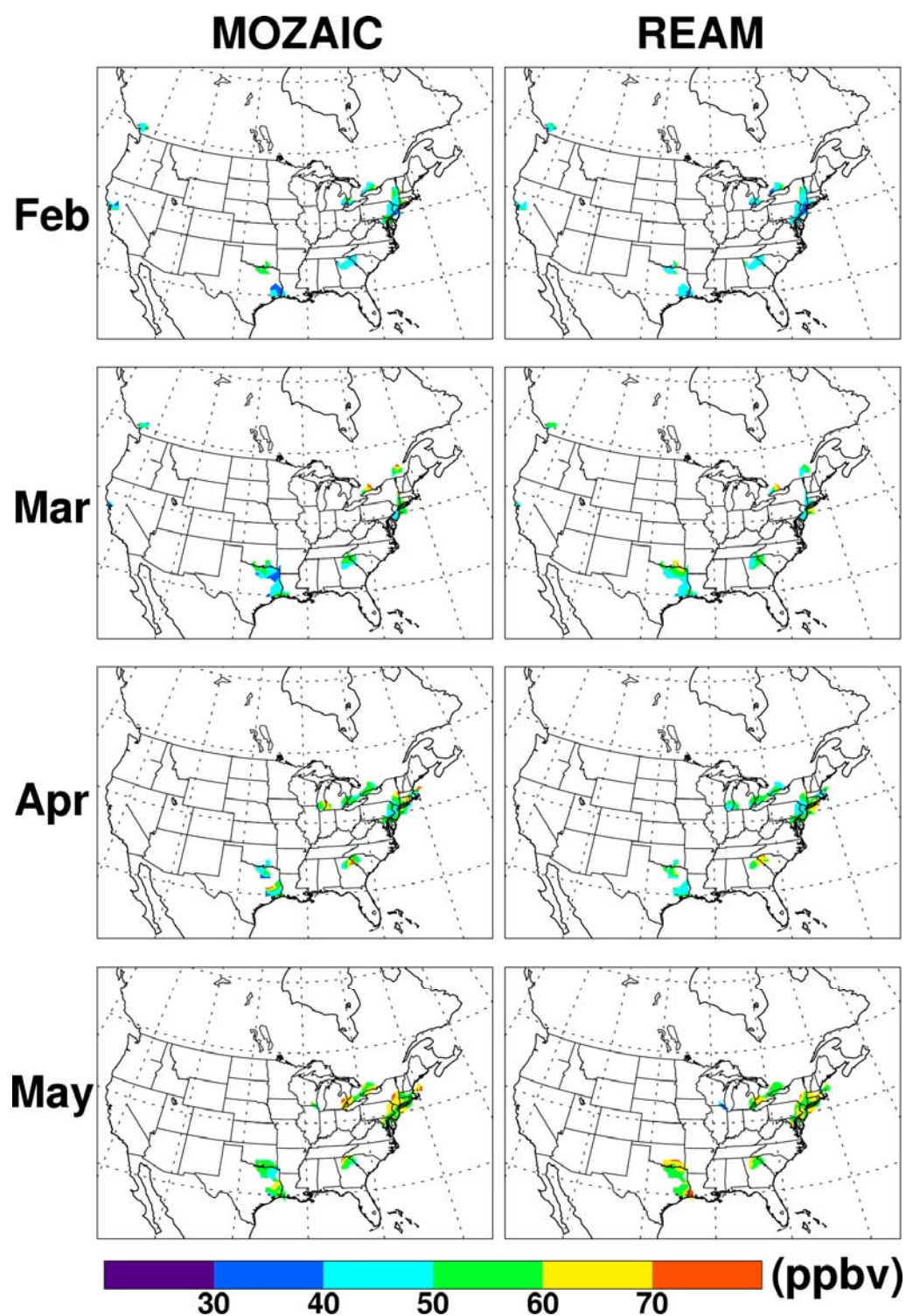


**Figure 3.12**  $O_3$  concentration (ppbv) below 350 hpa from the MOZAIC measurements during February-May 2000 (left column) and the corresponding REAM results (right column). The REAM data for comparison with the MOZAIC data are sampled along MOZAIC aircraft tracks.

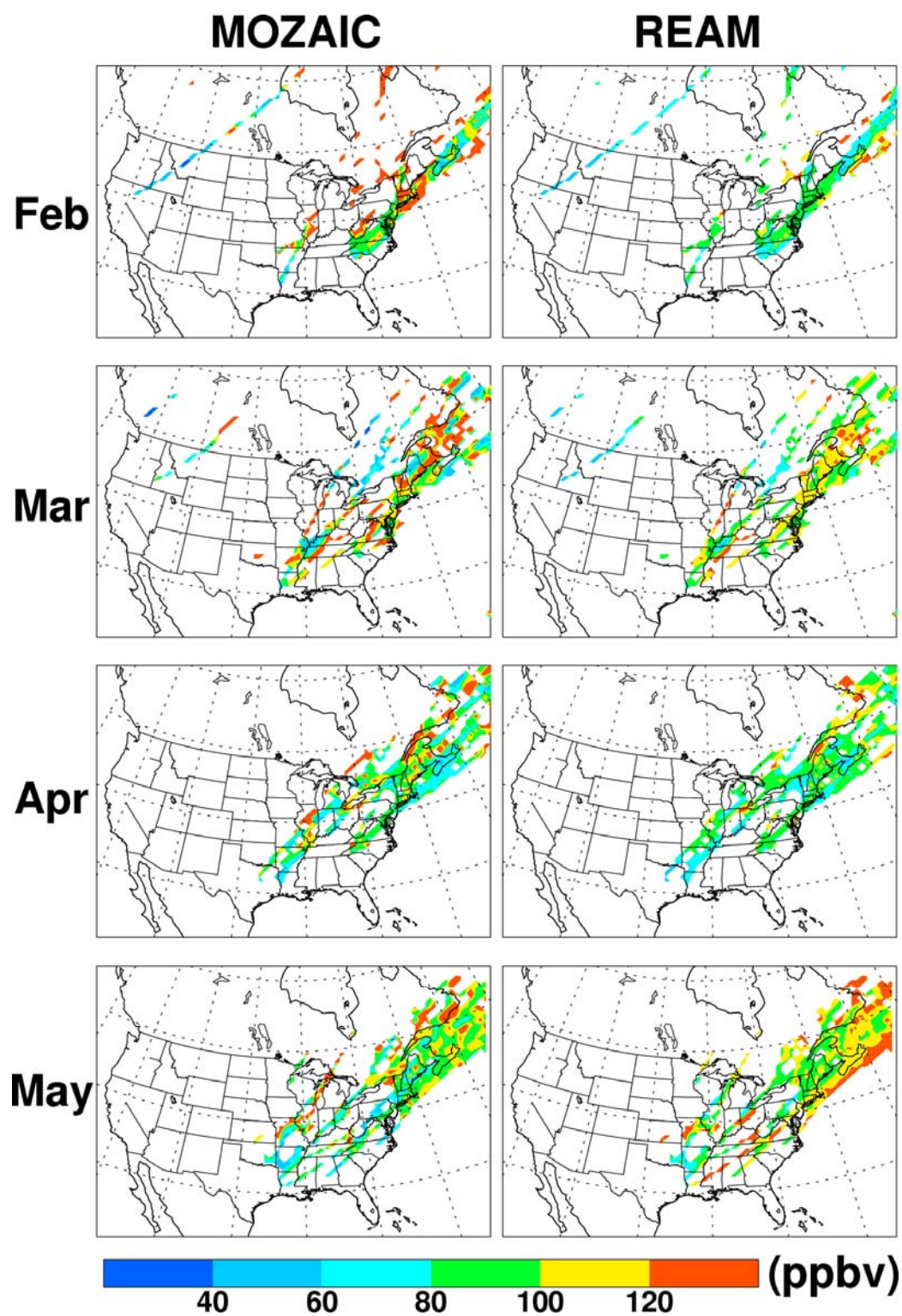


**Figure 3.13** The same as Figure 3.12, but for 250-350 hPa. The O<sub>3</sub> data > 200 ppbv from MOZAIC and REAM are filtered out.

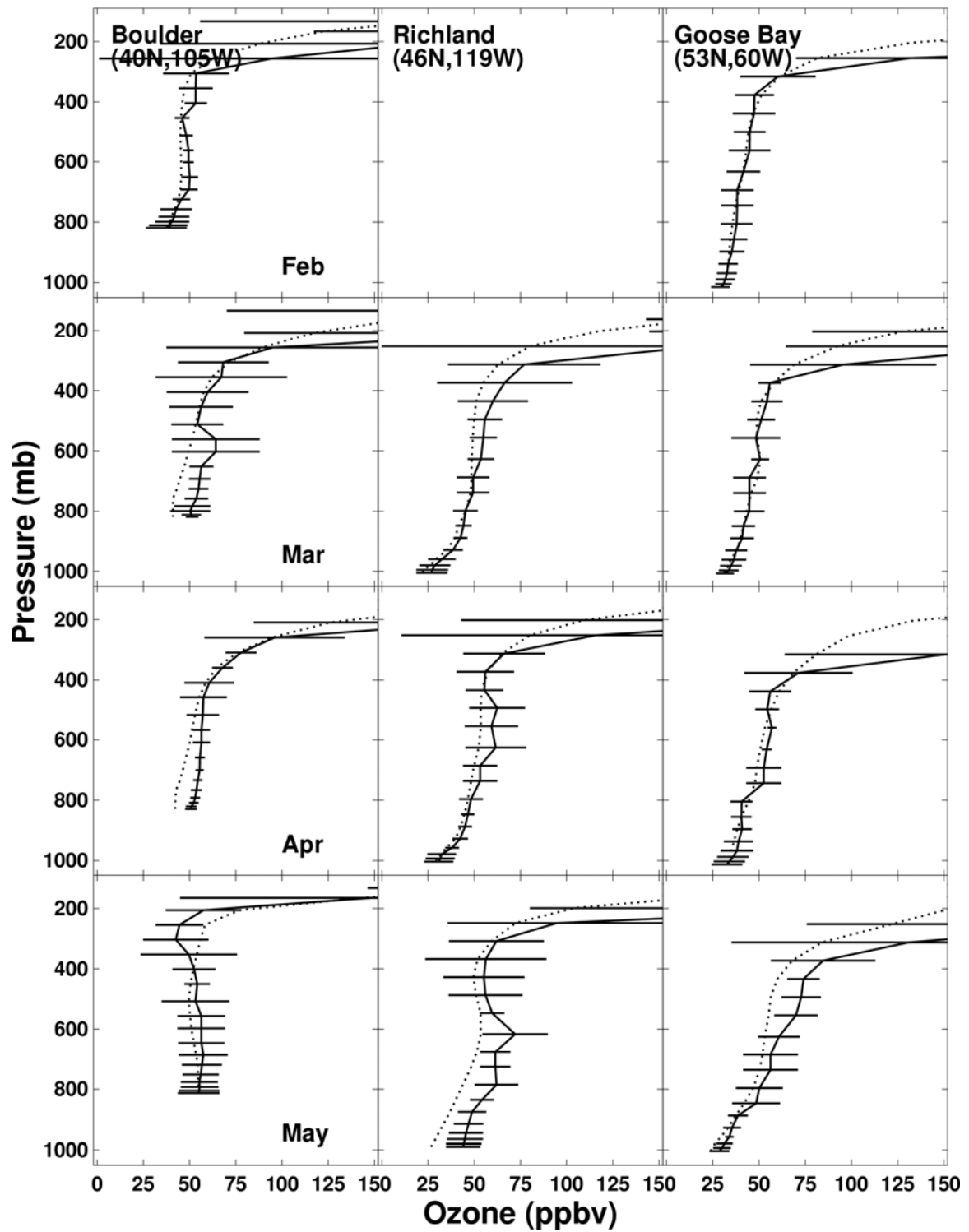


**Figure 3.14** Observed and simulated O<sub>3</sub> monthly mean vertical profiles (ppbv) for six ozonesonde sites at 30-55°N in February-May 2000. The solid lines represent the ozonesonde measurements, and the dotted lines represent the corresponding REAM results. The error bars represent the standard deviations of the measurements.



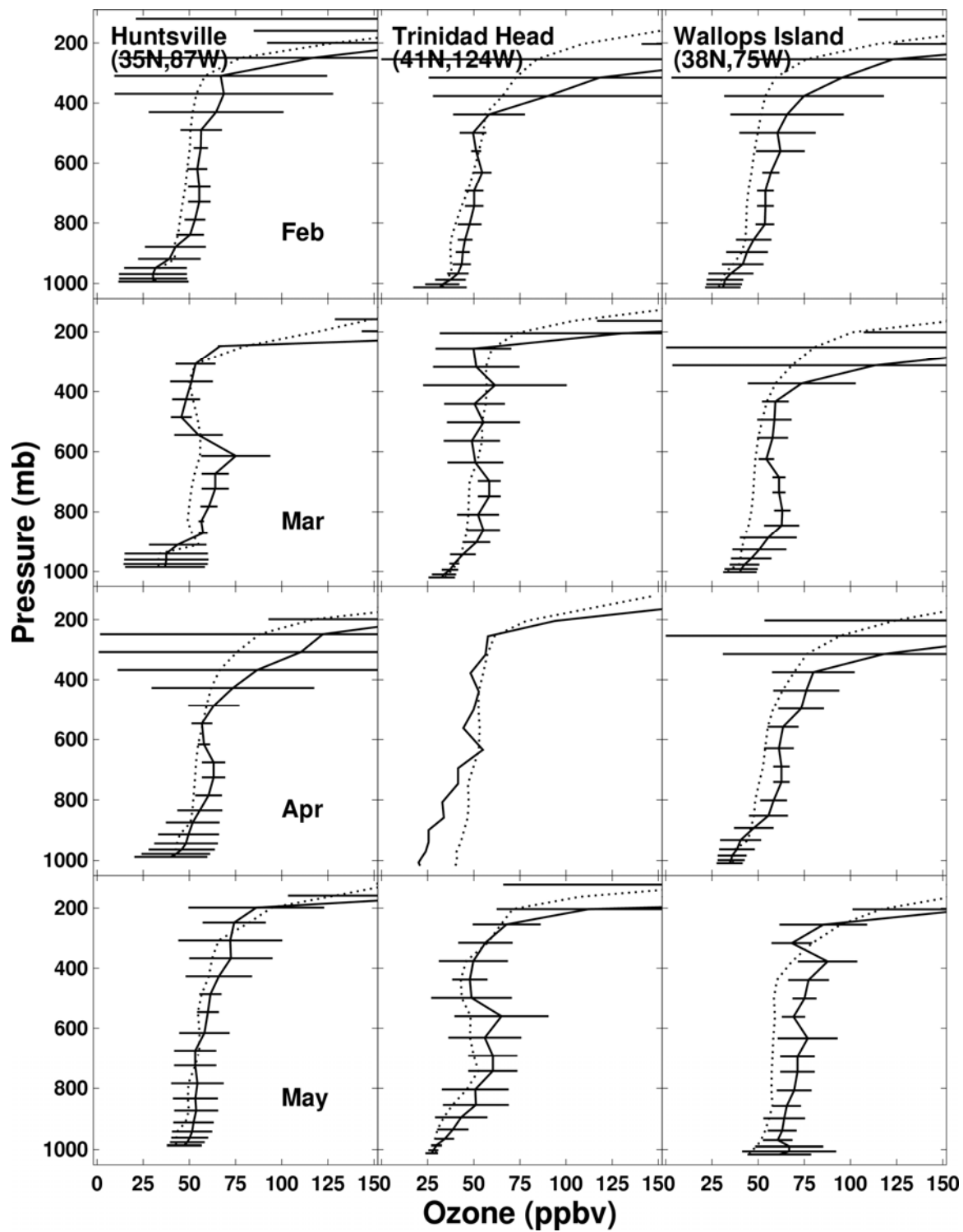


Figure 3.14 (continued.)

MOZAIC measurements in the upper troposphere show large influences from stratospheric air masses, which have high O<sub>3</sub> concentrations. We filtered out mixing ratios > 200 ppbv in the measurements (and model results) to minimize the effects of extreme values. Figure 3.13 shows a comparison of MOZAIC measurements with REAM results at 250-350 hPa. In general, REAM underestimates high O<sub>3</sub> concentration measurements, except in May. Thouret *et al.* [2006] found that maximum ozone in the MOZAIC measurements is found in the spring in the lower stratosphere, where ozone concentrations range from 150 to 500 ppb with a strong vertical gradient near the tropopause region. REAM underestimates O<sub>3</sub> concentrations compared with MOZAIC at that level. We will show the model bias in the comparison of the REAM results with the ozonesonde measurements (Figure 3.14). The upper tropospheric O<sub>3</sub> simulations in REAM are strongly affected by the specified upper boundary conditions at 100 hPa from GEOS-CHEM, which exhibits difficulties in simulating the sharp O<sub>3</sub> gradient across the tropopause [Bey *et al.*, 2001].

#### 3.4.3.5 Ozonesonde measurements

Ozonesonde observations at the six sites over North America are compared with the REAM results in Figure 3.14. The observed seasonal trend of increasing tropospheric O<sub>3</sub> concentration is captured reasonably well by REAM. However, the large concentration gradients near the tropopause in the ozonesonde observations are underestimated in the model. Stratospheric intrusion events are more frequent in the winter and the spring than in the summer. Therefore, the discrepancies between the REAM results and the MOZAIC and ozonesonde measurements decrease as the season

shifts towards summer. The monthly ozone concentrations and their changes below 350 hPa are better simulated than they are in the region above.

Simulated low-altitude O<sub>3</sub> concentrations are generally close to the ozonesondes measurements (within 10 ppbv). While the measurements at Boulder, Huntsville, and Wallops Island show O<sub>3</sub> increases in the lower troposphere, those at Trinidad Head and Goose Bay do not undergo large seasonal changes. The latter two stations are not as affected by North American NO<sub>x</sub> emissions as the other stations. The underestimation of REAM is the largest at Wallops Island, located at a baroclinic zone that has large ozone gradients, described previously by Thouret *et al.* [2006].

#### 3.4.3.6 TOMS-SAGE II tropospheric column O<sub>3</sub>

Section 3.2.4 describes tropospheric column O<sub>3</sub> derived from TOMS and SAGE II measurements. PV mapping is a promising method of deriving tropospheric O<sub>3</sub> at mid-latitudes. However, the resolution and accuracy of PV mappings largely depend on the relatively sparse number of ozonesonde observations [Bithell *et al.*, 1999], and ozonesonde observations are usually not coincident with SAGE measurements. Therefore, capturing events in synoptic or smaller scales is difficult using the PV mapping method. We use tropospheric O<sub>3</sub> products here to qualitatively examine the seasonal transition. Figure 3.15 compares TOMS-SAGE II tropospheric O<sub>3</sub> column with REAM and GEOS-CHEM results from February to May 2000. Both the satellite products and the models show a springtime increase in tropospheric O<sub>3</sub> over North America, even though absolute amounts of column O<sub>3</sub> from the PV mapping method do not agree well with either model. High O<sub>3</sub> columns are clearly shown over the western North Atlantic in the satellite

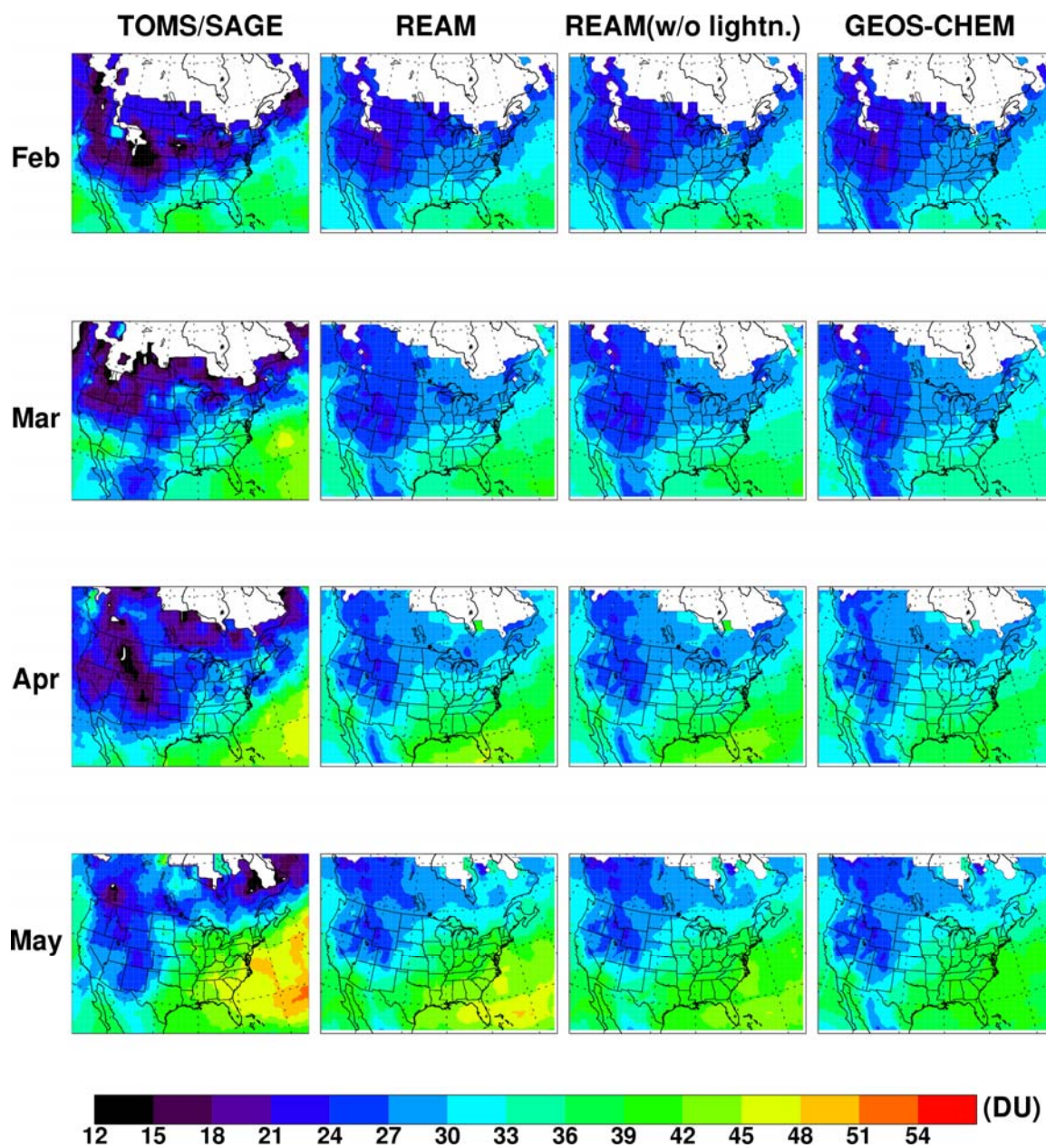


**Figure 3.15** Monthly mean tropospheric O<sub>3</sub> columns derived from TOMS total columns and SAGE II stratospheric columns (first column), the REAM standard simulation (second), the REAM sensitivity simulation without lightning NO<sub>x</sub> production (third), and the GEOS-CHEM simulation (last).

derived columns, particularly in May. The standard REAM model produces significant enhancements over the region while GEOS-CHEM does not. A sensitivity REAM simulation without lightning NO production exhibits much weaker enhancements, suggesting that lightning NO production is the main contributor to O<sub>3</sub> enhancements over the western North Atlantic. REAM-simulated lightning NO<sub>x</sub> enhancements (Figure 3.3) cover regions similar to TOMS-SAGE-derived O<sub>3</sub> enhancements. However, the resulting O<sub>3</sub> enhancements are mainly in the southern region, where solar influx is large.

### 3.4.4 Pollutant Export/Import Fluxes and Budget Calculations

#### 3.4.4.1 *Longitudinal pollutant fluxes*

Fluxes of NO<sub>x</sub>, NO<sub>y</sub>, CO, and O<sub>3</sub> imported to and exported from the troposphere in North America are estimated using the REAM results. Fluxes throughout the western and eastern boundaries are a factor of 18 larger than throughout the north and south boundaries. Here, we focus on longitudinal fluxes. Figure 3.16 shows the longitudinal import and export fluxes of these pollutants as a function of latitude. We find net import in the western boundary region and net export in the eastern boundary region. Import fluxes are generally smaller than export fluxes. The import and export fluxes of NO<sub>x</sub> are smaller than those of NO<sub>y</sub>, CO, and O<sub>3</sub> due to the relatively low concentrations of NO<sub>x</sub> caused by its shorter lifetimes. The latitudes of maximum NO<sub>x</sub> export are different from those of NO<sub>y</sub>, CO and O<sub>3</sub>. The shorter lifetimes of NO<sub>x</sub> dictate that the export flux reflects more the locations of NO<sub>x</sub> emissions, where longer-lived species are affected more by meteorology. The latitudes of NO<sub>x</sub>, NO<sub>y</sub>, CO, and O<sub>3</sub> export peaks in May are similar to those in June 1985 from PK04 [Park *et al.*, 2004b, hereafter referred to as

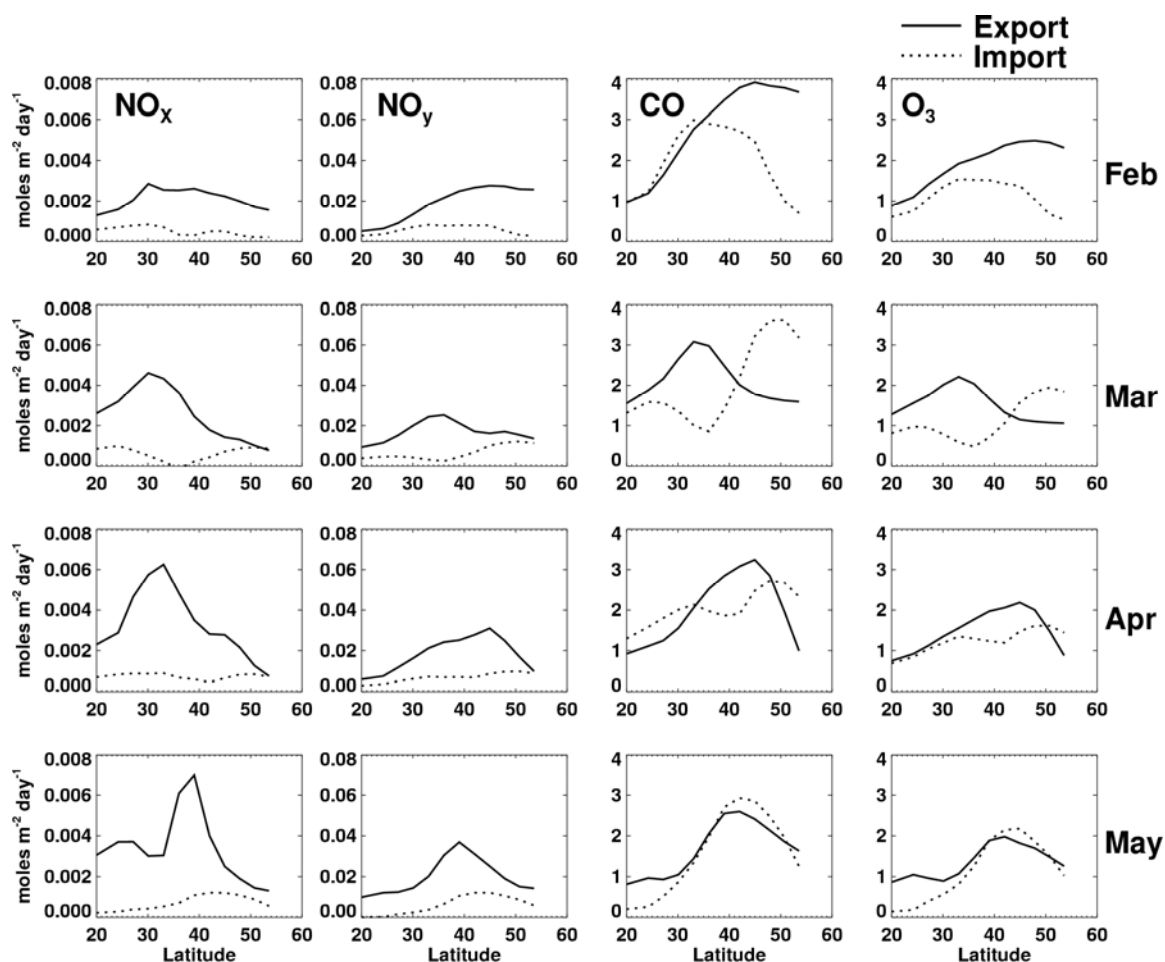


**Figure 3.16** The longitudinal import and export fluxes of  $\text{NO}_x$ ,  $\text{NO}_y$ , CO, and  $\text{O}_3$  over North America in the troposphere as a function of latitude. The western and eastern boundaries are the same as those depicted in Figure 3.15. The solid lines represent export fluxes while the dotted lines represent import fluxes.

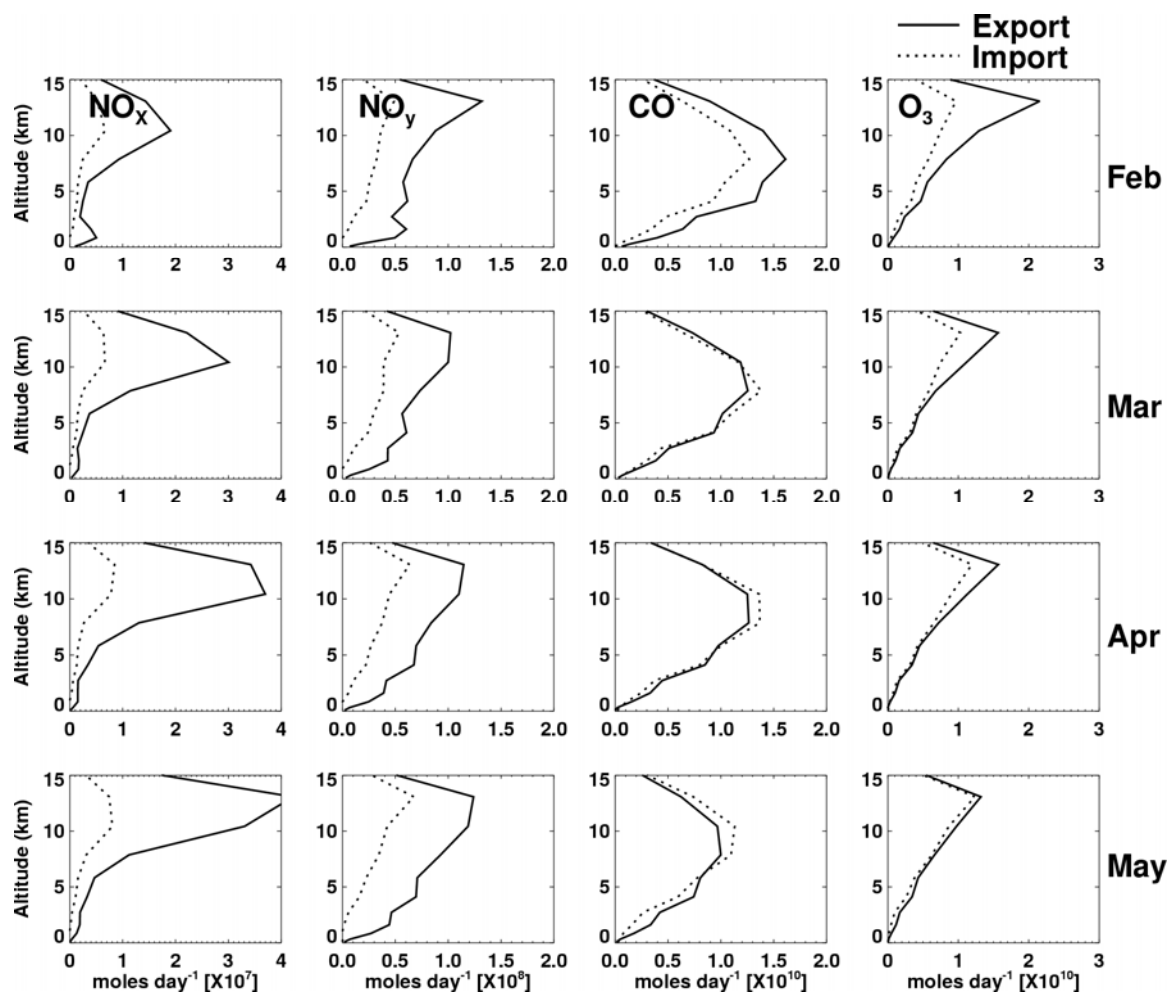


**Figure 3.17** The same as Figure 3.16, but for altitude.

PK04], but the  $\text{NO}_x$  export in May in this study is higher by a factor of 3 than that by PK04, reflecting higher lightning  $\text{NO}_x$  production. The peak  $\text{NO}_y$  export in this study is also higher than PK04 by 25%. The net export of  $\text{NO}_x$  increases from February to May because of increasing emissions from lightning and soils (Figure 3.3). The net exports of  $\text{CO}$  and  $\text{O}_3$  at 20-40 °N are most significant in May, driven in part by more activate convection in the region.

Figure 3.17 shows longitudinal import and export fluxes as a function of altitude. REAM shows that significant pollution import from the West takes place in the upper troposphere, and that export fluxes of  $\text{NO}_x$  and  $\text{NO}_y$  are much larger than import fluxes at high altitudes. This trend is also shown in PK04. The peak  $\text{NO}_x$  export in May in this study is larger than that from PK04 by a factor of 5. The peak export of  $\text{NO}_y$  in this study is larger than that of PK04 by 38%. Import fluxes of  $\text{NO}_x$  and  $\text{NO}_y$  in this study are similar to those from PK04. In addition, in PK04, less  $\text{CO}$  was exported than imported above 7 km in March-May due to a stronger jet stream over the Pacific than over the Atlantic, which is also shown in this study. PK04 shows that less  $\text{O}_3$  is exported than imported above 9 km. By comparison, we find that  $\text{O}_3$  export fluxes are similar to the import fluxes in the upper troposphere in this study, likely due to higher lightning  $\text{NO}_x$  production.

Export of  $\text{NO}_x$  in the upper troposphere is enhanced due to lightning production [Pickering *et al.*, 1998; Choi *et al.*, 2005]. Simulated  $\text{NO}_x$  export fluxes at 12 km increase from  $1.8 \times 10^7$  moles  $\text{day}^{-1}$  to  $4 \times 10^7$  moles  $\text{day}^{-1}$  from February to May. This increase is associated with active lightning  $\text{NO}_x$  production as the season shifts towards summer. Sensitivity studies (not shown) indicate that lightning production enhances  $\text{NO}_x$



and NO<sub>y</sub> exports in the upper troposphere (8-12 km) by 252% and 66%, respectively, in May.

Maximum NO<sub>x</sub> fluxes occur at about 10 km in February, March, and April, and at about 12 km in May due to lightning NO<sub>x</sub> enhancements at high altitudes. The maximum O<sub>3</sub> and NO<sub>y</sub> fluxes are located at about 10-15 km. Maximum CO fluxes occur at about 9 km. Maximum CO fluxes take place at a lower altitude because the source of CO emissions is primarily at the surface. By comparison, the sources of NO<sub>x</sub> (and hence, NO<sub>y</sub>) are aircraft and lightning in the upper troposphere, and O<sub>3</sub> has net production in the upper troposphere [e.g., Y. Wang *et al.*, 2003].

#### *3.4.4.2 Net fluxes in the free troposphere and boundary layer*

##### *3.4.4.2.1 Net flux in the lower and middle troposphere*

We chose 7 km as the top of the middle troposphere in order to compare our results with those of PK04. Net fluxes of NO<sub>x</sub> in the lower and middle troposphere (<7 km) are 0.037, 0.014, 0.023, and 0.024 Gmol day<sup>-1</sup>, and those of NO<sub>y</sub> are 0.47, 0.32, 0.36, and 0.43 Gmol day<sup>-1</sup> from February to May 2000 (Table 3.2a). NO<sub>x</sub> and NO<sub>y</sub> net fluxes decrease from February to March, but beginning in April, the net fluxes increase due to enhanced lightning and soil NO<sub>x</sub> emissions. Compared with the net fluxes of NO<sub>x</sub> and NO<sub>y</sub> in June from PK04, NO<sub>x</sub> and NO<sub>y</sub> the net fluxes in May in this study are larger by 50% and 79%, respectively.

Export CO fluxes from North America in the lower and middle troposphere are 93, 61, 53, and 49 Gmol day<sup>-1</sup> from February to May, compared with imports of 61, 61, 52, 39 Gmol day<sup>-1</sup> (Table 3.2a). The import and export fluxes in May in this study are larger

than those from PK04. However, the net CO flux over North America in May is 10 Gmol day<sup>-1</sup>, which is similar to the 12 Gmol day<sup>-1</sup> in June from PK04. Net flux is largest in the winter due to slow photochemical loss, but net flux in May is larger than in March and April in part due to the increase of photochemical CO production. The difference in import CO fluxes between PK04 (20 Gmol day<sup>-1</sup>) and those in this study (39 Gmol day<sup>-1</sup> in May) could stem from a number of factors, including an underestimation of Asian fossil fuel emissions and an overestimation of OH concentrations in the spring and the summer in PK04 [Park *et al.*, 2004a]. Other contributors could be the month and interannual differences.

The net O<sub>3</sub> flux in the lower and middle troposphere in May in this study (6 Gmol day<sup>-1</sup>) is smaller than that in PK04 (10 Gmol day<sup>-1</sup> in June). Photochemistry is more active in June than it is in May. PK04 used meteorological fields from GEOS-3 Stretched Grid Data Assimilation System (SG-DAS) [Fox-Rabinovitz *et al.*, 2002], which may also

**Table 3.2a** The import and export fluxes of tracers in the lower and middle troposphere (<7 km) over North America (20 – 62°N, Gmol day<sup>-1</sup>)

	Import fluxes				Export fluxes			
	Feb	Mar	Apr	May	Feb	Mar	Apr	May
NO <sub>x</sub>	0.003	0.006	0.007	0.006	0.04	0.02	0.03	0.03
NO <sub>y</sub>	0.11	0.14	0.13	0.09	0.58	0.46	0.49	0.52
CO	61	61	52	39	93	61	53	49
O <sub>3</sub>	21	21	20	16	30	22	21	22

**Table 3.2b** Same as table 3.2a, but in the boundary layer (<2.5 km)

	Import fluxes				Export fluxes			
	Feb	Mar	Apr	May	Feb	Mar	Apr	May
NO <sub>x</sub>	0.00	0.00	0.00	0.00	0.02	0.01	0.01	0.01
NO <sub>y</sub>	0.01	0.02	0.02	0.007	0.31	0.20	0.19	0.21
CO	18	17	13	9	33	19	14	16
O <sub>3</sub>	5.2	4.5	3.8	2.5	8.2	5.2	4.2	5.3

have deeper mixing depths than MM5 simulations in REAM, resulting in higher O<sub>3</sub> concentrations near the surface, as in the case of GEOS-CHEM (see Figure 3.9).

#### *3.4.4.2.2 Net flux in the boundary layer*

We chose 2.5 km as the top of the boundary layer in order to compare our results with those of PK04. NO<sub>x</sub> exports in the boundary layer are 0.02, 0.01, 0.01, and 0.01 Gmol day<sup>-1</sup>, and NO<sub>y</sub> exports 0.31, 0.20, 0.19, and 0.21 Gmol day<sup>-1</sup> from February to May, respectively (Table 3.2b). PK04 shows NO<sub>x</sub> and NO<sub>y</sub> exports of 0.01 and 0.11 Gmol day<sup>-1</sup>, respectively, in the boundary layer in the month. Whereas the net flux difference in NO<sub>x</sub> in the troposphere (<12 km) of the two studies is large, the net fluxes of NO<sub>x</sub> in the boundary are the same (Table 3.2b) because the impact of lightning NO<sub>x</sub> is primarily in the upper troposphere. Some of the lightning NO<sub>x</sub> in the free troposphere is transported to the boundary layer. During transport, NO<sub>x</sub> is oxidized into longer-lived NO<sub>y</sub> species such as HNO<sub>3</sub>. As a result, the NO<sub>y</sub> export is larger.

Export CO fluxes in the boundary layer are 33, 19, 14, and 16 Gmol day<sup>-1</sup> and import CO fluxes 18, 17, 13, and 9 Gmol day<sup>-1</sup> from February to May, respectively. Net CO fluxes over North America are 15, 2, 1, and 7 Gmol day<sup>-1</sup> for the February to May period. The net CO flux in May is comparable to that of 7.2 Gmol day<sup>-1</sup> in June from PK04.

Exports of O<sub>3</sub> in the boundary layer are 8.2, 5.2, 4.2, and 5.3 Gmol day<sup>-1</sup> and imports 5.2, 4.5, 3.8, and 2.5 Gmol day<sup>-1</sup> from February to May. Net exports are 3.0, 0.7, 0.4 and 2.8 Gmol day<sup>-1</sup> from February to May. The net flux in May is smaller than the

4.88 Gmol day<sup>-1</sup> in June from PK04 for the same reasons discussed for the lower and middle tropospheric flux comparison.

#### *3.4.4.2.3 Export efficiencies for NO<sub>x</sub>*

North American NO<sub>x</sub> emissions (20-62°N) are about 1.47 Gmol day<sup>-1</sup>. About 1.4%, 0.7%, 0.6%, and 0.7% of the emission are exported as NO<sub>x</sub>, and 20%, 12%, 12%, and 14% are exported as NO<sub>y</sub> from the boundary layer from February to May, respectively. Because of more active convection (and lightning production) towards May, the export efficiency of NO<sub>x</sub> increases while that of photo-oxidation decreases. The ratio of NO<sub>x</sub> fluxes in the boundary layer to total emissions in May is comparable to that of PK04 (0.6%), but the ratio for NO<sub>y</sub> is twice as large as that of PK04 (7%), suggesting a large difference between the two models with regard to reactive nitrogen speciation. Considering the region below 7 km, 2.5%, 1.0%, 1.6%, and 1.6% are exported as NO<sub>x</sub> and 32%, 22%, 24%, and 29% as NO<sub>y</sub> from February to May, respectively. PK04 showed that 1% and 15% of NO<sub>x</sub> emissions were exported as NO<sub>x</sub> and NO<sub>y</sub>, respectively. The export efficiencies of NO<sub>x</sub> and NO<sub>y</sub> fluxes from the lower and middle troposphere in this study are 60% and 100% larger than those of PK04, respectively.

### **3.5 Conclusions**

We apply a regional chemical transport model (REAM) to analyze surface, ozonesonde, aircraft, and satellite measurements over North America from February to May 2000, in order to investigate the transitions of the concentrations and fluxes of O<sub>3</sub> and its precursors during the rapid photochemical and dynamical changes that occur in

the spring. The GEOS-CHEM model is used to provide not only chemical initial and boundary conditions but also targeted comparisons with REAM results. Pollutant fluxes from this work are compared with earlier work by PK04. Surface observations from the EPA AIRNow and SEARCH networks, aircraft observations from the TOPSE and MOZAIC experiments, ozonesondes, and satellite measurements from GOME, MOPITT, TOMS, and SAGE II are analyzed.

The REAM results are generally in good agreement with observations in the troposphere. Comparisons of surface measurements from EPA AIRNow ( $O_3$ ) and SEARCH networks ( $O_3$ , CO, and  $NO_x$ ) show that REAM performs reasonably well in simulating multi-day variations and seasonal transitions. The model is in reasonable agreement with MOZAIC and ozonesonde  $O_3$  measurements in terms of seasonal transitions, but simulated  $O_3$  concentrations above 350 hPa are biased low because the specified upper boundary condition for  $O_3$  is also biased low. The low bias decreases towards May as tropospheric chemistry becomes more important. Qualitative agreement between the model results and TOMS-SAGE II-derived tropospheric  $O_3$  column are found. Lightning  $NO_x$  production is found to contribute large  $O_3$  enhancements over the western North Atlantic in May.

MOPITT CO measurements are found to be in good agreement with column concentrations derived from TOPSE in situ measurements and REAM-simulated vertical CO profiles. However, after AK processing, the vertical information in the in situ measurements is clearly lost. The two model results are in good agreement with MOPITT CO columns with high correlation coefficients ( $R > 0.89$ ) and small mean biases

(< ±2.45%). The mixing depth in REAM is lower than in GEOS-CHEM, contributing to slightly lower a REAM mean CO column.

Comparisons of GOME NO<sub>2</sub> columns with REAM and GEOS-CHEM show that the model captures GOME spatial variation well in the spring (R> 0.85) with small mean biases (<±11%). While active photochemical oxidation leads to lower NO<sub>2</sub> columns from February to May, NO<sub>x</sub> emissions from lightning and soils also increase. The resulting monthly mean enhancements are  $0.5-2 \times 10^{15}$  and  $0.5-1.0 \times 10^{15}$  molecules cm<sup>-2</sup>, respectively. Some NO<sub>x</sub> enhancements in May due to lightning and soil emissions are larger than GOME retrieval uncertainties, suggesting that satellite measurements may be used to constrain the emissions.

A major difference found between REAM and GEOS-CHEM simulations is that the increase in surface O<sub>3</sub> concentrations from February to May over the eastern United States in GEOS-CHEM is larger than it is in the REAM or EPA surface observations. A key factor driving the model difference is mixing depth, which is much lower in REAM (simulated by MM5) than it is in GEOS-CHEM (simulated by GEOS-3). With limited supplies of radicals in the springtime, a larger mixing depth in GEOS-CHEM results in faster photochemical activation because radical loss by the reaction of OH and NO<sub>2</sub> decreases.

Another difference between REAM and GEOS-CHEM is that lightning NO<sub>x</sub> production is larger in REAM, particularly over the western North Atlantic, where REAM results are in better agreement with GOME NO<sub>2</sub> measurements. Because the mixing depth is shallower and lightning NO<sub>x</sub> production is larger, REAM simulates larger NO<sub>x</sub> vertical gradients in the lower and upper troposphere than GEOS-CHEM.

Higher surface concentrations and a larger boundary layer gradient in REAM leads to smaller AMFs in GOME NO<sub>2</sub> retrievals, which leads to higher top-down estimates of fossil fuel NO<sub>x</sub> emissions (3-16%) than GEOS-CHEM from February to April. In May, however, higher lightning NO<sub>x</sub> emissions in REAM leads to a smaller top-down estimate (20%) than those in GEOS-CHEM. Over the course of the season, the top-down estimates from the two models are essentially the same and in close agreement with those from the EPA NEI inventory.

Lightning NO<sub>x</sub> production is a major contributor to the seasonal increase in the exports of NO<sub>x</sub> and NO<sub>y</sub> from North America in the upper troposphere. As a result, simulated NO<sub>x</sub> export fluxes at 12 km increase by more than a factor of 2 from February to May ( $1.8$  to  $4 \times 10^7$  moles day<sup>-1</sup>). In May, lightning production enhances NO<sub>x</sub> and NO<sub>y</sub> exports in the upper troposphere (8-12 km) by 252% and 66%, respectively. The effects of lightning on the net fluxes of NO<sub>x</sub> and NO<sub>y</sub> in the lower and middle troposphere are smaller. The model estimates 0.6-0.7 and 12-14% of NO<sub>x</sub> and NO<sub>y</sub>, respectively, are exported from the boundary layer from March to May.

## CHAPTER IV

### EVIDENCE OF SPRING-SUMMER NORTHWARD MIGRATION OF HIGH O<sub>3</sub> OVER THE WESTERN NORTH ATLANTIC

#### 4.1 Introduction

A major pathway for North American pollution outflow is cloud convection along with the warm conveyor belt (WCB) during the spring and summer [Li *et al.*, 2005; Kiley *et al.*, 2006]. Cloud convection, which is associated with lightning, enhances the precursor of ozone in the upper troposphere (UT) during the spring and summer. Due to convection, the enhanced precursors in the upper troposphere (UT) [Bertram *et al.*, 2007] are largely exported to the North Atlantic due to stronger westerly winds [Park *et al.*, 2004; Choi *et al.*, 2005, 2007a]. The chemical consequences of the addition of NO<sub>x</sub> in the UT due to aircraft or lightning NO<sub>x</sub> production on HO<sub>x</sub> and O<sub>3</sub> chemistry over the western North Atlantic have been studied from previous aircraft campaigns such as the <sup>3</sup>SASS (Subsonic Assessment) Ozone and NO<sub>x</sub> Experiment (SONEX), the NOAA Intercontinental Transport and Chemical Transformation (ITCT 2004), and the NASA Intercontinental Transport Experiment-North America, Phase A (INTEX-A) [Brune *et al.*, 1999; Jaegle *et al.*, 1999; Liu *et al.*, 1999; Singh *et al.*, 1999; Crawford, J., 2000; Bertram *et al.*, 2007; Hudman *et al.*, 2007]. Jaegle *et al.* [1998, 1999] also showed that NO<sub>x</sub> concentration to transfer North America from NO<sub>x</sub>-limited to NO<sub>x</sub>-saturated regimes in the spring is higher than that in the fall. Choi *et al.* [2005] also demonstrated that the transient enhancements of lightning NO<sub>x</sub> and the convective transport of CO have large enough signals for satellites to detect. Their impact on pollutant distributions averaged over a long time period become more difficult over land, but the signals are easier to

---

<sup>3</sup>This Chapter is for “Evidence of spring-summer northward migration of high O<sub>3</sub> over the western North Atlantic,” prepared for the submission to *Geophysical Research Letter* in 2007. Authors are Y. Choi, *et al.*



detect over the ocean [e.g., Li *et al.*, 2005; Choi *et al.*, 2005, 2007a]. In this work, we examine pollutant enhancements and their chemical consequences over the western North Atlantic during the transition from spring to summer in 2005 using measurements from recent satellite instruments, OMI, MLS, and TES, onboard the NASA Aura satellite. The Regional chEmical and trAnsport Model (REAM) [Choi *et al.*, 2005, 2007a] is applied to analyze the satellite measurements.

Many investigators have reported better agreement between the satellite measurements and the model results in tropical regions than at mid- and high-latitudes [e.g., Chandra *et al.*, 2003, 2004; Edwards *et al.*, 2003; Martin *et al.*, 2006a, 2006b; Ziemke *et al.*, 2006]. Recent GEOS-CHEM studies show increased lightning NO<sub>x</sub> production at higher latitudes from the standard model [e.g., Martin *et al.*, 2006b; Hudman *et al.*, 2007]. In the REAM model, lightning NO<sub>x</sub> production shows reasonably good agreement with measurements [Choi *et al.*, 2005]. Convective transport of CO is in agreement with MOPITT measurements [Choi *et al.*, 2005]. Simulated transient tropospheric O<sub>3</sub> column changes are in general agreement with OMI-MLS derived tropospheric O<sub>3</sub> column observations [Jing *et al.*, 2006]. More detailed REAM evaluations with surface, ozonesonde, aircraft, and satellite measurements are presented by Choi *et al.* [2007a]. In this work, we conduct sensitivity analyses to investigate the effects of surface pollutant emissions and lightning NO production on the spring-summer migration of high O<sub>3</sub> over the western North Atlantic.

#### **4.2 Satellite Measurements: OMI-MLS Tropospheric Column O<sub>3</sub>, OMI Tropospheric Column NO<sub>2</sub>, and TES O<sub>3</sub> and CO**

OMI, MLS, and TES are onboard the NASA Aura satellite, which passes over the equator at 1345 PM local time. The horizontal resolutions of OMI, MLS and TES are  $13\text{ km}\times 24\text{ km}$ ,  $30\text{ km}\times 150\text{ km}\times 2.5\text{ km}$ , and  $5\text{ km}\times 8\text{ km}$ . The tropospheric  $\text{O}_3$  column is derived using a residual method. We use a combination of MLS profiles above 215 hPa and OMI level 2 total column  $\text{O}_3$ . The OMI and MLS coincidence criteria are  $\pm 1.25^\circ$  longitude by  $1.25^\circ$  latitude on the same day. The mid-latitude stratospheric  $\text{O}_3$  columns between 215 hPa and the tropopause are obtained by SAGE II mapping profiles [Yang *et al.*, 2007]. The tropospheric  $\text{O}_3$  column is then obtained by subtracting stratospheric  $\text{O}_3$  columns from the OMI total columns. To avoid the interference of clouds on satellite measurements, we use only the OMI total column obtained under clear sky conditions defined as the reflectivity of  $< 10\%$  based on OMI 360 nm reflectivity data. A detailed validation of the OMI-MLS tropospheric  $\text{O}_3$  products was performed by Yang *et al.* [2007].

The retrieval of tropospheric  $\text{NO}_2$  columns from OMI measurements [Bucsela *et al.*, 2006] and their uncertainty are obtained from the NASA Goddard Earth Sciences Distributed Active Archive Center (GES DAAC). We use only OMI tropospheric  $\text{NO}_2$  column data with a cloud fraction of  $< 40\%$ . TES  $\text{O}_3$ , and CO data are obtained from the NASA Langley Atmospheric Science Data Center (ASDC). Only TES  $\text{O}_3$  and CO retrieval data with a degree of freedom (DFS) of  $> 3.5$  and  $1.0$ , respectively, are used. When compared with the results of the observations, the REAM results are processed with TES retrieval averaging kernels for  $\text{O}_3$  and CO, described by Worden *et al.* [2007] and Luo *et al.* [2007], respectively. TES  $\text{O}_3$  and CO are interpolated onto  $3^\circ$  latitude by  $4^\circ$  longitude using measurement locations.

### 4.3 Model Description

The model set up in this study is the same as that set up by Choi *et al.* [2005, 2007a]. REAM has a horizontal resolution of 70 km, with 23 vertical layers reaching 10 hPa. The National Center for Atmospheric Research/Penn State MM5 is used to simulate meteorological fields using four-dimensional data assimilation (FDDA) [Stauffer *et al.*, 1991] with the National Center for Environmental Prediction reanalysis, surface, and rawinsonde observations. Most meteorological variables are archived every 30 minutes. For convection and lightning, they are archived every 2.5 minutes. Spring and summer 2005 GEOS-CHEM model simulations provide initial and boundary conditions for trace gases. Regional simulations were spun up during the last two weeks of March 2005. Emission inventories for combustion and industrial sources are taken from GEOS-CHEM [Bey *et al.*, 2001], except for the fossil fuel NO<sub>x</sub> and CO emissions over the United States, which are taken from the 1999 US Environmental Agency National Emission Inventory. Our previous lightning NO<sub>x</sub> production in REAM using convective available potential energy and cloud mass flux resulted in evidence of the lightning-caused NO<sub>x</sub> signals over North America seen in GOME during spring [Choi *et al.*, 2005, 2007a]. The model produces  $3.0 \times 10^{26}$  NO molecules per flash of intracloud and cloud-to-ground flashes.

### 4.4 Results and Discussion

#### 4.4.1 OMI-MLS Tropospheric O<sub>3</sub>

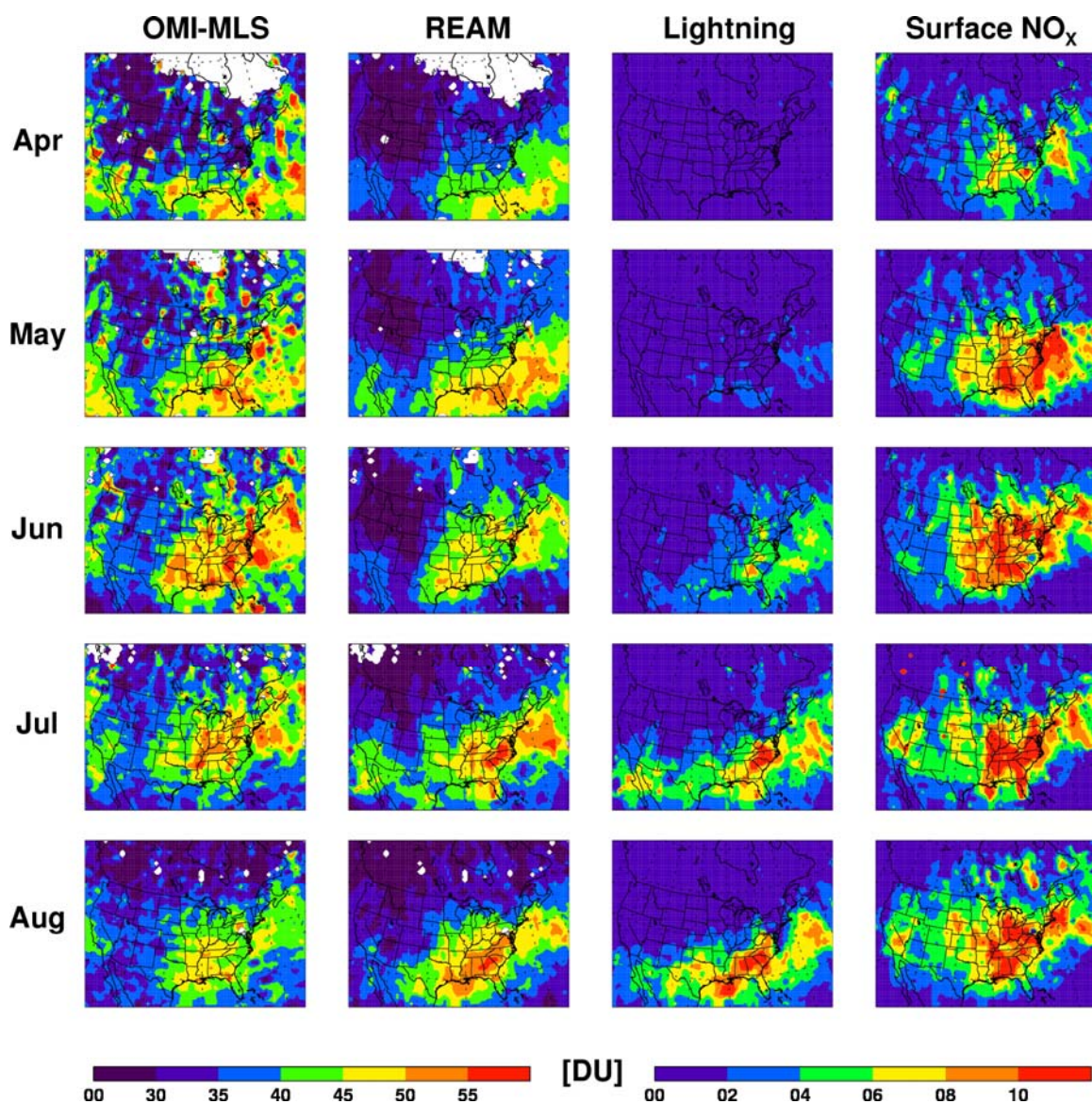


**Figure 4.1** Monthly mean tropospheric O<sub>3</sub> columns from April to August 2005 derived from OMI-MLS satellite measurements (first column), REAM simulations (second column), O<sub>3</sub> produced due to lightning NO production (third column), and O<sub>3</sub> produced due to surface emissions (last column).

Figure 4.1 shows the monthly mean tropospheric column  $O_3$  derived from OMI-MLS satellite measurements and the corresponding model simulations from April to August 2005. The model-simulated  $O_3$  concentrations are added to the level that located on the tropopause level from NCEP reanalysis data. OMI-MLS column shows high  $O_3$  over the eastern United States and the western North Atlantic. Despite large surface emissions of  $O_3$  precursors over North America,  $O_3$  enhancements over the western North Atlantic are as high as they are over the eastern United States. In fact, in April and May,  $O_3$  enhancements ( $> 45$  DU) over the ocean regions are higher than they are over land. As the season progresses from spring to summer, the high  $O_3$  regions over the western North Atlantic move northward from the coast off Florida to New England. In comparison, over the eastern United States, little  $O_3$  enhancement occurs in April. The  $O_3$  enhancement first reaches the southeastern United States in May, and by June, it covers the entire eastern United States. Photochemistry and  $O_3$  production slow in April, so the  $O_3$  enhancements are further downwind from the source regions than they are during the summer months.

Compared with the OMI-MLS measurements, REAM-simulated tropospheric  $O_3$  columns tend to be lower in June but higher in August. Overall, the model reproduces the aforementioned features in the OMI-MLS measurements. The measurements indicate that some of the enhancements over Canada and its coast in April and May are probably related to ozone from the stratosphere, but they are not captured by the model. A detailed comparison with MOZAIC aircraft  $O_3$  measurements and ozonesondes by Choi *et al.* shows that REAM exhibits a tendency of underpredicting upper tropospheric ozone ( $<$

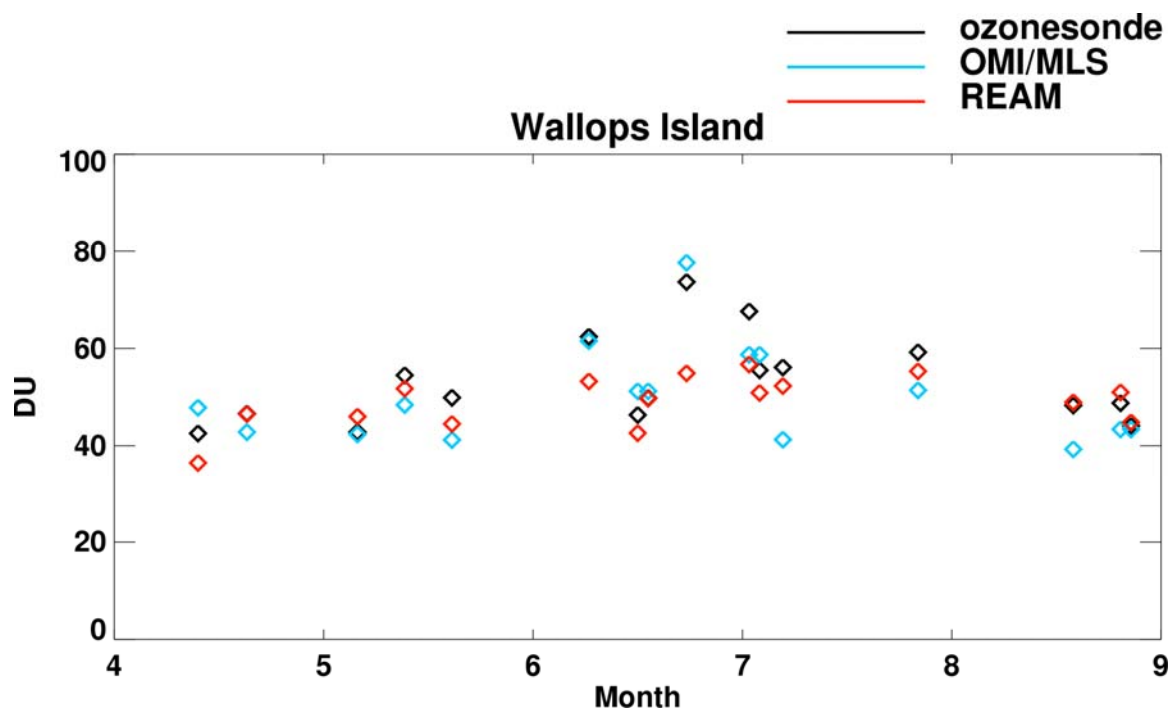


**Figure 4.2** Tropospheric O<sub>3</sub> columns measured by ozonesondes, derived from OMI-MLS and simulated by REAM at Wallops Island from April to August 2005. Coincidence criteria for OMI-MLS-derived column ozone are at  $\pm 3^\circ$  longitude,  $\pm 2.5^\circ$  latitude on the same day as the ozonesonde measurements. Ozonesonde data are obtained from the World Ozone and Ultraviolet Data Center (WOUDC).

350 hPa) due to the low bias in the prescribed upper boundary condition of O<sub>3</sub> from GEOS-CHEM simulations. Yang *et al.* [2007] has conducted comprehensive comparisons of the OMI-MLS tropospheric O<sub>3</sub> columns with ozonesonde measurements. As an illustration, we show the comparison of OMI-MLS tropospheric O<sub>3</sub> columns with ozonesonde measurements at Wallops Island (38°N, 75°W) in April-August, 2005 (Figure 4.2). The tropopause levels for ozonesonde column calculations are also taken from the NCEP reanalysis data. We also show the corresponding REAM simulation results. Compared with ozonesondes, both OMI-MLS and REAM underestimate tropospheric O<sub>3</sub> columns, the mean biases being -3 and -4 DU for OMI-MLS and REAM, respectively, and the correlation coefficients 0.81 and 0.82, respectively. The more extensive evaluation with 8 ozonesonde stations by Yang *et al.* [2007] shows a bias (-4.7 DU) at 35-60°N in summer. The OMI-MLS biases do not affect the results of this study.

#### 4.4.2 OMI Tropospheric Column NO<sub>2</sub>

NO<sub>x</sub> is a major precursor for tropospheric O<sub>3</sub> production. Figure 4.3 shows the average tropospheric NO<sub>2</sub> columns retrieved from OMI and simulated by REAM in the summer of 2005. Overall, the model results are in reasonably good agreement with OMI retrievals. Compared with the OMI tropospheric NO<sub>2</sub> column, REAM overestimates NO<sub>2</sub> columns by  $\sim 1 \times 10^{15}$  molecules cm<sup>-2</sup> over the Ohio Valley, where power plant NO<sub>x</sub> emissions are large. Frost *et al.* [2006] and Kim *et al.* [2006] found large reductions of NO<sub>x</sub> emissions from power plants. That reduction was not taken into account in the model. We compute the contribution of lightning to the NO<sub>2</sub> column by comparing the standard model results to a sensitivity simulation in which lightning NO production is

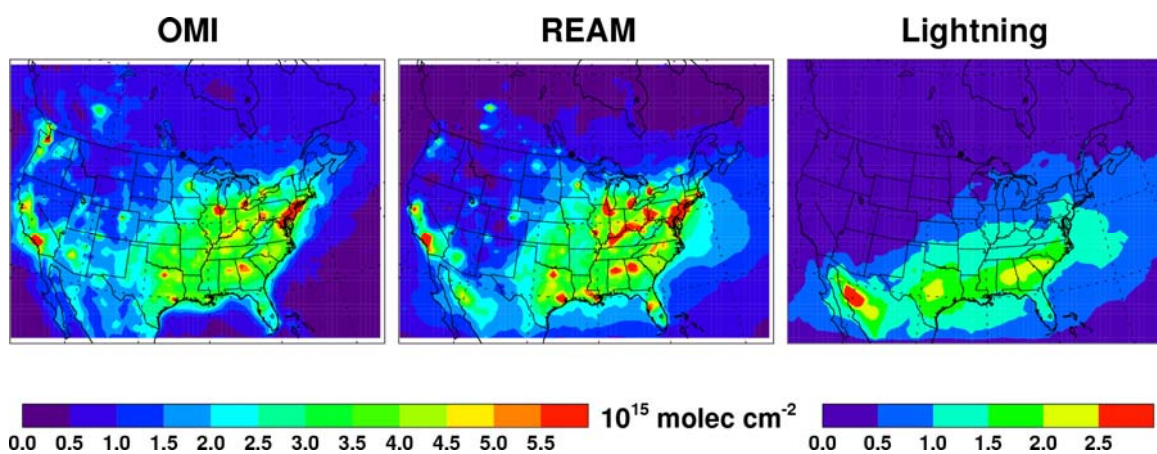


**Figure 4.3** Monthly mean tropospheric NO<sub>2</sub> columns during summer 2005 from OMI satellite measurements, those from REAM simulations (second column), and those contributed by lightning production in the model (third column). Only OMI data with cloud fractions of < 40 % are used. Corresponding model results are sampled at the same time as the OMI measurements.



turned off. Results show that the contribution of lightning appears to be overestimated over northern Mexico. REAM also simulates higher NO<sub>2</sub> column over the ocean than OMI. Compared to GOME [Choi *et al.*, 2005, 2007a] and SCIAMACHY [Martin *et al.*, 2006], the NO<sub>2</sub> columns retrieved from OMI over the western North Atlantic are lower. The reasons for this finding are unclear.

#### 4.4.3 TES UT O<sub>3</sub> and CO Measurements

Due to insufficient spatial coverage of TES O<sub>3</sub> and CO measurements over North America from April to June 2005, we use only TES observations in July and August. TES O<sub>3</sub> distributions are patchy due in part to measurement uncertainties. Compared with TES O<sub>3</sub> at 300 hPa (250-350 hPa), monthly mean REAM O<sub>3</sub> concentrations have a low bias of 5-6% and a correlation coefficient of 0.5. Comparisons with in situ measurements such as ozonesondes show that UT TES measurements tend to overestimate O<sub>3</sub> [Worden *et al.*, 2007] but the lightning-derived UT O<sub>3</sub> enhancements in the model are consistent with lightning-caused O<sub>3</sub> column peaks (Figure 4.1). Monthly mean UT O<sub>3</sub> enhancements due to lightning are larger than 20 ppbv over a large portion of the western North Atlantic, the southeastern and Gulf coasts, and the southern United States (Figure 4.4). These enhancements are larger than the uncertainties of monthly mean TES O<sub>3</sub> retrievals, which range from 5 to 20 ppbv.

Compared with TES CO at 300 hPa, REAM CO concentrations exhibit larger mean differences in July and August of -6.4% (R=0.44) and -7.4% (R=0.41), respectively (not shown), due to the approximately 30% overestimated CO emissions in the 1999 EPA NEI [Hudman *et al.*, 2007] and the UT CO underestimation of TES, as shown by Luo *et*

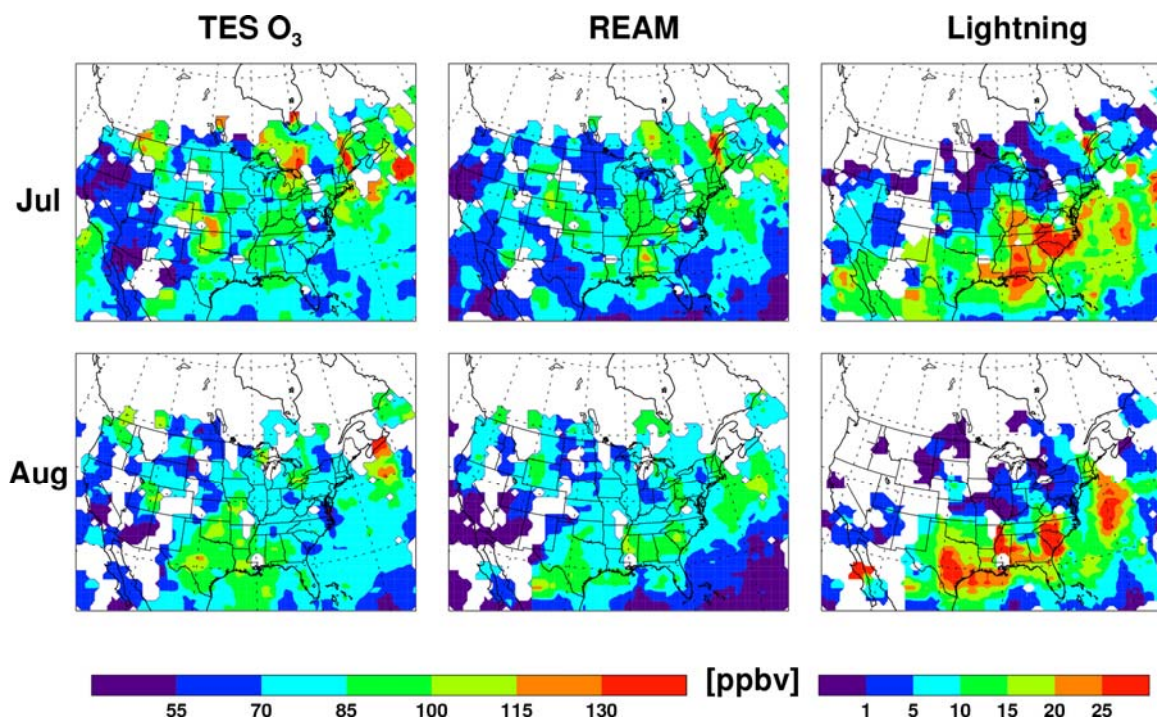


**Figure 4.4** Monthly mean tropospheric O<sub>3</sub> concentrations at 300 hPa (250-350) for July and August 2005 from measurements from the TES satellite measurements (first column), those from REAM (second), and those from the difference between REAM and the model turning off lightning NO<sub>x</sub> production (third). Only TES O<sub>3</sub> data with a degree of freedom of > 3.5 are used. Corresponding model results are sampled at the same time as the TES measurements.

*al.* [2007] from the comparisons with MOPITT CO. UT CO enhancements due to cloud convection that occurs over the southeastern coast, the southern United States, and the western North Atlantic, are generally consistent with O<sub>3</sub> column peaks due to convective outflow during the summer (Figure 4.1), but the REAM CO enhancements ranging from 6 to 20 ppbv are comparable to the uncertainties of monthly mean TES CO retrievals ranging from 10 to 15 ppbv.

#### **4.5 Conclusions**

The spatial distribution of O<sub>3</sub> and its precursors are strongly affected by cloud outflow and lightning NO<sub>x</sub> production. The tropospheric O<sub>3</sub> column by OMI and MLS, the tropospheric NO<sub>2</sub> column by OMI, and UT CO and O<sub>3</sub> by TES can be used to identify the impact of these transient factors using REAM. The OMI-MLS and TES independent satellite measurements show consistent convective outflow and lightning. Large enhancements of column and upper tropospheric O<sub>3</sub> comparable to those over the eastern United States are found over the western North Atlantic both in the satellite measurements and REAM simulations. The O<sub>3</sub> column peak region moves from the southern to northern North Atlantic due to convective outflow and lightning during spring to summer. Results of the model indicate large UT O<sub>3</sub> and CO enhancements due to lightning and cloud convection during the summer, suggesting that high-altitude aircraft campaigns will provide pivotal observations for evaluating model simulations and validating satellite observations. However, satellite uncertainties are still too large, so that model sensitivity is still critical to examine the underlying the detail mechanism of the factors. This study also provide opportunities for the future study of the impact of spatial

perturbations in the amount of O<sub>3</sub>, aerosols, and their precursors driven by cloud convection, lightning, and photochemistry on global climate change.

## CHAPTER V

### LATE-SPRING INCREASE OF TRANS-PACIFIC POLLUTION TRANSPORT IN THE UPPER TROPOSPHERE

#### 5.1 Introduction

Researchers have been concerned about the trans-Pacific transport of pollutants to North America [e.g., Andreae *et al.*, 1988; Merrill *et al.*, 1989; Kritz *et al.*, 1990; Parrish *et al.*, 1992]. They have been most concerned about the increase of pollution from Asia, particularly China, which has recently undergone dramatic economic growth, due to the resulting O<sub>3</sub> concentrations and their impact on the United States [e.g., Jacob *et al.*, 1999; Bernsten *et al.*, 1999]. For example, subsidence caused by high O<sub>3</sub> transported from Asia and produced catalytically by NO<sub>x</sub> (NO+NO<sub>2</sub>) during the oxidation of CO in addition to volatile organic compounds (VOCs) could significantly exceed standards set by the National Ambient Air Quality Standard at California mountain sites [Hudman *et al.*, 2004].

Previous analyses of the effects of trans-Pacific transport have focused on measurements of low-altitude O<sub>3</sub>, CO, and peroxyacetyl nitrate (PAN) [Jaffe *et al.*, 1999; Lin *et al.*, 2000; Jaffe *et al.*<sup>4</sup>, 2003]. However, this study will focus on two unexplored issues and evaluate current methods of simulating these observed features. One is to ascertain the differences between the characteristics of upper tropospheric trans-Pacific transport and those at lower altitudes; and the other is to determine the effects over North America of trans-Pacific transport on O<sub>3</sub> and its most critical precursor, NO<sub>x</sub>. To our

---

<sup>4</sup>This chapter is for “Late-spring increase of trans-Pacific pollution transport in the upper troposphere,” published at *Geophysical Research Letter* (33, L01811, doi:10.1029/2005GL024975). Authors are Y. Wang, Y. Choi, T. Zeng, B. Ridley, N. Blake, D. Blake, and F. Flocke.

knowledge, no one has examined the impact of trans-Pacific transport on North American  $\text{NO}_x$ .

This study will analyze the data from the Tropospheric Ozone Production about the Spring Equinox (TOPSE) experiment between February and May of 2000 [Atlas *et al.*, 2003]. The experiment, comprised of thirty-eight science flights in seven deployments (one to two weeks apart), took place in a region that spanned from Colorado to north of Thule, Greenland. The purpose of the experiment was to measure a comprehensive suite of chemical species relating to tropospheric  $\text{O}_3$  chemistry from the surface up to 8 km.

This research will analyze the measurements of the TOPSE experiment using REAM [Choi *et al.*, 2005] and the global GEOS-CHEM model [Bey *et al.*, 2001]. Within the continental United States and Canada, the REAM model domain covers a horizontal resolution of  $70 \times 70 \text{ km}^2$  and 21 layers up to 100 hPa in the vertical [Choi *et al.*, 2005]. To simulate the meteorological fields, this study employed the National Center for Atmospheric Research/Penn State MM5 using four-dimensional data assimilation along with the National Center for Environmental Prediction reanalysis, surface, and rawinsonde observations. Initial and hourly boundary conditions for trace gases were provided by the spring 2000 simulations that used the global GEOS-CHEM model (version 7.2.4 with a horizontal resolution of  $2^\circ \times 2.5^\circ$  and 30 layers up to 0.01 hPa, GEOS-3 meteorological fields). REAM shares the chemistry and deposition modules of GEOS-CHEM. More importantly, convective transport and lightning  $\text{NO}_x$  production schemes in the REAM are implemented [Choi *et al.*, 2005].

## 5.2 Results and Discussion

Results of the analysis of TOPSE 2000 showed that upper tropospheric reactive nitrogen  $\text{NO}_x$  and PAN increased the most during the late spring [Y. Wang *et al.*, 2003a]. Based on observed and simulated  $\text{NO}_x$  mixing ratios from March to May TOPSE aircraft observations, an initial investigation identified large increases of  $\text{NO}_x$  concentrations above 5 km, shown in Figure 5.1. The REAM is in reasonable agreement with the low concentrations in the upper troposphere observed in February (not shown) and March. However, since it simulates some enhancements in April, but none in May, it underestimates  $\text{NO}_x$  concentrations to a great extent. April REAM enhancements, which were not simulated in the global GEOS-CHEM model, are the result of localized convective transport and lightning  $\text{NO}_x$  production.

Because of the presence of a high-pressure ridge system residing over the western United States in May, neither the REAM nor the GEOS-CHEM model shows significant lightning and convective activity over the region, but measurements in each flight during this time (not shown) reveal four enhancements, which reach 200 km horizontally and 2 km vertically, with  $\text{NO}_x$  mixing ratios of  $>50$  pptv at altitude  $>6$  km. However, these measurements are often restricted by sampling. Two of the enhancements (not shown) were discernable but underestimated by the corresponding model simulations. Previous  $\text{NO}_x$  simulations that used differing regional (HANK [Hess *et al.*, 2000]) and global (MOZART-2 [Horowitz *et al.*, 2003]) CTMs also found model underestimations of 50% to 60% with several data points of simulated  $\text{NO}_x$  mixing ratios  $>50$  pptv above 5 km [Emmons *et al.*, 2003]. Nevertheless, these researchers did not provide reasons for such significant underestimation.

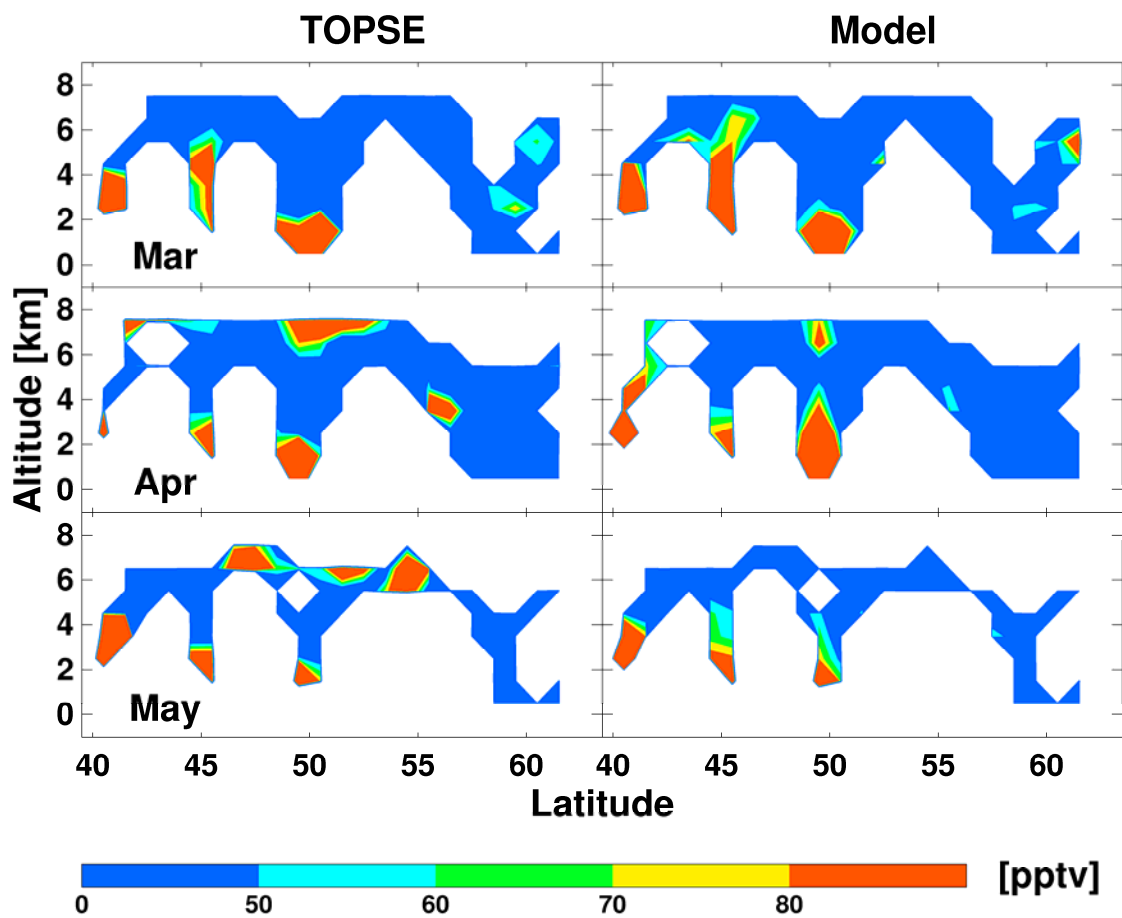


**Figure 5.1** Observed and REAM-simulated monthly mean distributions of  $\text{NO}_x$  from March to May 2000. The REAM data were sampled along the TOPSE flight tracks.



Overall, four different models with largely independent model formulations of convective transport and lightning parameterization and often drastically different meteorological fields and chemical formulations show that the models greatly underestimate upper tropospheric  $\text{NO}_x$  concentrations in April and May. However, this finding does not appear to be a poor representation of convection or lightning  $\text{NO}$  production. Model simulated  $\text{NO}_x$  enhancements due to local convection and associated lightning  $\text{NO}_x$  production are low due to the prevailing high-pressure ridge system over the western United States. In addition, previous comparisons of REAM simulations with satellite  $\text{NO}_x$  and  $\text{CO}$  observations indicate that the model reasonably captures observed day-to-day variations in lightning  $\text{NO}$  emissions and convective activity [Choi *et al.*, 2005]. Thus, we hypothesize that the trans-Pacific transport of pollutants in the upper troposphere into the region was underestimated in the models. This hypothesis can be better tested by examining the observations and simulations of other chemical tracers. We focus on a comparison in May when the pollutant enhancements are most significant.

Figure 5.2 shows a comparison of observed and simulated  $\text{CO}$ , PAN, and  $\text{O}_3$  concentrations in May. The REAM has distributions similar to GEOS-CHEM but with more localized enhancements. Hence, only the former is shown. Carbon monoxide is a good tracer for anthropogenic emissions, and peroxyacetyl nitrate is the reaction product of  $\text{NO}_2$  and peroxyacetyl radicals formed during the oxidation of VOC's. Therefore, it is a good tracer for tropospheric chemical activity of  $\text{O}_3$  precursors. While in reasonable agreement below 6 km, the simulated  $\text{CO}$ , PAN, and  $\text{O}_3$  concentrations are much lower than those from the observations at higher altitudes. The observed upper tropospheric enhancements of  $\text{CO}$ , PAN, and  $\text{O}_3$  tend to be collocated with those of  $\text{NO}_x$  (Figure 5.1).

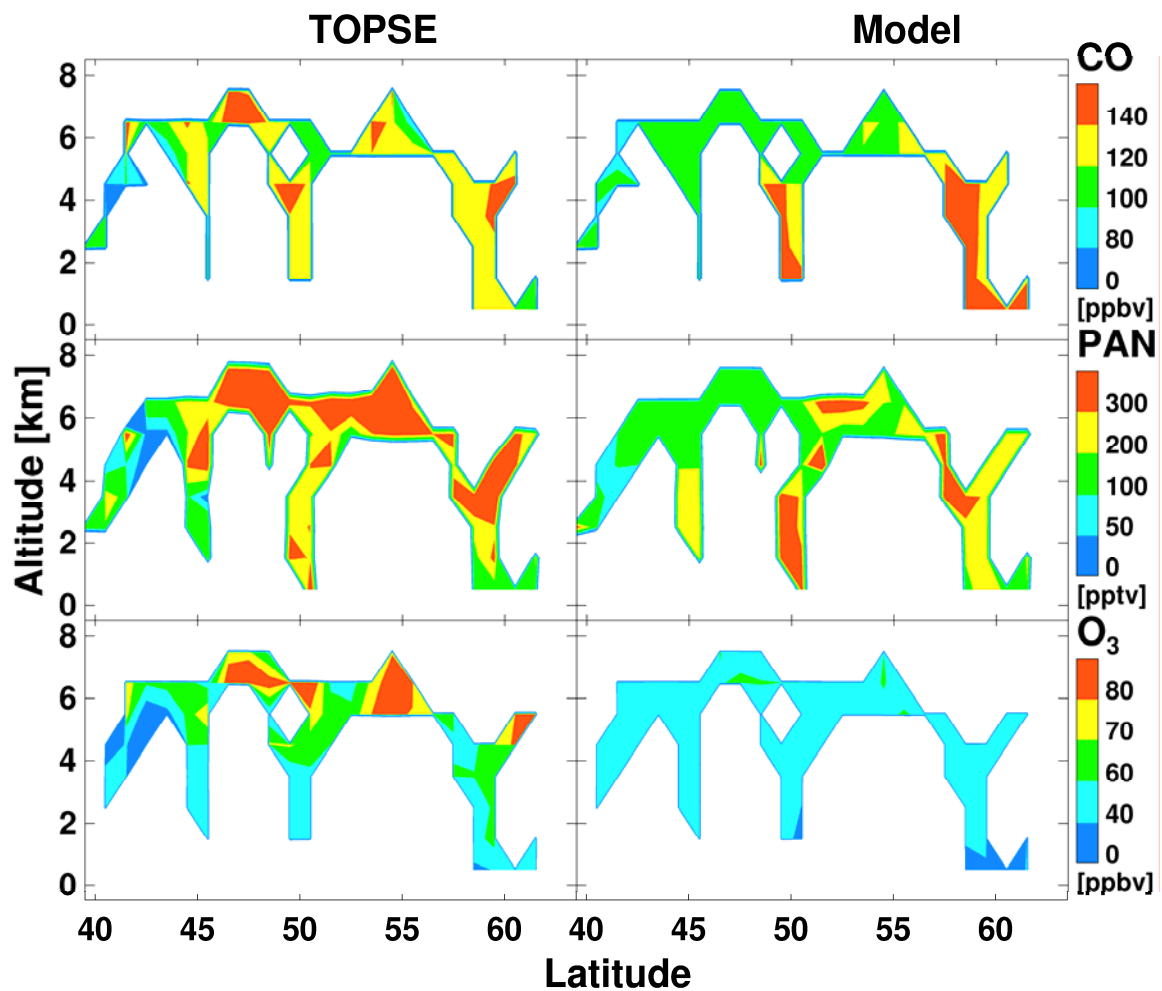


**Figure 5.2** The same as Fig. 5.1, but for CO, PAN, and O<sub>3</sub> in May. To filter out the effect of stratospheric O<sub>3</sub> when constructing the observed O<sub>3</sub> distribution, we did not include measurements with mixing ratios >110 ppbv.

A close inspection of the simulated  $O_3$  concentrations reveals slight enhancements in the upper tropospheric regions where high  $O_3$  was observed. The enhancements, which correspond to those in the GEOS-CHEM-simulated western boundary conditions, are not caused by photochemical production in the regional model, suggesting that the global model has some capability of simulating trans-Pacific transport [e.g., Hudman *et al.*, 2004]; however, the simulated magnitudes are too small.

The discrepancies between simulated and observed CO and PAN concentrations are much larger in May than they are in the three previous months (not shown). At lower altitudes (<6 km), the model reproduces the observed rapid decrease of CO well from April to May, but the decrease reflects more active photochemical oxidation towards summer. While the observations show a large increase of CO at higher altitudes (>6 km), the simulated concentrations are lower in May than April. The simulated PAN concentrations in May are similar to those in April at high altitudes, while the observations also show a large increase. The observed  $O_3$  mixing ratios at high altitudes show a clear increase from 50-60 ppbv in February to >80 ppbv in May (Figure 5.2) [Browell *et al.*, 2003]; the model does not reproduce the large increase.

We previously attributed 60% and 80% of the observed springtime  $O_3$  increase to photochemical production at mid and high latitudes, respectively [Y. Wang *et al.*, 2003b]. Thus, the upper tropospheric  $O_3$  problem in the model may be attributed to the large underestimation of  $NO_x$ . In addition, a direct observational evidence for the importance of photochemical  $O_3$  production catalyzed by  $NO_x$  can be seen in Figure 5.3, which shows the observed correlation between  $NO_x$  and  $O_3$  above 4 km in May. By examining the deviation from a normal mode in the CO cumulative probability distribution in May,

we identify two distinct data groups, CO <110 ppbv (lower 10<sup>th</sup> percentile) and CO >135 ppbv (upper 30<sup>th</sup> percentile). Low CO mixing ratios reflect a strong influence by either stratospheric or clean marine boundary layer air, while high CO mixing ratios indicate polluted air masses. The low CO data points show high O<sub>3</sub> mixing ratios of 150-220 ppbv with NO<sub>x</sub> of 80-110 pptv, reflecting the influence of stratospheric air since O<sub>3</sub> mixing ratios in the clean marine boundary layer are low.

The high CO data points show that O<sub>3</sub> mixing ratios increase to 120 ppbv while NO<sub>x</sub> mixing ratios reach 250 pptv. These high O<sub>3</sub> concentrations mainly reflect photochemical production of O<sub>3</sub> in polluted tropospheric air masses. Lightning affects the concentrations of CO or O<sub>3</sub> negligibly. Fresh local convection tends to produce higher CO and NO<sub>x</sub> concentrations through transport but relatively low O<sub>3</sub> concentrations and PAN/NO<sub>x</sub> ratios due in part to the time required for photochemical processing. Both the high PAN/NO<sub>x</sub> ratios of 5-40 (not shown) and >80 ppbv of O<sub>3</sub> with a moderate amount of NO<sub>x</sub> (~150 pptv) suggests that the air masses are photochemically aged and not significantly affected by local lightning or convective transport. Furthermore, inspection of back trajectories [Y. Wang *et al.*, 2003b] for data points with NO<sub>x</sub> >50 pptv in Figure 5.3 reveals that they are driven by trans-Pacific transport, not Pacific recirculation of pollutants emitted from the West Coast.

Our hypothesis that the observed large enhancements of upper tropospheric NO<sub>x</sub>, CO, PAN, and O<sub>3</sub> are due to trans-Pacific transport is also supported by the measurements of CFCs and Halon-1211 and back trajectory calculations. The production of CFCs and Halon-121 was phased out in developed countries in 1995 and will be

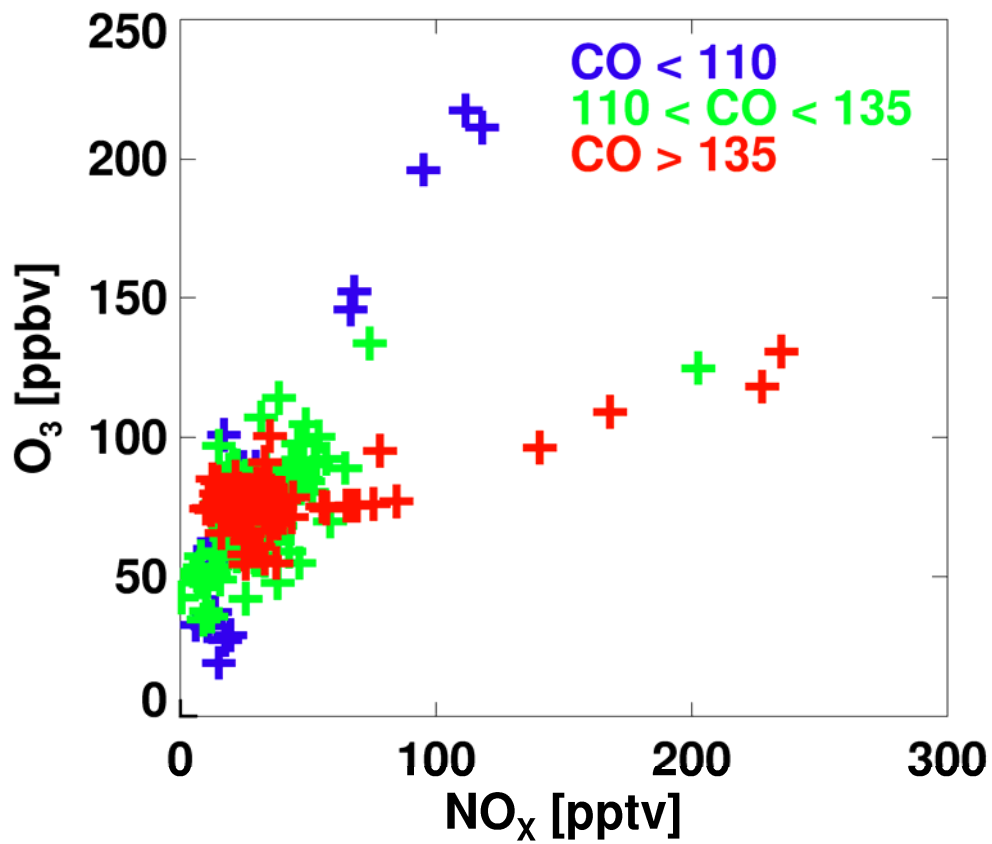


**Figure 5.3** Observed correlations between  $\text{O}_3$  and  $\text{NO}_x$ , grouped by CO mixing ratios (ppbv) in May. Only coincidental measurements of all three species above 4 km are included.

phased out in developing countries by 2010. Therefore, they are good tracers for air masses from East Asia. Observed CFCs and Halon-1211 exhibit similar features. Figure 5.4 shows the distribution of CFC-12 in May. The large enhancements at high altitudes ( $> 6$  km) tend to be consistent with those of  $\text{NO}_x$ , CO, PAN, and  $\text{O}_3$ . A close inspection of the measurements, which correspond to the enhancements of  $\text{NO}_x$  and CFC-12 observed at  $45\text{--}50^\circ$  N at high altitudes, reveals a general association of high  $\text{NO}_x$  concentrations with high CFC-12. However, the point-to-point correspondence is poor for two possible reasons. First, CFC-12 was sampled at a much lower frequency than  $\text{NO}_x$ . Secondly, the surface sources of  $\text{NO}_x$  and CFCs are not necessarily collocated, and  $\text{NO}_x$  concentrations are also affected by lightning production.

A major limitation of this work is that we do not know the exact origins for the observed trace gas enhancements. While TOPSE measurements are useful for examining the impact of trans-Pacific transport, the effects of specific distant sources become difficult to diagnose. Previous studies indicate that emissions of  $\text{NO}_x$  and CO are too low in China by  $\sim 50\%$  [Heald *et al.*, 2004; Y. Wang *et al.*, 2004]. In one sensitivity study (not shown), we doubled the Chinese surface emissions of these two gases. The large underestimation of upper tropospheric  $\text{NO}_x$  in TOPSE regions persists, likely reflecting the low export efficiency from the boundary layer and the short chemical lifetime of  $\text{NO}_x$ . Observed upper tropospheric CO enhancements are simulated well north of  $50^\circ$  N but still underestimated at lower latitudes. However, GEOS-CHEM now overestimates CO in February and March. TOPSE measurements do not show a strong increase in  $\text{CH}_3\text{Cl}$  in May, implying that the contribution from biomass burning to seasonal increases is limited.

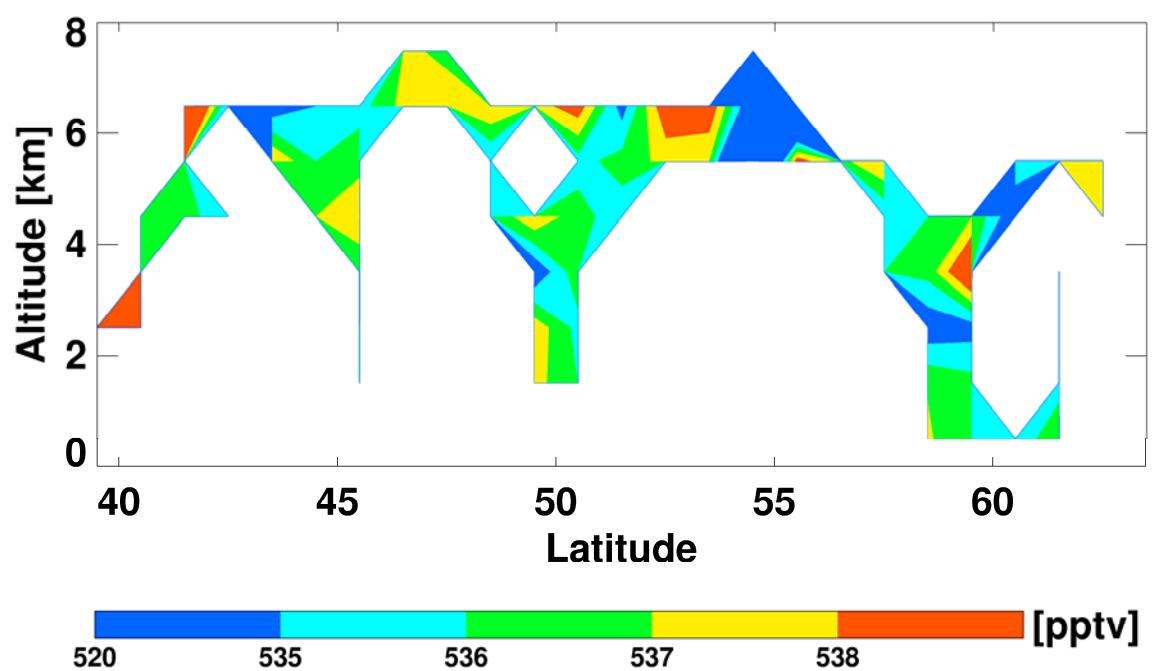


**Figure 5.4** Observed monthly mean distribution of CFC-12 in May.

It is possible that trans-Pacific pollutant transport surges in May due to a significant increase in convection and lightning over East Asia or the western Pacific (not simulated in the models). This possibility must be explored in a detailed analysis of other field measurements.

### 5.3 Conclusions

TOPSE observations show large enhancements of  $\text{NO}_x$ , PAN, CO,  $\text{O}_3$ , and CFCs at an altitude of  $>6$  km in May. We hypothesize that these enhancements are due to trans-Pacific transport. This hypothesis is supported by our analysis of the observations and model result. First, we find that these chemical tracers show consistent enhancement patterns at high altitudes. Both CFC enhancements and back trajectory calculations imply trans-Pacific transport from East Asia. In addition, we find that the  $\text{NO}_x$ - $\text{O}_3$  correlation for high CO data points indicates significant tropospheric photochemical production. We also find that the relatively high PAN/ $\text{NO}_x$  ratios of  $>5$  indicate photochemically-aged air masses. Finally, we show that separate regional/global chemical transport models using different meteorological fields and chemical formulations consistently underestimate the enhancements of  $\text{NO}_x$ , PAN, and CO. The contribution by North American surface emissions is limited in these simulations because the high-pressure ridge system over the western United States suppresses convection and lightning in May.

Our results indicate that the rapid late-spring increase of reactive nitrogen  $\text{NO}_x$  and PAN in the northern mid-latitude upper troposphere during TOPSE is most likely due to enhancements of these species by trans-Pacific transport. Such enhancements result in significant increases in photochemical oxidation and  $\text{O}_3$  production. The trace gas



enhancements, including those of CO, continue to increase in May. This phenomenon is very different from trans-Pacific transport-driven CO enhancements at low altitudes, which peaks in March and April [e.g., Weiss-Penzias *et al.*, 2004]. The current global CTMs do not capture this rapid seasonal transition, which results in a significant underestimation of the photochemical production of O<sub>3</sub> in the models. The problem raises concerns about our capability to assess the effects of intercontinental transport on regional air quality.

## CHAPTER VI

### ASSESSING THE PHOTOCHEMICAL IMPACT OF SNOW NO<sub>x</sub> EMISSIONS OVER ANTARCTICA DURING ANTCI 2003

#### 6.1 Introduction

In late November and December of 2003, the Antarctic Tropospheric Chemistry Investigation (ANTCI) took place [Esiele *et al.*, 2007]. Unlike the ISCAT 1998 and 2000 studies, both the tethered balloon observations at SP [Helmig *et al.*, 2007] and the Twin Otter aircraft plateau measurements gathered the critical spatial information about NO over Antarctica [Davis *et al.*, 2007]. We examined these measurements along with SP surface measurements by employing the 1-D and regional REAM models. On the basis of SP measurements, the 1-D model is to construct a snowpack NO<sub>x</sub> emission parameterization and then run 1-D model simulations to analyze the effects of vertical transport on reactive nitrogen. On the basis of balloon and Twin Otter measurements, the snowpack NO<sub>x</sub> emission parameterization is implemented in REAM to examine the effects of transport by advection and the spatial heterogeneity of snowpack NO<sub>x</sub> emissions. The focus of this modeling analysis is the plateau region, where NO<sub>x</sub> emission rates are expected to be the highest. Section 6.2 describes the models ; Section 6.3 presents a 3-D model construct of a snow NO<sub>x</sub> emission parameterization, and then Section 6.4 evaluates the 1-D and REAM simulations with surface measurements of reactive nitrogen. Finally, Section 6.5 presents a comparison of the 1-D and REAM model simulations with the balloon and Twin Otter measurements and then assesses the

---

<sup>5</sup>This chapter is for “Assessing the photochemical impact of snow NO<sub>x</sub> emissions over Antarctica during ANTCI 2003,” accepted in *Atmospheric Environment* in 2007. Authors are Y. Wang, Y. Choi, T. Zeng, D. Davis, M. Buhr, G. Huey, and W. Neff.

impact of snow NO<sub>x</sub> emissions on the reactive nitrogen budget and photochemistry over Antarctica. Finally, Section 6.6 concludes.

## **6.2 3-D Model Descriptions and the 1-D Model Setup**

The regional 3-D modeling system has two components, the polar version of the Penn State/National Center for Atmospheric Research mesoscale model MM5 and a regional chemistry and transport model. The models have a horizontal spatial resolution of  $80 \times 80 \text{ km}^2$ . There are 27 vertical layers up to 10 hPa, 13 of which are placed in the lowest 1 km in order to simulate the vertical distribution of trace gases in the boundary layer. In our simulations, the MM5 simulation domain is five grid boxes larger on each side than the chemical transport simulation domain such that any dynamic anomaly near the boundary does not affect transport in the chemical model.

We use the polar version of MM5 [Bromwich *et al.*, 2001; Cassano *et al.*, 2001], which provides better meteorological simulations in comparison to regular MM5 or other similar models because the model has specific physical parameterizations for polar regions. In our simulations over Antarctica, we use four-dimensional data assimilation conducted using the ECMWF reanalysis, rawinsondes, and surface observations. Most meteorological data are archived every 30 minutes. We archive turbulence statistics every 2.5 minutes in order to resolve turbulent transport in the boundary layer. We use the ETA Mellor-Yamada-Janjic (MYJ) 2.5-order closure scheme [Black, 1994] for the turbulence calculation.

The regional chemical transport model [Zeng *et al.*, 2003, 2006; Choi *et al.*, 2005, 2007a, 2007b; Y. Wang *et al.*, 2006; Jing *et al.*, 2006] adopts the photochemical and dry

and wet deposition modules from the GEOS-CHEM model [Bey *et al.*, 2001]. The model includes a detailed photochemical mechanism with about 200 reactions and 120 concentration-varying chemical species; 24 tracers (family or species) are transported to describe  $\text{O}_3$ - $\text{NO}_x$ -hydrocarbon chemistry. Recent kinetics data on  $\text{HNO}_4$  photolysis and thermal decomposition [Roehl *et al.*, 2002; Gierczak *et al.*, 2005] are used in this work. The transport scheme is that by Walcek [2000]. We apply the simulation results of the global GEOS-CHEM model to specify the initial and daily boundary conditions of trace gas concentrations in the regional model. GEOS-CHEM (version 5.02  $4^\circ$  latitude by  $5^\circ$  longitude resolution) is driven by GEOS-4 assimilated fields for 2003 by the NASA Global Modeling and Assimilation Office.

A 1-D model derived from the 3-D model with vertical transport only by turbulence is used to analyze the interaction of snow  $\text{NO}_x$  emissions, photochemistry, dry deposition, and turbulent transport in the boundary layer at SP. Therefore, the 1-D and 3-D models share the same vertical structure and meteorological fields (for SP in the 3-D model). GEOS-CHEM results are used for initial and upper chemical boundary conditions at 1 km in 1-D simulations, which is well above the shallow atmospheric boundary layer at SP [Neff *et al.*, 2007]. One objective of the 1-D simulations is to construct, on the basis of SP measurements, a parameterization of snow  $\text{NO}_x$  emissions that can be used in the 3-D model for Antarctica. We use the 1-D model for this purpose because the iterative 1-D  $\text{NO}_x$  flux analysis detailed in the next section cannot be executed within the 3-D model. We chose not to include the snow emissions of  $\text{H}_2\text{O}_2$  and  $\text{CH}_2\text{O}$  [Hutterli *et al.*, 2004] in this work for three reasons. First, measurements of  $\text{H}_2\text{O}_2$  at the SP show magnitudes ( $\sim 270$  pptv) similar to those in 2000 reported by Hutterli *et al.*

[2004]. However, CH<sub>2</sub>O mixing ratios (20-60 ppbv) are lower than the values in 2000 (50-150 ppbv). Model simulations for ANTICI 2003, constrained by observed concentrations of O<sub>3</sub>, NO, hydrocarbons, and water vapor and photolysis rates of J(O<sup>1</sup>D) and J(NO<sub>2</sub>), show CH<sub>2</sub>O values in the range of the 2000 measurements (50-120 ppbv) but higher than the 2003 measurements, implying a photochemical sink for CH<sub>2</sub>O in snow rather than a source during ANTICI 2003. Second, measurements of H<sub>2</sub>O<sub>2</sub> in 2003 are fairly constant (~200 ppbv higher than the model results). We are unable to parameterize the diagnosed emissions as functions of other variables as we did with snow NO<sub>x</sub> emissions. Without H<sub>2</sub>O<sub>2</sub> measurements in other regions, we cannot extend the emissions to other regions of Antarctica in the 3-D model. Finally, as discussed in Chen *et al.* [2004], the photochemical model (without snow emissions of H<sub>2</sub>O<sub>2</sub>) overestimates OH measurements. Similar discrepancies were found in the 2003 experiment. Inclusion of snow H<sub>2</sub>O<sub>2</sub> emissions will further increase model overestimates. Thus, more targeted measurements will be needed to resolve the disagreement between simulated and measured OH [Chen *et al.*, 2004]. We will take this uncertainty into consideration when analyzing the results of the 3-D model, but we will not further discuss the model-measurement comparisons with regard to HO<sub>x</sub> chemistry, which would largely be a duplication of work by Chen *et al.* [2004].

### **6.3 Snow NO<sub>x</sub> Emission Flux Parameterization**

We apply the 1-D model to estimate the snow NO<sub>x</sub> emissions based on trace gas measurements at SP. We assume that the emissions are in the form of NO<sub>2</sub> [Jones *et al.*, 2000]. Davis *et al.* [2004], however, showed that NO and NO<sub>2</sub> are in photochemical

equilibrium at the surface, based on measurements taken at -20 cm to the surface. Whether the emissions are in the form of NO or NO<sub>2</sub> does not change the simulation results because these species reach photochemical equilibrium in minutes in the plateau atmosphere with the amount of O<sub>3</sub> present. We first compare simulated meteorological variables to the measurements at SP.

### 6.3.1 Effects of Turbulence on Boundary Layer Height and Surface Temperature and Wind Speed

A key measurement pertinent to the model flux estimation is that of boundary layer height, estimated using the Sound Detection and Ranging (SODAR) instrument. Based on the backscattered signals (due to boundary layer turbulence structures), an automatic algorithm [Neff *et al.*, 2007] that identifies the boundary layer height was applied. The maximum range of the instrument, as configured for the ANTCI 2003 study, was 180 m. The simulated diffusion coefficient drops rapidly to a minimum value at the top of the boundary layer. Therefore, we define the boundary layer height in the model as the altitude at which the turbulence diffusion coefficient drops to a value equivalent to 10 times the minimum value specified in the model. Based on this approach, the polar MM5 simulation using the original ETA MYJ 2.5-order closure scheme clearly underestimates SODAR measurements since the boundary layer only occasionally extends beyond the first model layer (Figure 6.1). Further analysis reveals a problematic assumption in the MM5 MYJ turbulence scheme implementation, i.e., the default minimum diffusion coefficient is set at  $0.09 \text{ m}^2 \text{ s}^{-1}$ . While a reasonable minimum value for mid-latitude North America, it is too high over the polar region, where the surface roughness of snow is very

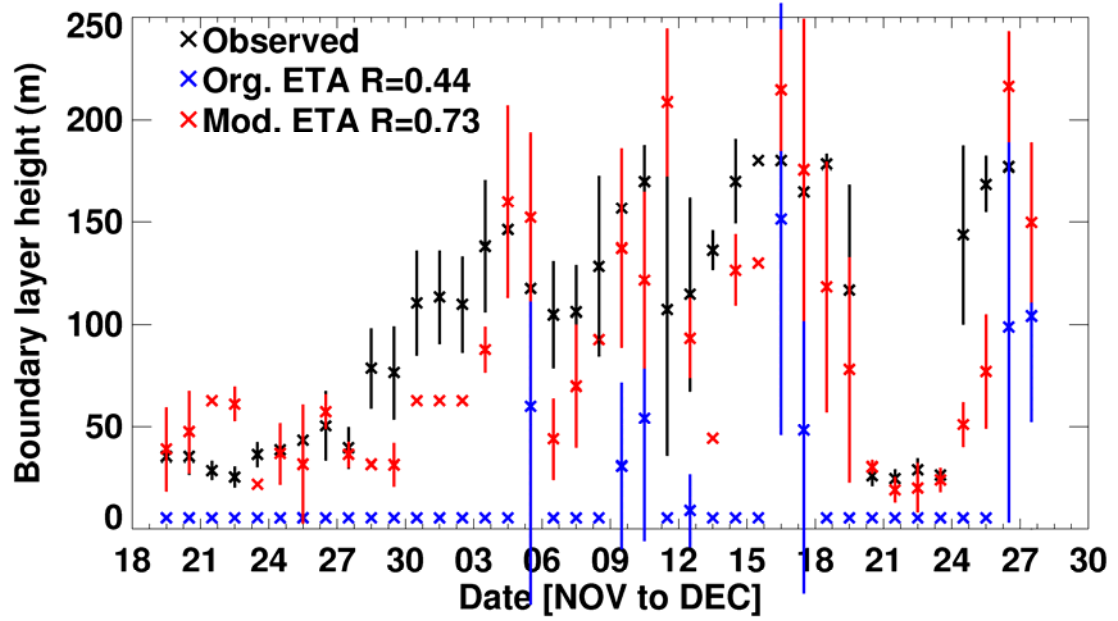


**Figure 6.1** Observed and simulated daily boundary layer heights at SP during ANTICI 2003. Simulation results using the original and modified ETA MYJ turbulence scheme are shown. The vertical bar shows the daily standard deviation. The maximum altitude measurable by SODAR is 180 m.

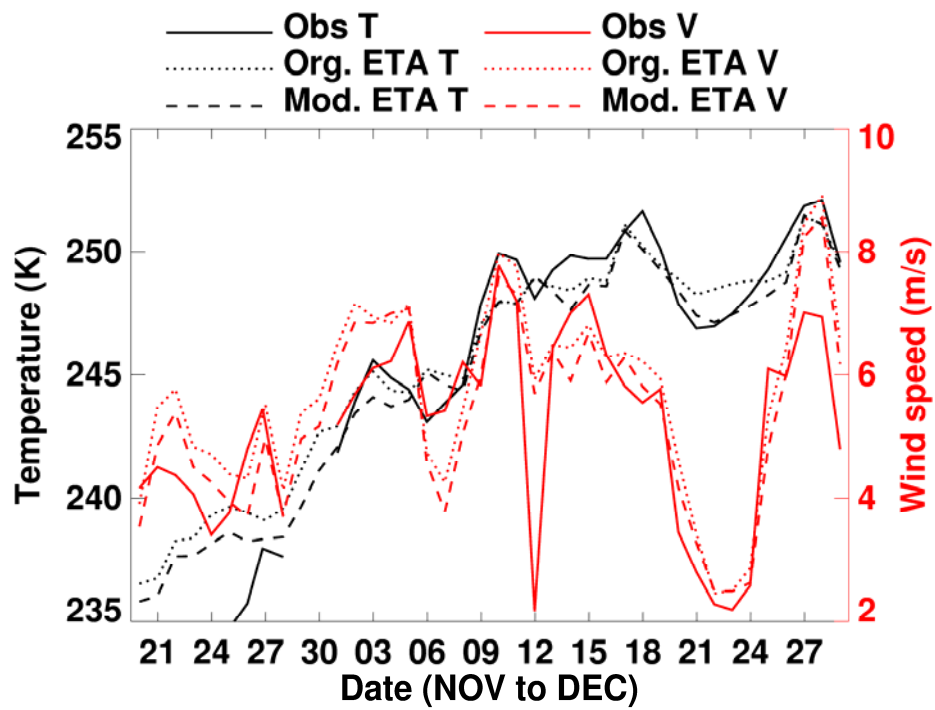


**Figure 6.2** The same as Figure 6.1, but for temperature and wind speed. “T” denotes temperature and “V” denotes wind speed.



low. Thus, we decreased the minimum value to  $0.001 \text{ m}^2 \text{ s}^{-1}$ . With this adjustment, the simulated boundary layer height is much higher and in reasonable agreement with the SODAR measurements, particularly in light of the model's vertical resolution and the uncertainty in the SODAR boundary layer height detection algorithm [Neff *et al.*, 2007]. The correlation coefficient of observed and simulated boundary layer heights improves from 0.44 to 0.73.

Simulated surface wind speed and temperature at SP are not strongly affected by the modification of the turbulence scheme (Figure 6.2). However, some improvement in temperature simulations can be observed. Polar MM5 has a warm bias in late November. When the minimum diffusion coefficient is reduced to  $0.001 \text{ m}^2 \text{ s}^{-1}$ , the warm bias is reduced (but not eliminated). Model-simulated friction velocity ( $u_*$ ) values are in good agreement with sonic anemometer measurements in the second half of December (not shown). The surface stress simulation is not significantly affected by changing the minimum diffusion coefficient in the model. Additional evidence was found in our recent model analysis of (halogen-driven) ozone depletion events in Alert, Canada, in which the model simulations of surface ozone in Alert were much improved in May when the minimum diffusion coefficient decreased from 0.09 to  $0.001 \text{ m}^2 \text{ s}^{-1}$  [Zeng *et al.*, 2006]. Thus, we adjusted the minimum diffusion coefficient to the lower value for our simulations.

### 6.3.2 Snow $\text{NO}_x$ Emission Flux Estimation and Parameterization

We constrain the 1-D model with observed concentrations of  $\text{O}_3$ , hydrocarbons, water vapor, and the photolysis rates of  $J(\text{O}^1\text{D})$  and  $J(\text{NO}_2)$ . Trace gas measurements

were made on the second floor of the Atmospheric Research Observatory (ARO), approximately 10 m above the snow surface. The presence of the ARO building induces local-scale mixing; thus, we consider these measurements as averages for the lowest model layer (0-10 m). All measurements have higher measurement frequencies than hour<sup>-1</sup>; hourly averages are used in the model analyses. The surface NO<sub>x</sub> concentrations in the model are determined by an influx from the snow pack, an outflux to higher altitudes, and chemical production and loss. Other than the snow emission flux, all other terms are calculated in the 1-D model. With measurements of NO, we can therefore derive snow NO<sub>x</sub> emission fluxes using the model. Our initial guess of the snow emission is  $3.9 \times 10^8$  molec cm<sup>-2</sup> s<sup>-1</sup> [Oncley *et al.*, 2004]. This emission flux is adjusted iteratively until model-simulated surface NO concentrations match the measurements (to <1% each hour) or if the flux is reduced to 0. The derived daily snow NO<sub>x</sub> flux is shown in Figure 6.3. The average emission flux derived from the 1-D model is  $3.2 \times 10^8$  molec cm<sup>-2</sup> s<sup>-1</sup>, which is 20% lower than the mean flux of  $3.9 \times 10^8$  molec cm<sup>-2</sup> s<sup>-1</sup> estimated by Oncley *et al.* [2004] using sonic anemometer/thermometers and NO measurements in late November/early December of the ISCAT 2000 study. The reasonable agreement found between NO<sub>x</sub> flux estimates for ISCAT 2000 and ANTICI 2003 could be fortuitous. However, additional flux measurements/model analyses are needed to provide more substantial constraints on the year-to-year variability of snow emissions at the site.

Superimposed on the NO<sub>x</sub> flux are observed and simulated temperature and wind speed in Figure 6.3. The derived flux appears to show anti-correlations with temperature and to some extent with wind speed. Other variables, such as surface pressure and humidity, do not significantly correlate or anti-correlate with the derived NO<sub>x</sub> flux. Here,

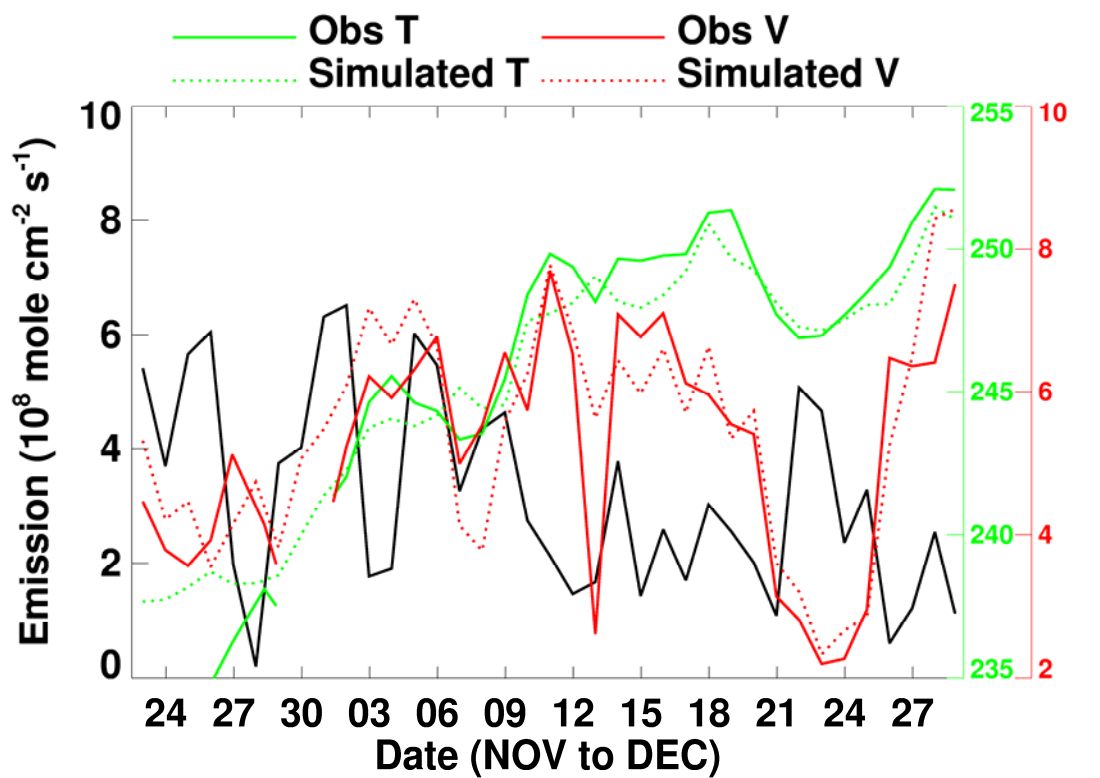


**Figure 6.3** 1-D model derived daily snow  $\text{NO}_x$  emissions, and observed and simulated temperature and wind speed at SP. The black line shows model-derived snow  $\text{NO}_x$  emissions. “T” denotes temperature (K) and “V” denotes wind speed ( $\text{m s}^{-1}$ ).

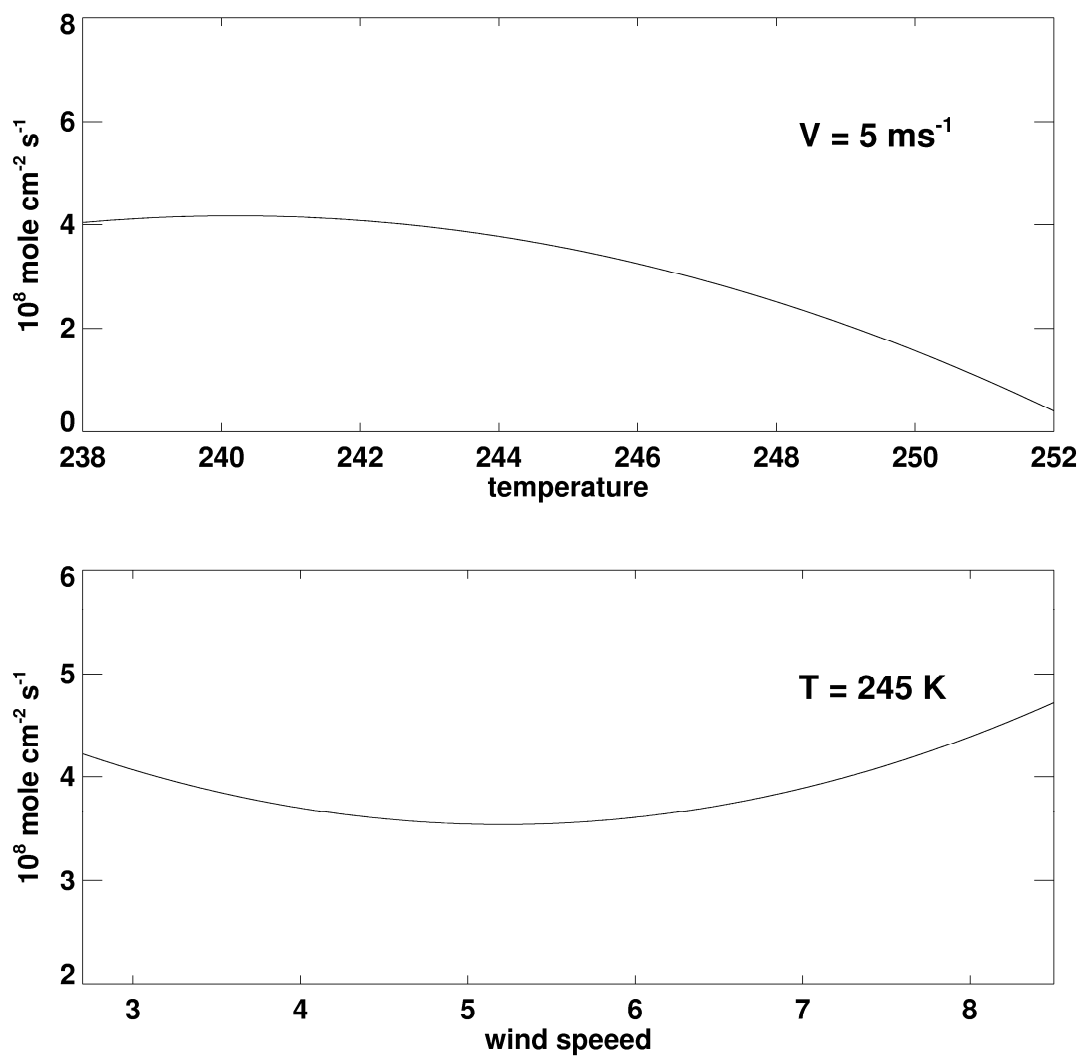


**Figure 6.4** Parameterized snow pack NO<sub>x</sub> emission flux as a function of temperature (K) at a wind speed of  $5 \text{ m s}^{-1}$  and as a function of wind speed ( $\text{m s}^{-1}$ ) at a temperature of 250 K.

the emission flux was parameterized on a daily basis as polynomials of simulated wind speed and temperature up to the 2<sup>nd</sup> order and obtained

$$\text{NO}_x \text{ flux} = -1009 + 8.38T - 0.0173T^2 + 2.008v + 0.0689v^2 - 0.011vT, \quad (1)$$

where the flux is in  $10^8 \text{ molec m}^{-2} \text{ s}^{-1}$ , temperature  $T$  in K, and wind speed  $v$  in  $\text{m s}^{-1}$ .

Figure 6.4 shows the parameterized flux as a function of temperature at a wind speed of  $5 \text{ m s}^{-1}$  and as a function of wind speed at a temperature of 245 K. We see that the derived snow  $\text{NO}_x$  emission tends to increase as the temperature decreases; but the rate of change increases as the temperature increases at the high end. By comparison, the flux dependence on wind speed is relatively weak and nonlinear. Generally speaking, the derived snow emission rate tends to increase as wind speed decreases at the low end, but tends to increase as wind increases at the high end. The flux variation with wind speed is relatively small.

The ranges in temperature and wind speed in the parameterization are limited by the measurements at SP (a temperature from 238 to 252 K and a wind speed from 2 to 9 m/s). When applied in the 3-D model, both the temperature and the wind speed can exceed these ranges. We linearly extrapolate the parameterization for temperatures up to 260 K when flux is  $>0$ . The flux dependence on wind speed is weak; we do not use any extrapolation, i.e., out-of-bound wind speeds are replaced by the respective bound values. We did not find significant correlations of the derived snow  $\text{NO}_x$  emission flux with ozone column density, solar zenith angle, or values of  $J(\text{O}^1\text{D})$  or  $J(\text{NO}_2)$ . It appears that the lack of any correlation is due in part to the relatively small range of values for these photochemical parameters at SP. Emissions of  $\text{NO}_x$  from the snow pack are allowed only during daylight conditions in the 3-D simulations.

An empirical emission parameterization is constructed here to sidestep the lack of fundamental and quantitative knowledge of the snow  $\text{NO}_x$  emission process such that measurements from ANTICI 2003 can be analyzed via the model simulations to improve our understanding of photochemical processes over Antarctica. As a result, use of the emission parameterization in other periods may lead to significant errors. A more process-based parameterization of the snow pack  $\text{NO}_x$  emission rate should consider, for example, nitrate concentrations in snow [Simpson *et al.*, 2002; Wolff *et al.* 2002]. However, available snow nitrate measurements over Antarctica are currently very limited in space and time [e.g., Kreutz and Mayewski, 1999] and we do not have the necessary measurements to test the structure of snow nitrate distribution as simulated by Wolff *et al.* [2002]. Interestingly, model estimated snow pack  $\text{NO}_x$  emissions at SP by Wolff *et al.* [2002] are a factor of 3-4 lower than the measurement by Oncley *et al.* [2004] during ISCAT 2000 or the derived average flux from this study. The discrepancy underscores the need for additional laboratory and field measurements that constrain the process-based snow pack emission models.

#### **6.4 Evaluations with Surface Reactive Nitrogen Measurements at SP**

We apply the derived snow pack  $\text{NO}_x$  emission parameterization in the 1-D and 3-D models. We compare 1-D and 3-D model-simulated NO mixing ratios with the observations at SP in Figure 6.5a. Additional input to the 1-D model consisted of surface measurements of  $\text{O}_3$ , hydrocarbon concentrations, water vapor, and the photolysis rates for  $\text{J}(\text{O}^1\text{D})$  and  $\text{J}(\text{NO}_2)$ . However, these measurement constraints could not be applied to the 3-D simulations. In the 1-D simulation, snow  $\text{NO}_x$  parameterization as a function of

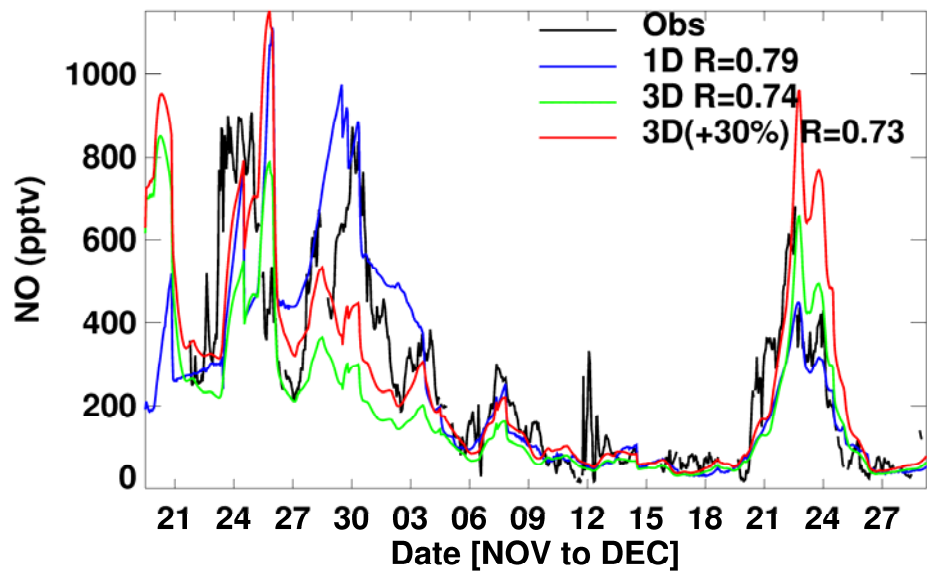


**Figure 6.5a** Observed and 1-D and REAM model simulated near-surface NO mixing ratios at SP. In the second 3-D simulation, parameterized snow NO<sub>x</sub> emissions increase by 30%.

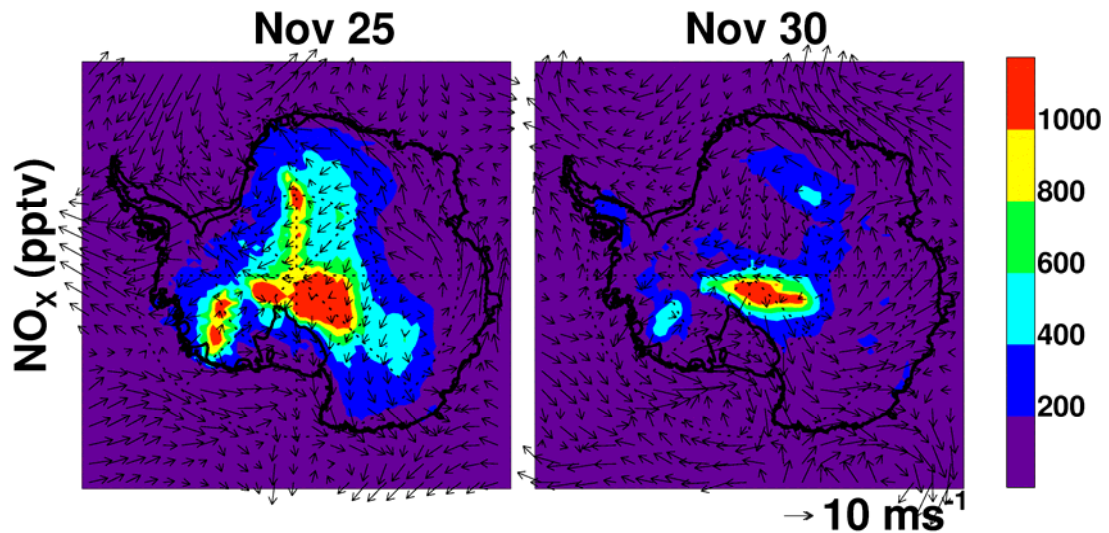


**Figure 6.5b** Simulated surface NO<sub>x</sub> mixing ratios (pptv) and wind at 1200 UT on November 25 and 30, 2003.

temperature and wind speed is used. In the first 3-D simulation, the original model-derived daytime snow emission parameterization is applied over the entire Antarctic continent. In the second 3-D simulation, the parameterized snow emissions are increased by 30%.

The observed high NO episodes on November 25, 30, and December 8, 23 are generally reproduced by the model simulations. Sensitivity results indicate that stable and shallow boundary layers during those periods are main drivers for the developments of high surface NO<sub>x</sub> concentrations [Davis *et al.*, 2004]. The correlation coefficient between observed and 1-D simulated surface NO concentrations is 0.79. In the 3-D simulation with the original snow NO<sub>x</sub> emission parameterization, the model has a tendency to underpredict the observed values; the correlation coefficient is slightly lower at 0.74. Sensitivity analysis indicates that downward advection of lower NO<sub>x</sub> concentrations from above in general and horizontal advection of low NO<sub>x</sub> air on occasion are key factors in reducing surface NO<sub>x</sub> concentrations at SP in the 3-D model compared to the 1-D model. The assumption of zero mean vertical and horizontal advection used in eddy correlation measurements and in the 1-D model could be in error because of large-scale downslope katabatic flow over Antarctica. The 3-D model results are improved by increasing snow NO<sub>x</sub> emissions by 30%. The increase in NO<sub>x</sub> during high NO<sub>x</sub> episodes is higher than 30%, partly because of the nonlinear relationship between NO<sub>x</sub> lifetime and its mixing ratio [Davis *et al.*, 2004]. The difference between the 1-D and 3-D models indicates the eddy correlation method tends to underestimate snow NO<sub>x</sub> emissions, as it does not account for advection. Therefore, all the 3-D model results presented hereafter are taken from the simulation with a 30% increase in snow NO<sub>x</sub> emissions.



The 3-D model was able to simulate low  $\text{NO}_x$  concentrations around December 2, not captured by the 1-D model. However, the 3-D model clearly underestimates the  $\text{NO}_x$  episode around November 30 while reproducing the earlier episode around November 25. Horizontal gradients and transport appear to play important roles. Figure 6.5b compares surface  $\text{NO}_x$  concentrations and wind transport over Antarctica between November 25 and 30 (1200 UT). The model predicts more extensive high surface  $\text{NO}_x$  concentrations on November 25 than on November 30. While the high  $\text{NO}_x$  distribution is nearly homogeneous around SP on November 25, a large spatial gradient is simulated around SP on November 30. Simulated surface winds are in good agreement with ANTICI measurements on November 25 and with Automatic Weather Station (AWS) measurements on November 30. We use AWS data for the latter day, when ANTICI wind measurements were unavailable. Along the  $0^\circ$  meridian, prevailing transport on November 25 is from the high-elevation plateau, where  $\text{NO}_x$  emissions are high; prevailing transport on November 30 is from a northern low-elevation region, where  $\text{NO}_x$  emissions are low. Low- $\text{NO}_x$  transport is important for the creation of the spatial  $\text{NO}$  gradient around SP on November 30 in the 3-D model. Thus, the underestimation in the 3-D model, but not in the 1-D model, suggests that this low- $\text{NO}_x$  transport is exaggerated in the 3-D model; possible reasons for these findings are errors in the snow  $\text{NO}_x$  emission distribution or wind transport and coarse model spatial resolution.

Figure 6.6 shows compares observed and simulated surface  $\text{HNO}_3$  at SP. Since  $\text{HNO}_3$  concentrations strongly depend on  $\text{NO}_x$  concentrations, model errors in  $\text{NO}$  will propagate into  $\text{HNO}_3$  simulations. To eliminate this error, we added another 1-D simulation in which surface  $\text{NO}$  concentrations are specified as observed, so snow  $\text{NO}_x$

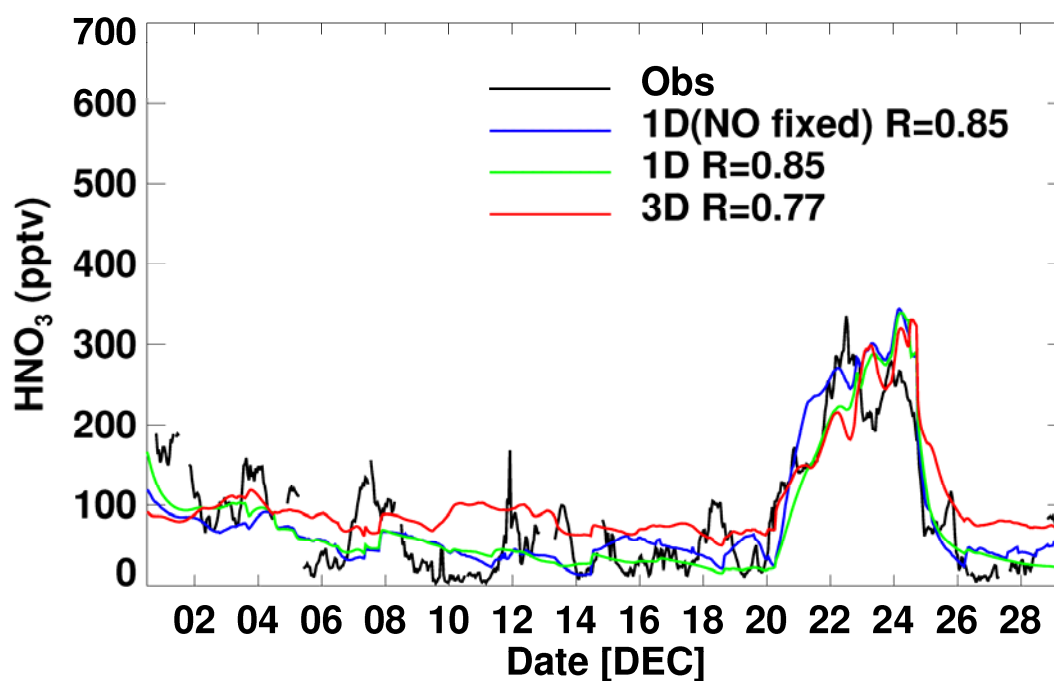


**Figure 6.6** The same as Figure 6.5a, but for  $\text{HNO}_3$ . In the first 1-D simulation, surface NO is specified as observed. In the second 1-D simulation, snow  $\text{NO}_x$  emission parameterization is used. In the 3-D simulation, parameterized snow  $\text{NO}_x$  emissions (Eq. (6.1)) are increased by 30%. The measurement accuracy of  $\text{HNO}_3$  is 20% [Huey *et al.*, 2004].

emission parameterization is not used in this simulation. The dry deposition velocity in the models is calculated with the resistance-in-series scheme by Wesely [1989]. The aerodynamic resistance is computed based on ETA MYJ turbulence output. The snow surface resistance of  $\text{HNO}_3$  also follows Wesely [1989]. The calculated average deposition velocity during ANTICI 2003 is  $0.15 \text{ cm s}^{-1}$ . The model result shows reasonable agreement with the measurements, revealing low  $\text{HNO}_3$  concentrations between December 3 and 20 and high concentrations between December 21 and 24. The correlation coefficients are 0.85 and 0.77 for the 1-D and 3-D models, respectively. Both models tend to overestimate  $\text{HNO}_3$  concentrations at low  $\text{HNO}_3$  values. However, the positive bias of the 3-D model is considerably larger; after presenting the results for  $\text{HNO}_4$ , we will discuss the reasons for the bias.

In the  $\text{HNO}_4$  simulations, we assume that dry deposition of  $\text{HNO}_4$  to snow is as fast as it is of  $\text{HNO}_3$  [Slusher *et al.*, 2002]. Therefore, the average of calculated dry deposition velocities for  $\text{HNO}_4$  is  $0.15 \text{ cm s}^{-1}$ . Figure 6.7a, in which observed and simulated  $\text{HNO}_4$  at SP are compared, the 1-D simulations generally show agreement of the measurements, except for low bias before December 9. However, the observed variability is severely underestimated. The correlation coefficients are 0.63.

In the 1-D model, near-surface  $\text{HNO}_4$  is determined by chemical production and loss, turbulent diffusion transport, and dry deposition. We examine each term to investigate which of these factors is likely the major contributor to the high-frequency variations in the measurements. Figure 6.7b shows the time series of each term in December. In this simulation, surface NO is specified as observed. The magnitudes of the four terms are comparable. Chemical production is generally larger than chemical loss,

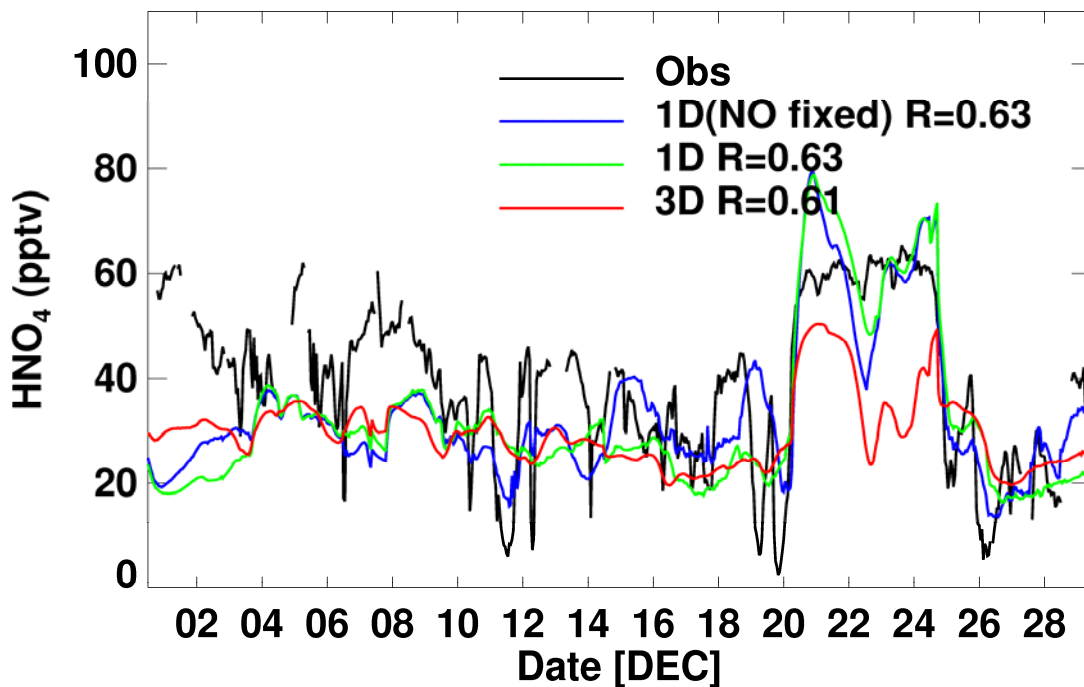


**Figure 6.7a** Same as Figure 6.6, but for  $\text{HNO}_4$ . The measurement accuracy of  $\text{HNO}_4$  is 30%.

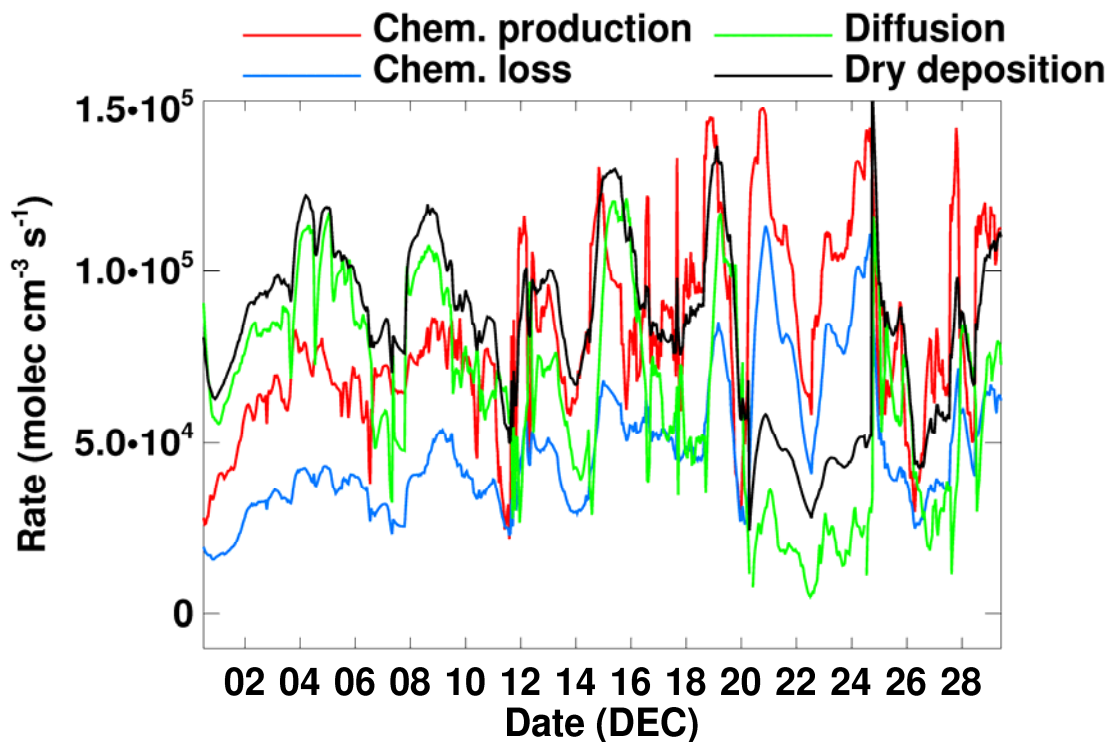


**Figure 6.7b** Simulated chemical production, loss, turbulent diffusion transport, and dry deposition rates for  $\text{HNO}_4$  near the surface (0-10 m) in the 1-D model.

and dry deposition loss is generally larger than turbulent influx from above. During the episode on December 21-24, both turbulent transport and dry deposition are low because of the establishment of a shallow stable boundary layer (Figure 6.1). Neither thermal deposition nor photolysis exhibits high-frequency variations, nor does the simulated aerodynamic resistance vary in high frequency. Major portions of high-frequency variations in chemical loss and dry deposition rates are driven by variability in the simulated  $\text{HNO}_4$  concentration. The chemical production rate does exhibit large high-frequency variations, particularly between December 12 and 19. However, the high-frequency variation is modulated by turbulent transport. The initial large pulse of  $\text{HNO}_4$  production is compensated by a decrease in turbulent transport from above. If high  $\text{HNO}_4$  production driven by snow  $\text{NO}_x$  emissions continues, the production of  $\text{HNO}_4$  in the layers above also increases as  $\text{NO}_x$  is transported upward by turbulence, resulting in an accumulation of  $\text{HNO}_4$  and an increase in turbulent influx of  $\text{HNO}_4$  to the surface layer. The slower response of the 1-D model-simulated  $\text{HNO}_4$  to  $\text{NO}$  variation may indicate that turbulent transport between the lower model layers is overestimated. The correlation coefficient between 3-D model-simulated and observed  $\text{HNO}_4$  is 0.61. The 3-D model simulation is considerably lower than 1-D simulated and measured  $\text{HNO}_4$  during the high-concentration episode on December 21-24. Increasing the snow resistance to  $\text{HNO}_4$  deposition decreases dry deposition and increases  $\text{HNO}_4$  concentrations. A 50% increase in snow resistance pushes the  $\text{HNO}_4$  mixing ratios to the upper bound of observed values prior to December 20, but the model still underestimates the values on December 21-24 since aerodynamic resistance during this period is high, reducing the dry deposition velocity by a factor of 4 from the earlier period. An inspection of the 3-D

model results reveals that advection of low  $\text{HNO}_4$  to SP on December 21-24 contributes significantly to the low bias in the model.

To further clarify the model results, we compare the 1-D and 3-D simulated mean vertical profiles of  $\text{NO}$ ,  $\text{HNO}_3$ ,  $\text{HNO}_4$  during ANTICI 2003 (Figure 6.8). The 1-D simulation with surface  $\text{NO}$  concentrations specified to the measurements are similar to that with parameterized snow  $\text{NO}_x$  emissions. Despite 30% higher emissions, the simulated  $\text{NO}$  profiles in the 3-D model are very similar to the 1-D profiles. A clear drop off in the  $\text{NO}$  profiles is evident at about 50 m, the altitude at which the boundary layer top generally resides under stable conditions. The difference between the 1-D and 3-D model vertical profiles is much larger for  $\text{HNO}_3$  and  $\text{HNO}_4$ . Both gases show higher values at 50 m than at the surface, suggesting that vertical mixing together with advection might represent an effective loss process for reactive nitrogen from the plateau. It is also noteworthy that the estimated concentrations of both gases over the altitude range of 50-500 m when calculated using the 3-D are higher than they are using the 1-D model. These higher concentrations in the 3-D model are driven in part by advection from high plateau regions, a process not simulated in the 1-D model. While not affecting surface  $\text{HNO}_4$  concentrations significantly, the accumulation extends to the surface for  $\text{HNO}_3$  because  $\text{HNO}_3$  has a longer chemical lifetime than  $\text{HNO}_4$ . Although model-calculated dry deposition is adequate in the 1-D simulations, the overestimates of  $\text{HNO}_3$  in the 3-D model indicate a need for lower snow resistance and thus higher  $\text{HNO}_3$  deposition. The slightly lower  $\text{HNO}_4$  concentration at 0-50 m in the 3-D than that in the 1-D model is due in part to underestimation during the episode on December 21-24.

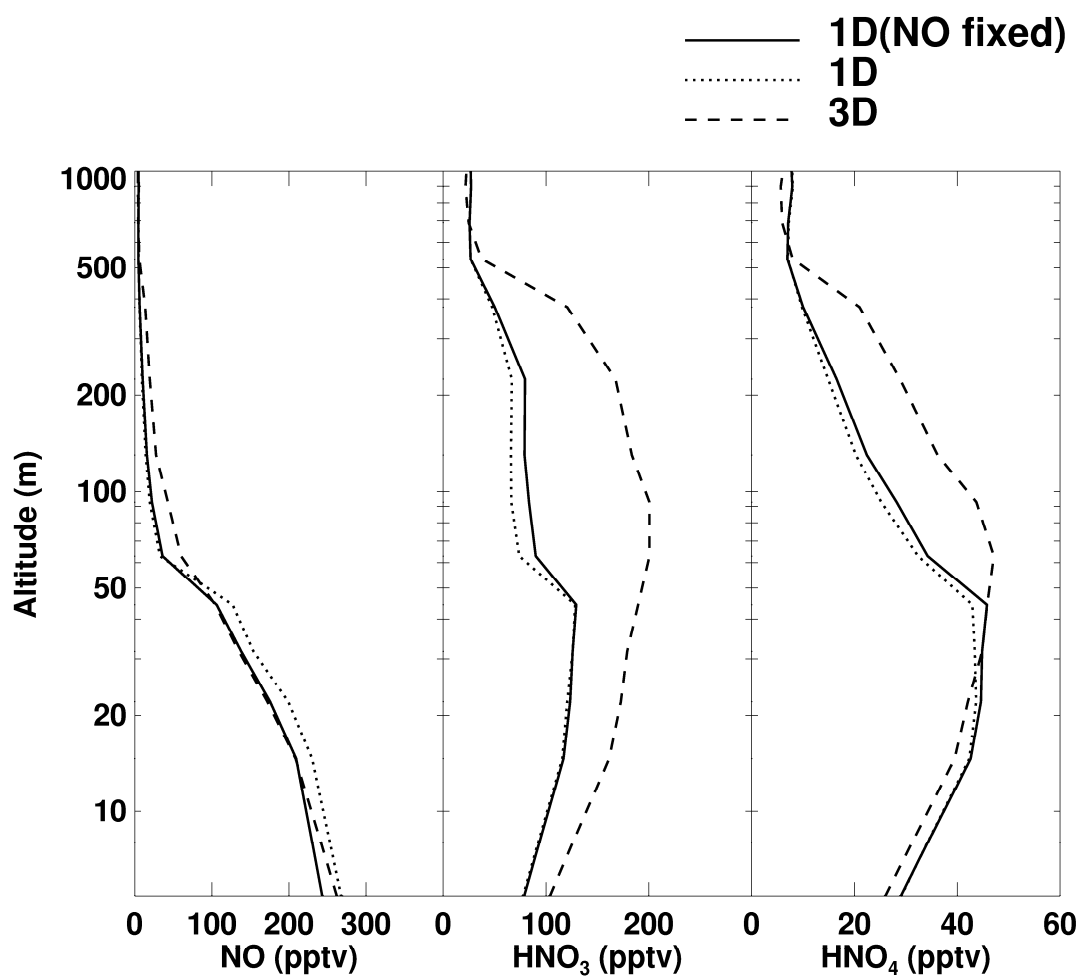


**Figure 6.8** 1-D and 3-D model-simulated mean vertical profiles of NO, HNO<sub>3</sub>, and HNO<sub>4</sub> during ANTICI 2003. In the first 1-D simulation, surface NO is specified as observed. In the second simulation, snow NO<sub>x</sub> emission parameterization is used.

Using a box model analysis of ISCAT 2000 measurements, Slusher *et al.* [2002] estimated that the lifetimes of  $\text{HNO}_3$  and  $\text{HNO}_4$  against deposition are 3.5 hours. With ANTICI data, a similar calculation results in a dry deposition lifetime of 10 hours. Slower dry deposition during ANTICI likely reflects a meteorological environment different from that of ISCAT 2000. Scaling a boundary layer depth to 50-100 m with a deposition velocity of  $0.15 \text{ cm s}^{-1}$  yields a lifetime in the range of 9 to 18 hours. We note that a simple scaling of the boundary layer height with dry deposition velocity underestimates the deposition lifetime of  $\text{HNO}_4$  because its concentrations increase by a factor of 2 in the boundary layer (Figure 6.8). Estimating dry deposition lifetimes using a box model is reasonable in a well-mixing boundary layer, but it is problematic over Antarctica because the boundary layer is frequently stable. The large vertical gradients of  $\text{HNO}_4$  and  $\text{NO}_x$ , which exhibit opposite trends, cannot be taken into account properly in a box model. Furthermore, Figure 6.7b shows that diffusion influx is as important as chemical production or deposition loss. In a shallow box near the surface, a box-model calculation would overestimate the loss by dry deposition because it accounts for both dry deposition and diffusion influx. However, the finding by Slusher *et al.* [2002] that  $\text{HNO}_4$  deposition accounts for a significant portion of nitrogen deposition to snow is still valid in our results since the deposition flux is the product of deposition velocity and trace gas concentration. The deposition velocities are the same for  $\text{HNO}_3$  and  $\text{HNO}_4$ , and their concentrations are in comparable ranges.

## **6.5 Comparison with Balloon and Aircraft NO Measurements and Assessments of Plateau Reactive Nitrogen Budget and Photochemical Impact Over Antarctica**



We extend the comparison of model-simulated reactive nitrogen with surface measurements to include the vertical distributions of NO as recorded by the tethered balloon platform at SP [Helmig *et al.*, 2007] and the Twin Otter data recorded within 400 km of SP but still over the plateau [Davis *et al.*, 2007]. For this purpose, the construction of a rather crude empirical daytime snow NO<sub>x</sub> emission parameterization (Section 3.2), without which it would be difficult to simulate the spatial variability of surface NO<sub>x</sub> over Antarctica, is critically important.

The tethered balloon was used to measure NO vertical distributions at SP on December 17-28. High NO<sub>x</sub> concentrations were measured near the surface on December 21 and 23 (Figure 6.5a); we separate these data from the periods of December 17-20 and 25-28. During the high-NO<sub>x</sub> period of December 21 and 23 (no balloon measurements were made on December 24), simulated median values at low altitudes are lower than the measurements because of the model underestimation on December 21 (Figure 6.5a). The observed and simulated means are closer. The observed decrease in NO with altitude is simulated by the models. During the low-NO<sub>x</sub> periods, the simulated median values are too low; although low bias is still evident above 60 m, the agreements among the mean values are better. The concentrations in the 3-D model are higher than those in the 1-D model due in part to the 30% higher emissions, and they are in better agreement with those in the observations.

The spatial distribution of the NO mixing ratios measured by the Twin Otter at 20-60 m above the surface on December 4-6 is shown in Figure 6.10a. From here, it can be seen that the observed NO concentrations tend to be higher at higher elevations. Such

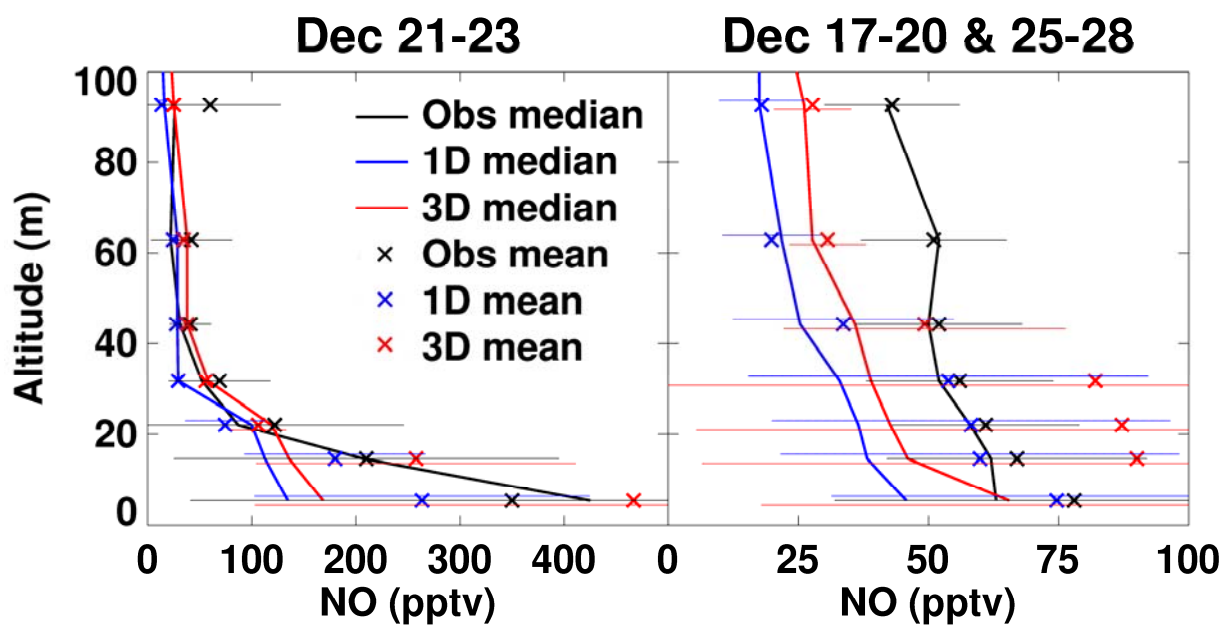


**Figure 6.9** Balloon measurements of NO profiles on December 17-28 and the corresponding model results. The horizontal bar shows the standard deviation. There are 6 profiles for December 21-23 and 21 profiles for December 17-20 and 25-28.

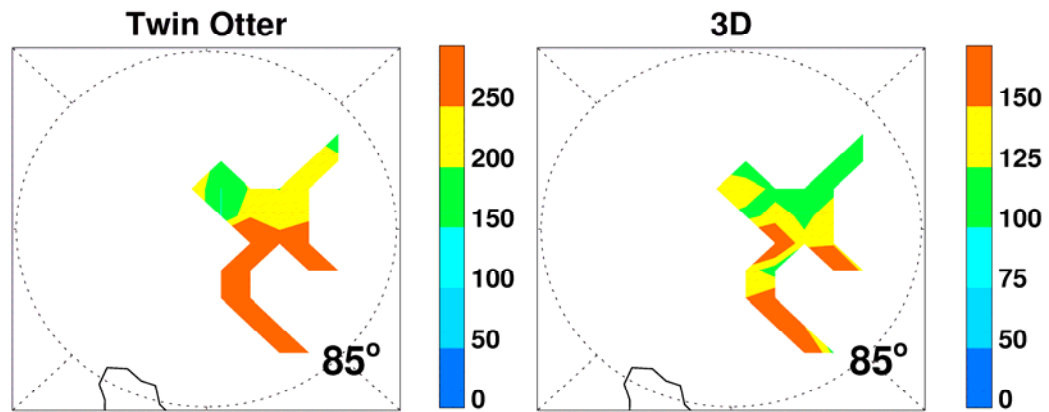


**Figure 6.10a** Twin Otter observed- and model-simulated NO mixing ratios (pptv) at 20-60 m above the surface on December 4-6. Model results are sampled along flight tracks at the time of the measurements.

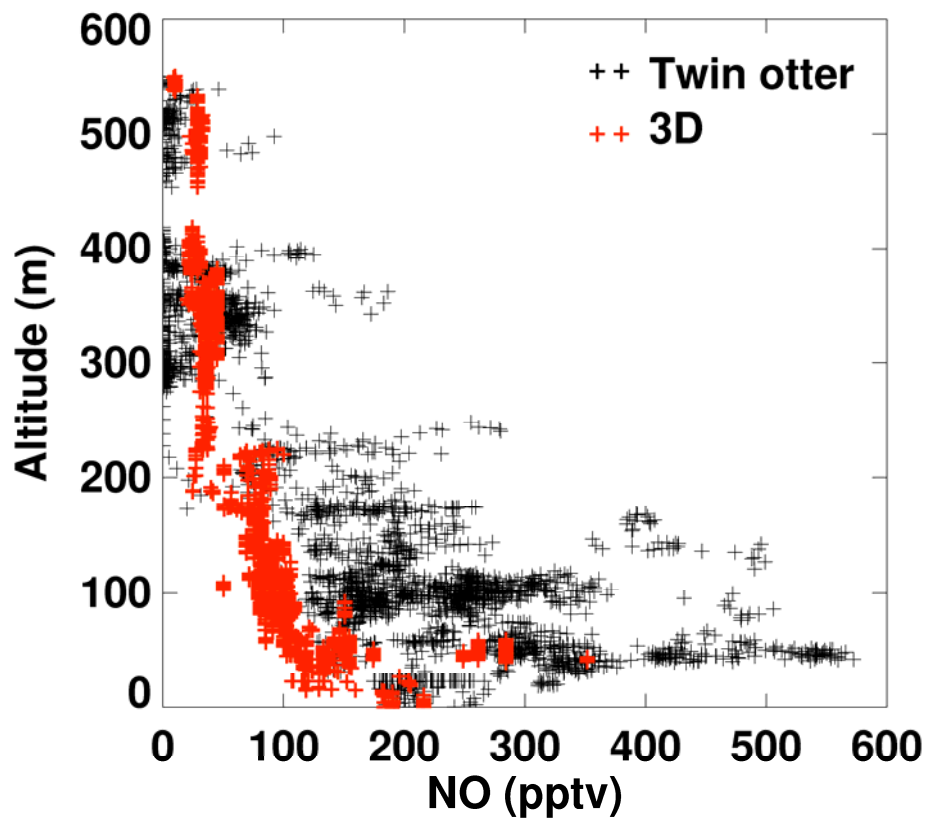


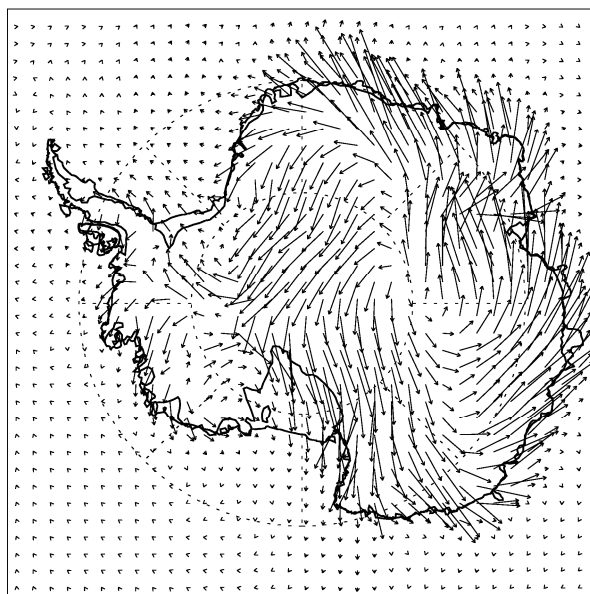
**Figure 6.10b** Twin Otter observed- and model-simulated vertical distributions of NO on December 4-6.

a spatial distribution is captured by the model simulation. However, the model has a clear low bias, which is also shown in the vertical distribution (Figure 6.10b). While the measurements show NO mixing ratios up to 550 pptv, the model results reach only 350 pptv. Surface measurements of 100-200 pptv at SP on December 4-6 are also underestimated by the 3-D model, but to a lesser extent (Figure 6.5a). Because the model-simulated variability is driven mostly by temperature (Figure 6.4), the colder temperatures at higher elevations lead to more NO<sub>x</sub> emissions and thus to higher NO concentrations. The resulting spatial gradient/variability is, however, underestimated by the model. Several important factors that contribute significantly to the spatial variability of snow NO<sub>x</sub> emissions might not be accounted for in the parameterization. An adequate evaluation of this issue necessitates more extensive spatial and temporal aircraft measurements that improve on their "representativeness" as well as detailed laboratory studies of the nitrate photochemical mechanisms.

The comparison of model simulations with the measurements from the ANTICI 2003 experiment demonstrates that the 3-D model can capture some of the essential features of airborne data. Given this level of agreement, we applied the 3-D model to explore the reactive nitrogen budget over the plateau and the photochemical impact of snow NO<sub>x</sub> emissions over the entire Antarctic continent. In general, the simulated low-altitude NO<sub>x</sub> concentrations have low bias at SP during low-NO<sub>x</sub> periods of balloon measurements and over the plateau regions sampled by Twin Otter, implying that the simulated nitrogen source and photochemical impact (in terms of OH concentrations) may have low bias.

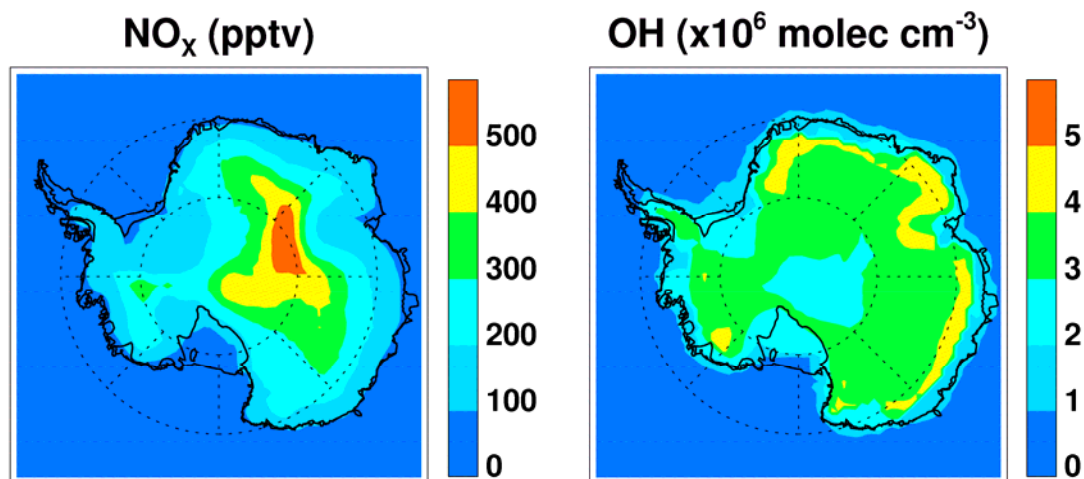
Using the 3-D model results, we construct the nitrogen budget for the plateau region (elevation above 2.5 km). For December 2003, we estimate emissions of  $0.25 \text{ kg N km}^{-2} \text{ month}^{-1}$ . The reactive nitrogen deposition flux is  $0.13 \text{ kg N km}^{-2} \text{ month}^{-1}$ . Depositions of  $\text{HNO}_3$  and  $\text{HNO}_4$  account for 73% and 21%, respectively, and the rest is largely deposition of  $\text{NO}_2$ . The net outflux of reactive nitrogen is  $0.12 \text{ kg N km}^{-2} \text{ month}^{-1}$ . About 90% of the outflux takes place within 1 km above the surface. Outfluxes of  $\text{HNO}_3$  and  $\text{NO}_x$  account for 61% and 26%, respectively, and the rest is mostly  $\text{HNO}_4$ . Figure 6.11 shows the near-surface fluxes of  $\text{HNO}_3$ . As indicated in the figure, most of the transport is over eastern Antarctica. The implications of the outflux on plateau nitrogen chemistry are discussed by Davis *et al.* [2007].

Figure 6.12 shows model-simulated surface  $\text{NO}_x$  and OH concentrations over Antarctica during the ANTICI 2003 period. The emission parameterization predicts higher  $\text{NO}_x$  emissions and thus concentrations over the eastern Antarctic plateau. The concentration of OH does not maximize in regions with the highest  $\text{NO}_x$  concentrations because of the nonlinearity of  $\text{HO}_x$  chemistry [Chen *et al.*, 2001, 2004, Davis *et al.*, 2004]. Thus, the model predicts some of the highest OH levels in the downslope drainage areas of eastern Antarctica. Predicted mean surface OH concentrations exceed  $2 \times 10^6 \text{ molec cm}^{-3}$  over most of the Antarctic continent. Using a box model having as its input the Twin Otter plateau NO data set, Davis *et al.* [2007] showed a strong vertical gradient in OH with estimated concentrations reaching as high as  $4 \times 10^6 \text{ molec cm}^{-3}$ . Based on these results, the authors hypothesized that upon consideration of the vertical NO structure across the larger plateau, it is likely that  $\text{NO}_x$  snow emissions likely lead to an oxidizing canopy that enshrouds the entire plateau. Showing a shallow canopy of high OH concentrations above



—0.004 moles m<sup>-2</sup>day<sup>-1</sup>

**Figure 6.11** Simulated monthly mean near-surface HNO<sub>3</sub> fluxes for December 2003.



**Figure 6.12** Simulated mean surface NO<sub>x</sub> and OH concentrations during ANTICI 2003.

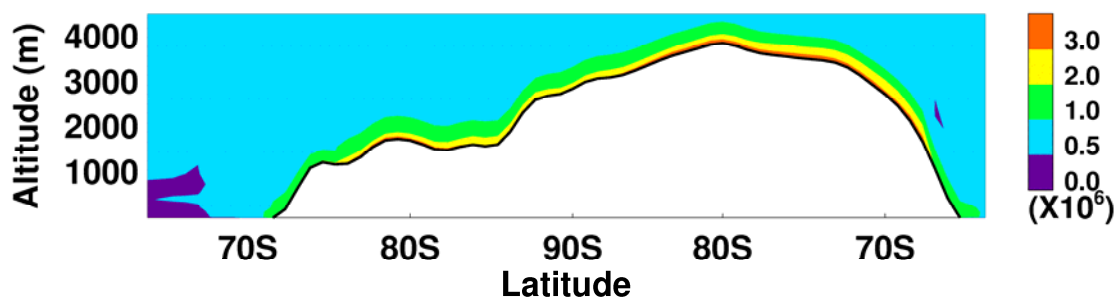


**Figure 6.13a** Simulated cross section of OH concentrations ( $10^6 \text{ molec cm}^{-3}$ ) along the  $90^\circ\text{W} - 90^\circ\text{E}$  meridian during ANTICI 2003.

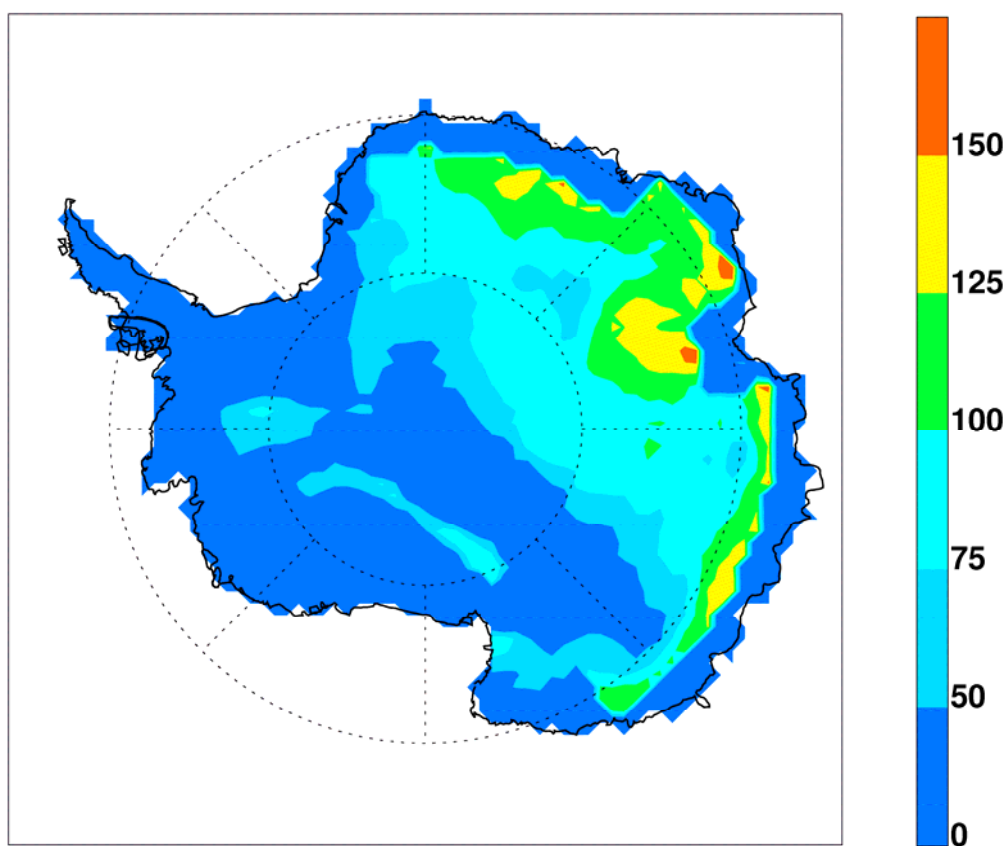


**Figure 6.13b** Simulated depth (m) of the oxidizing canopy over Antarctica ( $[\text{OH}] > 3 \times 10^6 \text{ molec cm}^{-3}$ ) during ANTICI 2003.

the Antarctic plateau driven by snow  $\text{NO}_x$  emissions, a model-simulated cross-section of the OH concentration level along the  $90^\circ\text{W}$ - $90^\circ\text{E}$  meridian (Figure 6.13a) supports their hypothesis, Figure 6.13b shows the simulated distribution of the oxidizing canopy thickness over Antarctica. For illustrative purposes, we define the highly active oxidizing canopy as the region with  $[\text{OH}] \geq 3 \times 10^6 \text{ molec cm}^{-3}$ , the highest median value found in the marine boundary layer over the tropical Pacific [Y. Wang *et al.*, 2001]. The simulated OH canopy is deeper, generally in the range of 50-150 m, over the eastern Antarctic plateau than it is over other regions. The spatial distribution of the canopy depth reflects a combination of surface  $\text{NO}_x$  emissions, boundary layer height, and transport.

## 6.6 Conclusions

We apply 1-D chemistry-diffusion and 3-D chemical transport models to analyze surface, balloon, and aircraft measurements of reactive nitrogen during ANTICI 2003. The emphasis of the model analysis is on high  $\text{NO}_x$ -emitting plateau regions. We simulate the meteorological fields using the polar version of MM5. The default ETA MYJ 2.5-order closure scheme predicts much lower boundary layer heights than SODAR measurements at SP. We decrease the minimum eddy diffusion coefficient from a default value of 0.09 to  $0.001 \text{ m}^2 \text{ s}^{-1}$  and obtain reasonable simulations of SP boundary layer heights.

Using the 1-D chemistry-diffusion model and surface measurements at SP, we derive the necessary snow  $\text{NO}_x$  emission fluxes that explain the observed NO concentrations. The average emission flux of  $3.2 \times 10^8 \text{ molec cm}^{-2} \text{ s}^{-1}$  is 20% lower than the mean flux of  $3.9 \times 10^8 \text{ molec cm}^{-2} \text{ s}^{-1}$  estimated by Oncley *et al.* (2004) using sonic anemometers, temperature sensors, and high-speed NO measurements during ISCAT



2000. We parameterize the derived daytime snow emissions as a function of temperature and wind speed. The empirical parameterization is essential for simulating the spatial variability of observed NO concentrations by Twin Otter. Vertical advection, not accounted for in the 1-D model, decreases surface NO concentrations at SP; daytime snow emissions increased 30% in the 3-D model to an average of  $4.2 \times 10^8 \text{ molec cm}^{-2} \text{ s}^{-1}$  at SP in order to reproduce the observed NO concentrations. We calculate an average dry deposition velocity of  $0.15 \text{ cm s}^{-1}$  for  $\text{HNO}_3$  and  $\text{HNO}_4$  at SP. We find reasonable agreement between observed and simulated  $\text{HNO}_3$  and  $\text{HNO}_4$  at SP.

To our knowledge, this is first 3-D chemical transport model analysis of reactive nitrogen at SP or over Antarctica in general. Meteorological fields, snow  $\text{NO}_x$  emission parameterization, and  $\text{HO}_x$  photochemistry [Chen *et al.*, 2004] all contribute to the overall uncertainties in the simulations. In particular, simulated NO concentrations are too low compared with those of the Twin Otter measurements during December 4-6. However, a longer measurement period is needed to assess whether the bias is representative. Quantifying each of these uncertainties will require much larger datasets than those currently available during ANTICI 2003, and new laboratory studies of the snow nitrate photochemical process. Below, we focus the discussion on two major implications from the model results.

First, inefficient turbulence transport in the relatively stable Antarctic boundary layer leads to large gradients in NO (> a factor of 2 change within the lowest 50 m, Figure 6.8), which implies that the vertical structure needs to be simulated if photochemistry in the region is to be understood. For the oxidation products  $\text{HNO}_3$  and  $\text{HNO}_4$ , extensive mixing up to 500 m is simulated. These 1-D vertical profiles are further

modified by 3-D transport. The vertical distribution of  $\text{HNO}_3$  is affected most. The much longer lifetime of  $\text{HNO}_3$  than  $\text{NO}_x$  or  $\text{HNO}_4$  allows for large accumulations of this species in the upper portion of the boundary layer, resulting in  $\text{HNO}_3$  concentrations near the surface that are significantly higher in the 3-D model than in the 1-D model. In order to reduce the “excess”  $\text{HNO}_3$ , the dry deposition velocity of  $\text{HNO}_3$  needs to be increased in the 3-D model. Diagnostics using 1-D models will tend to underestimate  $\text{HNO}_3$  deposition velocity. While the shape of the  $\text{NO}_x$  vertical profile is not affected by 3-D transport, snow emissions need to be increased by 30% in the 3-D model compared to 1-D model. The vertical distribution of  $\text{HNO}_4$  is also affected by 3-D transport. By definition, the flux measurements of snow emissions or deposition by the eddy correlation technique assume zero mean advection of trace gases, which is inconsistent with the prevailing downslope circulation driven by katabatic flow over Antarctica. As a result, the effect of advection needs to be taken into account in the interpretation of any eddy-correlation flux measurements.

Second, the empirical daytime snow  $\text{NO}_x$  emission parameterization based on temperature and wind speed is obviously an oversimplification of the snow emission process. A more sophisticated process-based emission model that can be coupled with 1-D and 3-D chemical transport models will require additional detailed laboratory studies and more extensive field measurements (particularly by aircraft). Despite the above-cited simplifications, the 3-D model has shown that it can capture the observed spatial variability of near-surface NO recorded on the Twin Otter even though the magnitudes are underestimated. These model results suggest that the Antarctic plateau is a major source region for  $\text{NO}_x$  and that snow  $\text{NO}_x$  production takes place through a common

mechanism. For December 2003, the model estimates an average  $\text{NO}_x$  emission flux of  $0.25 \text{ kg N km}^{-2} \text{ month}^{-1}$  over the plateau (elevation above 2.5 km). About 50% of reactive nitrogen is lost by deposition and the other 50% by transport.  $\text{HNO}_3$  and  $\text{HNO}_4$  are major deposition species (73% and 21%, respectively); nitrogen outflux is largely in the form of  $\text{HNO}_3$  and  $\text{NO}_x$  (61% and 26%, respectively). At the simulated  $\text{NO}_x$  levels, most of the Antarctic continent during ANTICI 2003 has near-surface mean OH concentrations of  $> 2 \times 10^6 \text{ molec cm}^{-3}$ . The depth of the layer with  $[\text{OH}] > 3 \times 10^6 \text{ molec cm}^{-3}$  is estimated to be 50-150 m over the plateau. This result shows a highly photochemically active oxidizing canopy enshrouding the entire Antarctic plateau, which was previously hypothesized by Davis *et al.* [2004].

## **CHAPTER VII**

### **CONCLUSIONS**

Column observations of NO<sub>2</sub> by GOME and CO by MOPITT over North America and surrounding oceans for April 2000 are analyzed using the Regional chEmical trAnsport Model (REAM). Transient enhancements in these measurements due to lightning NO<sub>x</sub> production or convective transport are examined. The analyses produce clear evidence for lightning enhancements of NO<sub>2</sub> over the continent and western North Atlantic and for convective transport enhancements of CO over the ocean. Two independent satellite measurements show consistent enhancements related to convective events. Results of the model suggest that the enhancements are particularly large in the lower troposphere due to convective downdrafts of lightning NO<sub>x</sub> and shallow convection of CO, implying that low-altitude aircraft in situ observations are potentially critical for evaluating the model simulations and validating the satellite observations of these transient features.

The 3-D REAM is used to simulate trace gas from February to May 2000 over North America. Once applied, the simulations result in an analysis of surface, aircraft, and satellite measurements that explain the springtime transitions of key trace gas concentrations and export. The global GEOS-CHEM model is used to provide chemical initial and boundary conditions. Surface observations from EPA AIRNow and SEARCH networks, aircraft observations from the TOPSE and MOZAIC experiments, ozonesondes, and remote sensing measurements from GOME, MOPITT, TOMS and SAGE II are then analyzed. Generally, the model results are in good agreement with the observations in the

troposphere. REAM is also used to simulate decreases in surface CO and NO<sub>x</sub> concentrations and MOPITT CO columns from spring to summer. Results show that the seasonal change of the GOME NO<sub>2</sub> tropospheric column is not as large as that of the CO column because of increasing lightning and soil NO<sub>x</sub> emissions. Differences between simulated and GOME NO<sub>2</sub> columns on a monthly mean basis are averaged over the four-month period. Results show that the total NO<sub>x</sub> emissions derived from the inversion of the GOME NO<sub>2</sub> column are in good agreement with those of the model a priori inventory. In addition, although REAM has a low bias (above 350 hPa) due to specified upper boundary concentrations, REAM-simulated surface ozone concentrations are in good agreement with AIRNow measurements. By comparison, GEOS-CHEM-simulated surface ozone concentrations show a much faster increasing trend. We find that the simulated boundary layer structure is a key process that differentiates the REAM results from GEOS-CHEM. The MM5-simulated mixing layer heights used in REAM are lower than those used in GEOS-CHEM. As a result, the activation of photochemistry in the boundary layer is much faster in GEOS-CHEM than it is in REAM. REAM results also indicate that the main contributor of the significant increase in the tropospheric ozone column over the western North Atlantic is lightning NO<sub>x</sub> production. The impact of lightning is also evident in model-simulated pollutant exports.

The tropospheric O<sub>3</sub> column retrieved from OMI and MLS measurements, the NO<sub>2</sub> column from OMI measurements, and the upper tropospheric O<sub>3</sub> and CO concentrations from TES over North America and the western North Atlantic from April to August 2005 are analyzed using REAM. The satellite measurements and REAM simulations showed large enhancements of column and upper tropospheric O<sub>3</sub> over the

western North Atlantic comparable to those over the eastern United States. These measurements show that the O<sub>3</sub> enhancement region migrates northward from spring to summer. An analysis of the model indicates that the northward shift is driven by O<sub>3</sub> in the stratospheric flux, convective outflow and production from lightning NO<sub>x</sub>. As their uncertainties improve, the satellite measurements of O<sub>3</sub> and its precursors will provide more quantitative constraints on pollutant outflow from the continents.

The observations during the TOPSE experiment show large enhancements of NO<sub>x</sub>, PAN, O<sub>3</sub>, CO, CFCs, and Halon-1211 in the upper troposphere over North America in the late spring. Analyses of these observations and model results indicate that the enhancements are most likely driven by a surge of trans-Pacific pollutant transport during the late spring. The rapid seasonal transition is particularly striking for upper tropospheric NO<sub>x</sub>, resulting in large increases in photochemical oxidation and O<sub>3</sub> production during the period. The transition occurs later in the season than that of low-altitude trans-Pacific transport, which peaks in March and April. The current generation of global chemical transport models clearly underestimates this long-range transport of pollutants, implying that the model-projected impact on regional air quality over North America has been underestimated (through subsidence).

The results of surface and aircraft measurements reveal a large amount of reactive nitrogen tracers over the Antarctic plateau in the summer. These measurements are then subjected to the 1-D CTM and REAM for the purpose of assessing the photochemical impact of snow NO<sub>x</sub> emissions. Then, after slightly modifying the ETA turbulence scheme, we simulated the boundary layer heights, measured by SODAR at SP, reasonably well with the polar version of MM5. Results show that the average level of

model-derived snow  $\text{NO}_x$  emissions ( $3.2\text{--}4.2 \times 10^8 \text{ molec cm}^{-2} \text{ s}^{-1}$ ) at SP is similar to the measured flux of  $3.9 \times 10^8 \text{ molec cm}^{-2} \text{ s}^{-1}$  during ISCAT 2000. Daytime snow  $\text{NO}_x$  emissions are parameterized as a function of temperature and wind speed. Surface measurements of NO,  $\text{HNO}_3$ , and  $\text{HNO}_4$ , and balloon measurements of NO at the South Pole are reasonably simulated by 1-D CTM and REAM. Compared with the Twin Otter measurements of NO over the plateau regions, REAM-simulated NO concentrations are at the low end, which indicates that either the parameterization based on surface measurements at SP underestimates emissions at higher-elevation plateau regions or the limited aircraft database may not totally represent the season of the year sampled. However, the model captures the spatial variability of near-surface NO measured by aircraft to a large extent, indicating that snow  $\text{NO}_x$  emissions are produced through a common mechanism. An average emission flux of  $0.25 \text{ kg N km}^{-2} \text{ month}^{-1}$  is calculated for December 2003 over the plateau (with an elevation above 2.5 km). Deposition is responsible for the loss of about half of reactive nitrogen, and scavenging by transport the other half. The REAM results show that snow  $\text{NO}_x$  emissions are responsible for a shallow but highly photochemically active oxidizing “canopy” enshrouding the entire Antarctic plateau.

## REFERENCES

- Allen, D. J., and K. E. Pickering, Evaluation of lightning flash rate parameterizations for use in a global chemical transport model, *J. Geophys. Res.*, 107(D23), 4711, doi:10.1029/2002JD002066, 2002.
- Allen, D., *et al.*, A three-dimensional total odd nitrogen ( $\text{NO}_y$ ) simulation during SONEX using a stretched-grid chemical transport model, *J. Geophys. Res.*, 105(D3), 3851-3876, 2000.
- Allen, D., *et al.*, Evaluation of pollutant outflow and CO sources during TRACE-P using model-calculated, aircraft-based, and Measurements of Pollution in the Troposphere (MOPITT)-derived CO concentrations, *J. Geophys. Res.*, 109, D15S03, 10.1029/2003JD004250, 2004.
- Andreae, M.O., H. Berresheim, T.W., Andreae, M.A. Kritz, T.S. Bates, and J.T. Merrill, Vertical distribution of dimethylsulfide, sulfur dioxide, aerosol ions, and radon over the northeast Pacific Ocean, *J. Atmos. Chem.*, 6, 149–173, 1988.
- Arellano, A. F., *et al.*, Top-down estimates of global CO sources using MOPITT measurements, *Geophys. Res. Lett.*, 31, L01104, doi:01110.01029/02003GL018609, 2004.
- Atlas, E. L., B. A. Ridley, and C. Cantrell, The Tropospheric Ozone Production about the Spring Equinox (TOPSE) Experiment: Introduction, *J. Geophys. Res.*, 108, 8353, doi:10.1029/2002JD003172, 2003.
- Beirle, S., *et al.*, Estimating the  $\text{NO}_x$  produced by lightning from GOME and NLDN data: a case study in the Gulf of Mexico, *Atmos. Chem. Phys.*, 6, 1075-1089, 2006.
- Beirle, S., *et al.*,  $\text{NO}_x$  production by lightning estimated with GOME, *Adv. Space Res.*, 34, 793-797, 2004.
- Benkovitz, C.M., M.T. Schultz, J. Pacyna, L. Tarrason, J. Dignon, E.C. Voldner, P.A. Sprro, J.A. Logan, and T.E. Graedel, Global gridded inventories for anthropogenic emissions of sulfur and nitrogen, *J. Geophys. Res.*, 101, 29239-29253, 1996.
- Berman, S., *et al.*, Spatial and temporal variation in the mixing depth over the Northeastern United States during the Summer of 1995, *J. Appl. Meteo.*, 38, 1661-1673, 1999.
- Berntsen, T. K., S. Karlsdottir, and D.A. Jaffe, Influence of Asian emissions on the composition of air reaching the northwestern United States, *Geophys. Res. Lett.*, 26, 2171-2174, 1999.
- Bertram, T. H., *et al.*, Satellite measurements of daily variations in soil  $\text{NO}_x$  emissions,



*Geophys. Res. Lett.*, 32, L24812, doi:24810.21029/22005GL024640, 2005.

Bertram, T. H., *et al.*, Direct Measurements of the Convective Recycling of the upper Troposphere, *Science*, 315, 816-820, 2007.

Bey I., D. J. Jacob, R. M. Yantosca, J. A. Logan, B. Field, A. M. Fiore, Q. Li, H. Liu, L. J. Mickley, and M. Schultz, Global modeling of tropospheric chemistry with assimilated meteorology: Model description and evaluation, *J. Geophys. Res.*, 106, 23073-23096, 2001.

Bithell, M., L. J. Gray, and B. D. Cox, Three-dimensional view of the evolution of midlatitude stratospheric intrusions, *J. Atmos. Sci.*, 56, 673-688, 1999.

Black, T. L., The new NMC mesoscale ETA model: Description and forecast examples, *Weather and Forecasting*, 9, 265-278, 1994.

Blackadar, A. K., Modeling pollutant transfer during daytime convection. Proc. Fourth Symp., On Atmospheric Turbulence, Diffusion, and Air Quality, Reno, *Amer. Meteo. Soc.*, 443-447, 1978.

Blake, N. J., *et al.*, The seasonal evolution of NMHCs and light alkyl nitrates at middle to high northern latitudes during TOPSE, *J. Geophys. Res.*, 108, 8359, doi:10.1029/2001JD001467, 2003.

Boersma, K. F., *et al.*, Estimates of lightning NO<sub>x</sub> production from GOME satellite observations, *Atmos. Chem. Phys.*, 5, 2311-2331, 2005.

Bonan, G. B., *et al.*, Landscapes as patches of plant functional types: An integrating concept for climate and ecosystem models, *Global Biogeo. Cyc.*, 16(2), 1021, doi:10.1029/2000GB001360, 2002.

Bond, D. W., *et al.*, NO<sub>x</sub> production by lightning over the continental United States, *J. Geophys. Res.*, 106(D21), 22701-22710, 2001.

Brasseur, G. P., *et al.*, MOZART, A global chemical transport model for ozone and related chemical tracers 1 - model description, *J. Geophys. Res.*, 103, 28265-28289, 1998.

Bromwich, D.H., J.J. Cassano, T. Klein, G. Heinemann, K. M. Hines, K. Steffen, and J. E. Box, Mesoscale Modeling of Katabatic Winds over Greenland with the Polar MM5, *Monthly Weather Rev.*, 129, 2290-2309, 2001.

Browell, E. *et al.*, Ozone, aerosol, potential vorticity, and trace gas trends observed at high latitudes from February to May 200, *J. Geophys. Res.*, 108, 8369, doi:10.1029/2001JD001390, 2003.

Brune, W. H., *et al.*, OH and HO<sub>2</sub> chemistry in the North Atlantic free troposphere, *Geophys. Res. Lett.*, 26, 3077-3080, 1999.

Cantrell, C. A., *et al.*, Steady state free radical budgets and ozone photochemistry during TOPSE, *J. Geophys. Res.*, 108, 8361, doi:10.1029/2002JD002198, 2003.

Cassano, J. J., J. E. Box, D. H. Bromwich, L. Li, and K. Steffen, Evaluation of polar MM5 simulations of Greenland's atmospheric circulation, *J. Geophys. Res.*, 106, 33867-33889, 2001.

Chance, K., *et al.*, Satellite observations of formaldehyde over North America from GOME, *Geophys. Res. Lett.*, 27, 3461-3464, 2000.

Chandra, S., *et al.*, Elevated ozone in the troposphere over the Atlantic and Pacific Oceans in the Northern Hemisphere, *Geophys. Res. Lett.*, 31, L23102, doi:10.1029/2004GL020821, 2004.

Chandra, S., *et al.*, Tropospheric ozone at tropical and middle latitudes derived from TOMS/MLS residual: Comparison with a global model, *J. Geophys. Res.*, 108(D9), 4291, doi:10.1029/2002JD002912, 2003.

Chen, G., D. Davis, J. Crawford, J.B. Nowak, F. Eisele, R.L. Mauldin, D. Tanner, M. Buhr, R. Shetter, B. Lefer, R. Arimoto, A. Hogan, and D. Blake, An investigation of South Pole HO<sub>x</sub> chemistry: Comparison of model results with ISCAT observations, *Geophys. Res. Lett.*, 28 (19), 3633-3636, 2001.

Chen, G., D. Davis, J. Crawford, L.M. Hutterli, L.G. Huey, D. Slusher, L. Mauldin, F. Eisele, D. Tanner, J. Dibb, M. Buhr, J. McConnell, B. Lefer, R. Shetter, D. Blake, C.H. Song, K. Lombardi, and J. Arnoldy, A reassessment of HO<sub>x</sub> South Pole chemistry based on observations recorded during ISCAT 2000, *Atmos. Env.*, 38 (32), 5451-5461, 2004.

Chin, M., D. J. Jacob, G.M. Gardner, M.S. Foreman-Fowler, P.A. Spiro, and D.L. Savoie, A global three-dimensional model of tropospheric sulfate, *J. Geophys. Res.*, 101, 18667-18690, 1996.

Chin, M., *et al.*, Tropospheric aerosol optical thickness from the GOCART model and comparisons with satellite and sunphotometer measurements, *J. Atmos. Sci.*, 59, 461-483, 2002.

Choi, Y., Y. Wang, T. Zeng, R. Martin, T. Kurosu, and K. Chance, Evidence of lightning NO<sub>x</sub> and convective transport of pollutants in satellite observations over North America, *Geophys. Res. Lett.*, 32, L02805, doi:10.1029/2004GL021436, 2005.

Choi, Y., *et al.*, Modeling analysis of springtime transition of NO<sub>2</sub>, CO and O<sub>3</sub> over North America on the basis of in situ and satellite measurements, will be submitted to *J. Geophys. Res.*, 2007a.

Choi, Y., *et al.*, Evidence of spring-summer northward migration of high O<sub>3</sub> over the western North Atlantic, will be submitted to *Geophys. Res. Lett.*, 2007b.

Cooper, O., *et al.*, Trace gas composition of midlatitude cyclones over the western North Atlantic Ocean: A conceptual model, *J. Geophys. Res.*, 107(D7), 4056, doi:10.1029/2001JD000901, 2002a.

Cooper, O., *et al.*, Trace gas composition of mid-latitude cyclones over the western North Atlantic Ocean: A seasonal comparison of ozone and CO, *J. Geophys. Res.*, 107(D7), 4057, doi:10.1029/2001JD000902, 2002b.

Cooper, O. R., *et al.*, A springtime comparison of tropospheric ozone and transport pathways on the east and west coasts of the United States, *J. Geophys. Res.*, 110, D05S90, doi:10.1029/2004JD005183, 2005.

Cooper, O. R., *et al.*, Larger upper tropospheric ozone enhancements above midlatitude North America during summer: In situ evidence from the IONS and MOZAIC ozone measurement network, *J. Geophys. Res.*, 111, D24S05, doi:10.1029/2006JD007306, 2006.

Crawford, J. H., *et al.*, Evolution and chemical consequences of lightning-produced NO<sub>x</sub> observed in the North Atlantic upper troposphere, *J. Geophys. Res.*, 105(D15), 19795-19809, 2000.

Crawford, J. H., *et al.*, Relationship between Measurements of Pollution in the Troposphere (MOPITT) and in situ observations of CO based on a large-scale feature sampled during TRACE-P, *J. Geophys. Res.*, 109, D15S04, doi:10.1029/2003JD004308, 2004.

Crawford, J. H., D. D. Davis, G. Chen, M. Buhr, S. Oltmans, R. Weller, L. Mauldin, F. Eisele, R. Shetter, B. Lefer, R. Arimoto, and A. Hogan, Evidence for photochemical production of ozone at the South Pole surface, *Geophys. Res. Lett.*, 28 (19), 3641-3644, 2001.

Cummins, K. L., *et al.*, A combined TOA/MDF Technology Upgrade of the U.S. National Lightning Detection Network, *J. Geophys. Res.*, 103(D8), 9035-9044, 1998.

Davis, D. D., *et al.*, An assessment of western North Pacific ozone photochemistry based on springtime observations from NASA's PEM-West B (1994) and TRACE-P (2001) field studies, *J. Geophys. Res.*, 108, 8829, doi:10.1029/2002JD003232, 2003.

Davis, D. D., J. Crawford, G. Chen, Y. Wang, M. Buhr, D. Helmig, D. Blake, W. Neff, and F. Eisele, New Antarctic study reveals an atmospheric environment over the plateau chemically unlike any other polar site, submitted to *Atmos. Env.*, 2007.

Davis, D., G. Chen, M. Buhr, J. Crawford, D. Lenschow, B. Lefer, R. Shetter, F. Eisele, L. Mauldin, and A. Hogan, South Pole NO<sub>x</sub> chemistry: an assessment of factors controlling variability and absolute levels, *Atmos. Env.*, 38 (32), 5375-5388, 2004.

Davis, D., J.B. Nowak, G. Chen, M. Buhr, R. Arimoto, A. Hogan, F. Eisele, L. Mauldin, D. Tanner, R. Shetter, B. Lefer, and P. McMurry, Unexpected high levels of NO observed at South Pole, *Geophys. Res. Lett.*, 28 (19), 3625-3628, 2001.

DeCaria, A. J., *et al.*, A cloud-scale model study of lightning-generated NO<sub>x</sub> in an individual thunderstorm during STERAO-A, *J. Geophys. Res.*, 105(D9), 11601-11616, 2000.

Deeter, M. N., *et al.*, Evaluation of operational radiances for the Measurements of Pollution in the Troposphere (MOPITT) instrument CO thermal band channels, *J. Geophys. Res.*, 109, D03308, doi:03310.01029/02003JD003970, 2004b.

Deeter, M. N., *et al.*, Operational carbon monoxide retrieval algorithm and selected results for the MOPITT instrument, *J. Geophys. Res.*, 108(D14), 4399, doi:/4310.1029/2002JD003186, 2003.

Deeter, M. N., *et al.*, Vertical resolution and information content of CO profiles retrieved by MOPITT, *Geophys. Res. Lett.*, 31, L15112, doi:15110.11029/12004GL020235, 2004a.

Dickerson, R. R., *et al.*, Thunderstorms: An important mechanism in the transport of air pollutants, *Science*, 235, 460-465, 1987.

Edwards, D. P., *et al.*, Tropospheric ozone over the tropical Atlantic: A satellite perspective, *J. Geophys. Res.*, 108(D8), 4237, doi:4210.1029/2002JD002927, 2003.

Eisele, F. L., *et al.*, Understanding the Production and Interconversion of the Hydroxyl Radical during the Tropospheric OH Photochemistry Experiment, *J. Geophys. Res.*, 102, 6457-6465, 1997.

Eisele, F., *et al.*, An overview of ANTICI 2003, submitted to *Atmos. Env.*, 2007.

Emmons, L. K., *et al.*, Budget of tropospheric ozone during TOPSE from two chemical transport models, *J. Geophys. Res.*, 108, 8372, doi:10.1029/2002JD002665, 2003.

Emmons, L. K., *et al.*, Validation of MOPITT CO retrievals with aircraft in situ profiles, *J. Geophys. Res.*, 109, D03309, doi:03310.01029/02003JD004101, 2004.

Emmons, L., *et al.*, Budget of tropospheric ozone during TOPSE from two chemical transport models, *J. Geophys. Res.*, 108, 8372, doi:10.1029/2002JD002665, 2003.

EPA, National air quality and emissions trends report, 1980, 1985, 1989-2000, U. S., Environmental Protection Agency, Research Triangle Park, NC 27111, 2003.

Fehr, T., *et al.*, Model study on production and transport of lightning-produced NO<sub>x</sub> in a EULINOX supercell storm, *J. Geophys. Res.*, 109, D09102, doi:10.1029/2003JD003935, 2004.

Finlayson, B. J., and J. N. Pitts, Chemistry of the upper and lower atmosphere, Academic press, 1999.

Fiore, A. M., *et al.*, Long-term trends in ground level ozone over the contiguous United States, *J. Geophys. Res.*, 103(D1), 1471-1480, 1998.

Fisherman, J., and J. C. Larsen, Distribution of total ozone and stratospheric ozone in the tropics: Implications for the distribution of tropospheric ozone, *J. Geophys. Res.*, 92, 6627-6634, 1987.

Fisherman, J., *et al.*, Distribution of tropospheric ozone determined from satellite data, *J. Geophys. Res.*, 95(D4), 3599-3617, 1990.

Fox-Rabinovitz, M. S., L. L. Takacs, and R. C. Govindaraju, A variable-resolution stretched-grid general circulation model and data assimilation system with multiple areas of interest: Studying anomalous regional climate events of 1998, *J. Geophys. Res.*, 107(D24), 4768, doi:10.1029/2002JD002177, 2002.

Frost, G. J., *et al.*, Effects of changing power plant NO<sub>x</sub> emissions on ozone in the eastern United States: Proof of concept, *J. Geophys. Res.*, 111, D12306, doi:10.1029/2005JD006354, 2006.

Geleyn, J. F., Some diagnostics of the cloud/radiation interaction in the ECMWF forecast model. In: Proceedings of Workshop on Radiation and Cloud-Radiation Interaction in Numerical Modeling, pp. 135-162, 1981.

Gierczak, T., E. Jimenez, V. Riffault, J. B. Burkholder, and A. R. Ravishankara, Thermal decomposition of HO<sub>2</sub>NO<sub>2</sub> (peroxynitric acid, PNA): Rate coefficient and determination of the enthalpy of formation, *J. Phys. Chem. A*, 109, 586-596, 2005.

Giorgi, F., and W.L. Chameides, Rainout lifetimes of highly soluble aerosols and gases as inferred from simulation with a general circulation model, *J. Geophys. Res.*, 91, 14367-14376, 1986.

Grell, G. A., Prognostic evaluation of assumptions used by cumulus parameterizations, *Mon. Weather Rev.*, 121, 764-787, 1993.

Guenther, *et al.*, A global model of natural volatile organic compound emissions, *J. Geophys. Res.*, 100, 8873-8892, 1995.

Heald, C. L., *et al.*, Asian outflow and trans-Pacific transport of carbon monoxide and

ozone pollution: An integrated satellite, aircraft, and model perspective, *J. Geophys. Res.*, 108(D24), 4804, doi:4810.1029/2003JD003507, 2003.

Heald, C.L., *et al.*, Comparative inverse analysis of satellite (MOPITT) and aircraft (TRACE-P) observations to estimate Asian sources of carbon monoxide, *J. Geophys. Res.*, 109, doi:10.1029/2004JD005185, 2004.

Helmig, D., *et al.*, Nitric oxide in the boundary-layer at South Pole during the Antarctic Tropospheric Chemistry Investigation (ANTCI), submitted to *Atmos. Env.*, 2007.

Herman, J. R., and E. A. Celarier, Earth surface reflectivity climatology at 340-380 nm from TOMS data, *J. Geophys. Res.*, 102, 28003-28011, 1997.

Hess, P. G., S. Flocke, J.-F. Lamarque, M. C. Barth, and S. Madronich, Episodic modeling of the chemical structure of the troposphere as revealed during the spring MLOPEX 2 intensive, *J. Geophys. Res.*, 105, 26809–26840, 2000.

Hess, P. G., A comparison of two paradigms: The relative global roles of moist convective versus nonconvective transport, *J. Geophys. Res.*, 110, D20302, doi:10.1029/2004JD005456, 2005.

Holton, J. R., An introduction to Dynamic meteorology, Academic press, 1992.

Holzworth, G. C., Estimates of mean maximum mixing depths in the contiguous United States, *Mon. Weather Rev.*, 92, 235-242, 1964.

Holzworth, G. C., Mixing Depths, Wind Speeds and Air Pollution Potential for Selected Locations in the United States, *J. Appl. Meteo.*, 6, 1039-1044, 1967.

Honrath, R.E., M.C. Peterson, S. Guo, J.E. Dibb, P.B. Shepson, and B. Campbell, Evidence of NO<sub>x</sub> production within or upon ice particles in the Greenland snowpack, *Geophys. Res. Lett.*, 26 (6), 695-698, 1999.

Horowitz, L. W., *et al.*, A global simulation of tropospheric ozone and related tracers: Description and evaluation of MOZART, version 2, *J. Geophys. Res.*, 108, 4784, doi:10.1029/2002JD002853, 2003.

Horowitz, L. W., *et al.*, Export of reactive nitrogen from North America during summertime: Sensitivity to hydrocarbon chemistry, *J. Geophys. Res.*, 103, 13451-13476, 1998.

Hudman, R. C., *et al.*, Ozone production in transpacific Asian pollution plumes and implications for ozone air quality in California, *J. Geophys. Res.*, 109, D23S10, doi:10.1029/2004JD004974, 2004.

Hudman, R. C., *et al.*, Surface and lightning sources of nitrogen oxides over the United

States: Magnitudes, chemical evolution, and outflow, *J. Geophys. Res.*, 112, doi:10.1029/2006JD007912, 2007.

Huey, L. G., *et al.*, CIMS measurements of HNO<sub>3</sub> and SO<sub>2</sub> at the South Pole during ISCAT 2000, *Atmos. Env.*, 38, 5411-5421, 2004.

Hutterli, M.A., J.R. McConnell, G. Chen, R.C. Bales, D.D. Davis, and D.H. Lenschow, Formaldehyde and hydrogen peroxide in air, snow and interstitial air at South Pole, *Atmos. Env.*, 38 (32), 5439-5450, 2004.

IPCC, Atmospheric chemistry and greenhouse gases, in Climate Change: The scientific Basis. The IPCC Working Group 1 Third Assessment Report., Cambridge Univ. Press, New York, 2001.

Jacob, D. J., *et al.*, Effect of rising Asian emissions on surface ozone in the United States, *Geophys. Res. Lett.*, 26, 2175-2178, 1999.

Jacob, D. J., *et al.*, Factors regulating ozone over the United States and its export to the global atmosphere, *J. Geophys. Res.*, 98, 14817-14826, 1993.

Jacob, D. J., J. A. Logan, and P. P. Murti, Effect of rising Asian emissions on surface ozone in the United States, *Geophys. Res. Lett.*, 26, 2175-2178, 1999.

Jacobson, M. Z., Fundamentals of Atmospheric modeling, Cambridge University Press, 1999.

Jacob, D.J., B.D. Field, E.M. Jin, I. Bey, Q. Li, J.A. Logan, and R.M. Yantosca, Atmospheric budget of acetone, *J. Geophys. Res.*, 107(D10), 10.1029/2001JD000694, 2002.

Jacobson, M. Z., and R.P. Turco, SMVGEAR: a sparse-matrix, vectorized Gear code for atmospheric models, *Atmos. Env.*, 28, 273-284, 1994.

Jaegle, L., *et al.*, Sources and chemistry of NO<sub>x</sub> in the upper troposphere over the United States, *Geophys. Res. Lett.*, 25, 1705-1708, 1998.

Jaegle, L., *et al.*, Ozone production in the upper troposphere and the influence of aircraft during SONEX: Approach of NO<sub>x</sub>-saturated conditions, *Geophys. Res. Lett.*, 26, 3081-3084, 1999.

Jaegle, L., *et al.*, Satellite mapping of rain-induced nitric oxide emissions from soils, *J. Geophys. Res.*, 109, D21310, doi:10.1029/2004JD004787, 2004.

Jaegle, L., *et al.*, Global partitioning of NO<sub>x</sub> sources using satellite observations: Relative roles of fossil fuel combustion, biomass burning and soil emissions, *Faraday Discuss.*, 130, 407-423, 2005.

Jaffe, D. A., I. McKendry, T. Anderson, and H. Price, Six 'new' episodes of trans-Pacific transport of air pollutants, *Atmos. Env.*, 37, 391–404, 2003.

Jaffe, D., *et al.*, Transport of Asian air pollution to North America, *Geophys. Res. Lett.*, 26, 711-714, 1999.

Jing, P., D. Cunnold, Y. Choi, and Y. Wang, Summertime tropospheric ozone columns from Aura OMI-MLS measurements versus regional model results over the United States, *Geophys. Res. Lett.*, 33, L17817, doi:10.1029/2006GL026473, 2006.

Jing, P., *et al.*, Isentropic cross-tropopause ozone transport in the Northern Hemisphere, *J. Atmos. Sci.*, 61, 1068-1078, 2004.

Jones, A.E., R. Weller, E.W. Wolff, and H.W. Jacobi, Speciation and rate of photochemical NO and NO<sub>2</sub> production in Antarctic snow, *Geophys. Res. Lett.*, 27 (3), 345-348, 2000.

Jones, A.E., R. Weller, P.S. Anderson, H.W. Jacobi, E.W. Wolff, O. Schrems, and H. Miller, Measurements of NO<sub>x</sub> emissions from the Antarctic snowpack, *Geophys. Res. Lett.*, 28 (8), 1499-1502, 2001.

Kar, J., *et al.*, Evidence of vertical transport of carbon monoxide from Measurements of Pollution in the Troposphere (MOPITT), *Geophys. Res. Lett.*, 31, L23105, doi:10.1029/2004GL021128, 2004.

Kiley, C. M., and Fuelberg, H. E., An examination of summertime cyclone transport processes during Intercontinental Chemical Transport Experiment (INTEX-A), *J. Geophys. Res.*, 111, doi:10.1029/2006JD007115, 2006.

Kim, *et al.*, Satellite-observed U.S. power plant NO<sub>x</sub> emission reductions and their impact on air quality, *Geophys. Res. Lett.*, 33, L22812, doi:10.1029/2006GL027749, 2006.

Komhyr, W. D., *et al.*, Electrochemical concentration cell ozonesonde performance evaluating during STOIC 1989, *J. Geophys. Res.*, 100, 9231-9244, 1995.

Kondo, Y., *et al.*, Photochemistry of ozone over the western Pacific from winter to spring, *J. Geophys. Res.*, 109(D23), doi:10.1029/2004JD004871, 2004.

Kreutz, K. J., and P. A. Mayewske, Spatial variability of Antarctic surface snow glaciochemistry: Implications for palaeoatmospheric circulation reconstructions, *Antarctic Science*, 11, 105-118, 1999.



Kritz, M. A., J.-C. Le Roulley, and E. F. Danielsen, The China Clipper - Fast advective transport of radon-rich air from the Asian boundary layer to the upper troposphere near California, *Tellus*, 42B, 46-61, 1990.

Kurosu, T. P., *et al.*, CRAG: Cloud Retrieval Algorithm for the European Space Agency's Global Ozone Monitoring Experiment, in Proceedings of the European Symposium of Atmospheric Measurements From Space, pp. 513-521, Eur. Space Agency, Paris, 1999.

Lacis, A. A., *et al.*, Radiative forcing of climate by changes in the vertical distribution of ozone, *J. Geophys. Res.*, 95, 9971-9981, 1990.

Lamarque, J.-F., *et al.*, Identification of CO plumes from MOPITT data: Application to the August 2000 Idaho-Montana forest fires, *Geophys. Res. Lett.*, 30(13), 1688, doi:10.1029/2003GL017503, 2003.

Lamarque, J.-F., *et al.*, Three-dimensional study of the relative contributions of the different nitrogen sources in the troposphere, *J. Geophys. Res.*, 101, 22,955-22,968, 1996.

Lauer, A., *et al.*, Tropospheric NO<sub>2</sub> columns: a comparison between model and retrieved data from GOME measurements, *Atmos. Chem. Phys. Discuss.*, 1, 411-438, 2001.

Lawrence, M. G., *et al.*, A model for studies of tropospheric photochemistry: Description, global distributions, and evaluation, *J. Geophys. Res.*, 104, 26245-26277, 1999.

Lelieveld, J., and F. J. Dentener, What controls tropospheric ozone? *J. Geophys. Res.*, 105(D3), 3531-3551, 2000.

Leue, C., *et al.*, Quantitative analysis of NO<sub>x</sub> emissions from Global Ozone Monitoring Experiment satellite image sequences, *J. Geophys. Res.*, 106(D6), 5493- 5505, 2001.

Levy, H., *et al.*, Simulated tropospheric NO<sub>x</sub>: Its evaluation, global distribution and individual source contributions, *J. Geophys. Res.*, 104, 26279-26306, 1999.

Li, Q. B., *et al.*, Outflow pathways for North American pollution in summer: A global 3-D model analysis of MODIS and MOPITT observations, *J. Geophys. Res.*, 110, D10301, doi:10.1029/12004JD005039, 2005.

Li, Q., *et al.*, Export of NO<sub>y</sub> from the North American boundary layer: Reconciling aircraft observations and global model budgets, *J. Geophys. Res.*, 109, D02313, doi:10.1029/2003JD004086, 2004.

Liang, J., *et al.*, Seasonal budgets of reactive nitrogen species and ozone over the United States, and export fluxes to the global atmosphere, *J. Geophys. Res.*, 103, 13435-13450, 1998.

Lin, C., D. J. Jacob, W. Munger, and A. Fiore, Increasing background ozone in surface air over the United States, *Geophys. Res. Lett.*, 27, 3465–3468, 2000.

Lin, X., B.A. Ridley, J. Walega, G.F. Hubler, S.A. McKeen, E.-Y. Hsie, M. Trainer, F.C. Fehsenfeld, and S.C. Liu, Parameterization of subgrid scale convective cloud transport in a mesoscale regional chemistry model, *J. Geophys. Res.* 99, 25615-25630, 1994.

Liu, H. D., D. J. Jacob, I. Bey, and R. M. Yantosca, Constraints from  $^{210}\text{Pb}$  and  $^7\text{Be}$  on wet deposition and transport in a global three-dimensional chemical transport model derived by assimilated meteorological files, *J. Geophys. Res.*, 106(D11), 12109-12128, 2001.

Liu, S. C., *et al.*, Sources of Reactive Nitrogen in the Upper Troposphere During SONEX, *J. Geophys. Res.*, 26, 2441-2444, 1999.

Logan, J. A., An analysis of ozonesonde data for the troposphere: Recommendations for testing 3-D models and development of a gridded climatology for tropospheric ozone, *J. Geophys. Res.*, 104(D13), 16115-16149, 1999.

Luo, M., *et al.*, Comparison of carbon monoxide measurements by TES and MOPITT – the influence of a priori data and instrument characteristics on nadir atmospheric species retrievals, *J. Geophys. Res.*, 112, D09303, doi:10.1029/2006JD007663, 2007.

Marenco, A., *et al.*, Measurement of ozone and water vapor by Airbus in-service aircraft: The MOZAIC airborne program, An overview, *J. Geophys. Res.*, 103, 25631-25642, 1998.

Martin, R. V., *et al.*, An improved retrieval of tropospheric nitrogen dioxide from GOME, *J. Geophys. Res.*, 107(D20), 4437, doi:4410.1029/2001JD001027, 2002.

Martin, R. V., *et al.*, Global inventory of nitrogen oxide emissions constrained by space-based observations of  $\text{NO}_2$  columns, *J. Geophys. Res.*, 108(D17), 4537, doi:4510.1029/2003JD003453, 2003a.

Martin, R. V., *et al.*, Global and seasonal decreases in tropospheric oxidants from photochemical effects of aerosols, *J. Geophys. Res.*, 108(D3), 4097, doi:4010.1029/2002JD002622, 2003b.

Martin, R. V., *et al.*, Evaluation of space-based constraints on global nitrogen oxide emissions with regional aircraft measurements over and downwind of eastern North America, *J. Geophys. Res.*, 111, D15308, doi:15310.11029/12005JD007780, 2006.

Mauldin, R.L., E. Kosciuch, B. Henry, F.L. Eisele, R. Shetter, B. Lefer, G. Chen, D. Davis, G. Huey, and D. Tanner, Measurements of OH,  $\text{HO}_2+\text{RO}_2$ ,  $\text{H}_2\text{SO}_4$ , and MSA at the south pole during ISCAT 2000, *Atmos. Env.*, 38 (32), 5423-5437, 2004.

- Mauldin, R.L., F.L. Eisele, D.J. Tanner, E. Kosciuch, R. Shetter, B. Lefer, S.R. Hall, J.B. Nowak, M. Buhr, G. Chen, P. Wang, and D. Davis, Measurements of OH, H<sub>2</sub>SO<sub>4</sub>, and MSA at the South Pole during ISCAT, *Geophys. Res. Lett.*, 28 (19), 3629-3632, 2001.
- McKeen, S. A., *et al.*, A regional model study of the ozone budget in the eastern United States, *J. Geophys. Res.*, 96(D6), 10809-10846, 1991.
- McKeen, S. A., *et al.*, Ozone production from Canadian wildfires during June and July of 1995, *J. Geophys. Res.*, 107, ACH7-1, 2002.
- Merrill, J.T., M. Uematsu, and R. Bleck, Meteorological analysis of long range transport of mineral aerosols over the North Pacific. *J. Geophys. Res.*, 94, 8584–8598, 1989.
- Mickley, L. J., *et al.*, Radiative forcing from tropospheric ozone calculated with a unified chemistry-climate model, *J. Geophys. Res.*, 104, 30153-30172, 1999.
- Nedelec, P., *et al.*, An improved Infra-Red Carbon Monoxide Analyser for Routine Measurements aboard Commercial Airbus Aircraft: Technical Validation and First Scientific Results of the MOZAIC III Program, Atmospheric Chemistry and Physics, 1551-1564, 2003.
- Neff, W., D. Helmig, A. Grachev, and D. Davis, A study of boundary layer behavior associated with high NO concentrations at the South Pole using minisodar, tethered balloon, and sonic anemometer, submitted to *Atmos. Env.*, 2007.
- Newchurch, M. J., *et al.*, Vertical distribution of ozone at four sites in the United States, *J. Geophys. Res.*, 108(D1), 4031, doi:4010.1029/2002JD002059, 2003.
- NRC, Rethinking the Ozone Problem in Urban and Regional Air Pollution, Natl. Acad., Washington D. C., 1991.
- Nunnermacker, L. J., *et al.*, Characterization of the Nashville Urban Plume on July 3 and July 18, *J. Geophys. Res.*, 103, 28129-28148, 1998.
- Ott, L. E., *et al.*, Trace gas transport and lightning NO<sub>x</sub> production during a CRYSTAL-FACE thunderstorm simulated using a 3-D cloud-scale chemical transport model, *Eos Trans. AGU*, 84(86), Fall Meet. Suppl., Abstract AE32A-0156, 2003.
- Palmer, P. I., *et al.*, Air mass factor formulation for spectroscopic measurements from satellites: Application to formaldehyde retrievals from the Global Ozone Monitoring Experiment, *J. Geophys. Res.*, 106, 14539-14550, 2001.
- Palmer, P. I., *et al.*, Inverting for emissions of carbon monoxide from Asia using aircraft observations over the western Pacific, *J. Geophys. Res.*, 108, 8828, doi:10.1029/2003JD003397, 2003.

Pan, L., *et al.*, Retrieval of tropospheric carbon monoxide for the MOPITT experiment, *J. Geophys. Res.*, 103(D24), 32277-32290, 1998.

Pan, L., *et al.*, Satellite remote sensing of tropospheric CO and CH<sub>4</sub>: forward model studies of the MOPITT instrument, *J. Geophys. Res.*, 34(30), 6976, 1995.

Park, R. J., *et al.*, Global simulation of tropospheric ozone using the University of Maryland Chemical Transport Model (UMD-CTM): 1. Model description and evaluation, *J. Geophys. Res.*, 109, D09301, doi:09310.01029/02003JD004266, 2004a.

Park, R. J., *et al.*, Global simulation of tropospheric ozone using the University of Maryland Chemical Transport Model (UMD-CTM): 2. Regional transport and chemistry over the central United States using a stretched grid, *J. Geophys. Res.*, 109, D09303, doi:09310.01029/02003JD004269, 2004b.

Parrish, D.D., *et al.*, Indications of photochemical histories of Pacific air masses from measurements of atmospheric trace species at Point Arena, California, *J. Geophys. Res.*, 97, 15883-15901, 1992.

Pickering, K. E. *et al.*, Trace gas transport in the vicinity of frontal convective clouds, *J. Geophys. Res.*, 93, 759-773, 1988.

Pickering, K. E., *et al.*, Vertical distributions of lightning NO<sub>x</sub> for use in regional and global chemical transport models, *J. Geophys. Res.*, 103(D23), 31203- 31216, 1998.

Price, C., and D. Rind, What determines the cloud-to-ground lightning fraction in thunderstorms? *J. Geophys. Res.*, 98, 463-466, 1993.

Price, C., *et al.*, NO<sub>x</sub> from lightning 1. Global distribution based on lightning physics, *J. Geophys. Res.*, 102(D5), 5929-5941, 1997.

Price, C., Evidence for a link between global lightning activity and upper tropospheric water vapor, *Nature*, 406, 290-293, 2000.

Pryor, S. C., A case study of emission changes and ozone responses, *Atmos. Env.*, 32, 123-131, 1998.

Rao, S. T., *et al.*, Sensitivity of the Urban Airshed Model to mixing height profile, paper presented at Eight Joint Conf. on Applications of Air Pollution Meteorology with A&WMA, Amer. Meteor. Soc., Nashville, TN, 1994.

Rao, S. T., *et al.*, Summertime characteristic of the atmospheric boundary layer and relationships to ozone levels over the eastern United States, *Pure and Applied Geophysics*, 160, 21-55, 2003.

Richter, A., and J. P. Burrows, Tropospheric NO<sub>2</sub> from GOME measurements, *Adv. Space Res.*, 29(11), 1673-1683, 2002.

Ridley, B., J. Walega, D. Montzka, F. Grahek, E. Atlas, F. Flocke, V. Stroud, J. Deary, A. Gallant, H. Boudries, J. Bottenheim, K. Anlauf, D. Worthy, A.L. Sumner, B. Splawn, and P. Shepson, Is the Arctic surface layer a source and sink of NO<sub>x</sub> in winter/spring?, *J. Atmos. Chem.*, 36 (1), 1-22, 2000.

Rind, D., Just add water vapor, *Science*, 281, 1152-1153, 1998.

Roehl, C. M., S. A. Nizkorodov, H. Zhang, G. A. Blake, and P. Wennberg, Photodissociation of peroxyntitric acid in the near-IR, *J. Phys. Chem. A*, 106, 3766-3772, 2002.

Salby, M. L., Fundamentals of Atmospheric Physics, Academic Press, 1996.

Schubert, S. D., *et al.*, An assimilated data set for earth science applications, *Bull. Amer. Meteorol. Soc.*, 74, 2331-2342, 1993.

Seinfeld, J.H. and S.N. Pandis, Atmospheric Chemistry and Physics, John Wiley & Sons, New York, 1998.

Simpson, R. S., *et al.*, adiation-transfer modeling of snow-pack photochemical processes during ALERT2000, *Atmos. Env.*, 36, 2663-2670, 2002.

Singh, H. B., *et al.*, SONEX airborne mission and coordinated POLINAT-2 activity: overview and accomplishments, *Geophys. Res. Lett.*, 26, 3053-3056, 1999.

Sistla, G., *et al.*, Effects of uncertainties in meteorological inputs on urban airshed model predictions and ozone control strategies, *Atmos. Env.*, 30, 2011-2025, 1996.

Slusher, D.L., S.J. Pitteri, B.J. Haman, D.J. Tanner, and L.G. Huey, A chemical ionization technique for measurement of pernitric acid in the upper troposphere and the polar boundary layer, *Geophys. Res. Lett.*, 28 (20), 3875-3878, 2002.

Soden, B. J., Enlightening water vapour, *Nature*, 406, 247-248, 2000.

Song, C. H., and G. R. Carmichael, A three-dimensional modeling investigation of the evolution processes of dust and sea-salt particles in east Asia, *J. Geophys. Res.*, 106(D16), 18131-18154, 2001.

Spichtinger, N., M. Wenig, P. James, T. Wagner, U. Platt, and A. Stohl (2001), Satellite detection of a continental-scale plume of nitrogen oxides from boreal forest-fires, *Geophys. Res. Lett.*, 28, 4579-4582, 2001.

Spurr, R. J. D., *et al.*, A linearized discrete ordinate radiative transfer model for atmospheric remote sensing retrieval, *J. Quant. Spectrosc. Radiat. Transfer*, 68, 689-735, 2001.

Stauffer, D. R., *et al.*, Use of four-dimensional data assimilation in a limited-area mesoscale model part II. Effects of data assimilation within the planetary boundary layer, *Mon. Weather Rev.*, 119, 734-754, 1991.

Stephens, G., *et al.*, Radiation profiles in extended water cloud III: Observations, *J. Atmos. Sci.*, 35, 2133-2141, 1978.

Stohl, A., A 1-year Lagrangian “climatology” of airstreams in the Northern Hemisphere troposphere and lowermost stratosphere, *J. Geophys. Res.*, 106, 7263-7279, 2001.

Thomas, W., E. Hegels, S. Slijkhuis, R. Spurr, and K. Chance, Detection of biomass burning combustion products in Southeast Asia from backscatter data taken by the GOME spectrometer, *Geophys. Res. Lett.*, 25, 1317–1320, 1998

Thompson, A. M., *et al.*, Convective transport over the central United States and its role in regional CO and ozone budgets, *J. Geophys. Res.*, 99, 18,703– 18,711, 1994

Thouret, V., *et al.*, Ozone climatologies at 9-12 km altitude as seen by the MOZAIC airborne program between September 1994 and August 1996, *J. Geophys. Res.*, 103, 25653-25679, 1998.

Thouret, V., *et al.*, Tropopause referenced ozone climatology and inter-annual variability (1994-2003) from the MOZAIC program, *Atmos. chem. phys.*, 6, 1033-1051, 2006.

Van Noije, T. P. C., *et al.*, Multi-model ensemble simulations of tropospheric NO<sub>2</sub> compared with GOME retrievals for the year 2000, *Atmos. chem. phys.*, 6, 2943-2979, 2006.

Velders, G. J. M., *et al.*, Global tropospheric NO<sub>2</sub> column distributions: Comparing 3-D model calculations with GOME measurements, *J. Geophys. Res.*, 106, 12643-12660, 2001.

Volz-Thomas, A., *et al.*, Measurements of total odd nitrogen (NO<sub>y</sub>) aboard MOZAIC in-service aircraft: instrument design, operation and performance, *Atmos. chem. phys.*, 5, 583-595, 2005.

Walcek, C. J., Minor flux adjustment near mixing ratio extremes for simplified yet highly accurate monotonic calculation of tracer advection, *J. Geophys. Res.*, 105, 9335–9348, 2000.

Wang, H.-J., *et al.*, Assessment of SAGE version 6.1 ozone data quality, *J. Geophys. Res.*, 107, 4691, doi:10.1029/2002JD002418, 2002.

Wang, H.-J., *et al.*, SAGE III solar ozone measurements: Initial results, *Geophys. Res. Lett.*, 33, L03805, doi:10.1029/2005GL025099, 2006.

Wang, Y. X., M. B. McElroy, T. Wang, and P. I. Palmer, Asian emissions of CO and NO<sub>x</sub>: Constraints from aircraft and Chinese station data, *J. Geophys. Res.*, *109*, doi:10.1029/2004JD005250, 2004.

Wang, Y., *et al.*, Global simulation of tropospheric O<sub>3</sub>-NO<sub>x</sub>-hydrocarbon chemistry: 1. Model formulation, *J. Geophys. Res.*, *103*, 10713-10725, 1998.

Wang, Y., *et al.*, Factors Controlling Tropospheric O<sub>3</sub>, OH, NO<sub>x</sub>, and SO<sub>2</sub> over the Tropical Pacific during PEM-Tropics B, *J. Geophys. Res.*, *106*, 32,733-32,748, 2001.

Wang, Y., *et al.*, Intercontinental transport of pollution manifested in the variability and seasonal trend of springtime O<sub>3</sub> at northern mid and high latitudes, *J. Geophys. Res.*, *108*, D21, 4683, 10.1029/2003JD003592, 2003b.

Wang, Y., *et al.*, Springtime photochemistry at northern mid and high latitudes, *J. Geophys. Res.*, *108*, 8358, doi:10.1029/2002JD002227, 2003a.

Wang, Y., Y. Choi, T. Zeng, B. Ridley, N. Blake, D. Blake, and F. Flocke, Late-spring increase of trans-Pacific pollution transport in the upper troposphere, *Geophys. Res. Lett.*, *33*, L01811, doi:10.1029/2005GL024975, 2006.

Wang, Y., Y. Choi, T. Zeng, D. Davis, M. Buhr, G. Huey, and W. Neff, Assessing the photochemical impact of snow NO<sub>x</sub> emissions over Antarctica during ANTICI 2003, submitted to *Atmos. Env.*, 2007.

Weele, M.V. and Duynkerke, P. G., Effects of Clouds on the Photodissociation of NO<sub>2</sub>: Observations and Modeling, *J. Atmos. Chem.*, *16*, 231-255, 1993.

Weiss-Penzias, P., D. A. Jaffe, L. Jaegle', and Q. Liang, Influence of long-range-transported pollution on the annual and diurnal cycles of carbon monoxide and ozone at Cheeka Peak Observatory, *J. Geophys. Res.*, *109*, D23S14, doi:10.1029/2004JD004505, 2004.

Wesely, M.L., Parameterization of surface resistance to gaseous dry deposition in regional-scale numerical models, *Atmos. Environ.*, *23*, 1293-1304, 1989.

Wild, O., Q. Zhu, and M.J. Prather, Fast-J: Accurate simulation of in- and below-cloud photolysis in global chemical models, *J. Atmos. Chem.*, *37*, 245-282, 2000.

Wolff, E. W., A. E. Jones, T. J. Martin, and T. C. Grenfell, Modelling photochemical NO<sub>x</sub> production and nitrate loss in the upper snowpack of Antarctica, *Geophys. Res., Lett.*, *29*, 1944, doi:10.1029/2002GL015823, 2002.

Worden, H. M., *et al.*, Comparisons of Tropospheric Emission Spectrometer (TES) ozone profiles to ozonesonde: Methods and initial results, *J. Geophys. Res.*, 112, D03309, doi:10.1029/2006JD007258, 2007.

Yang, Q., D.M. Cunnold, H.-J. Wang, and L. Froidevaux, Mid-latitude Tropospheric Ozone Columns Derived from Aura OMI and MLS data Using the TOR Approach and Mapping Techniques, submitted to *J. Geophys. Res.*, 2007.

Yienger, J. J., and H. Levy II, Empirical model of global soil-biogenic NO<sub>x</sub> emissions, *J. Geophys. Res.*, 100, 11447-11464, 1995.

Zeng, T., Y. Wang, K. Chance, E. V. Browell, B. A. Ridley, and E. L. Atlas, Widespread persistent near-surface ozone depletion at northern high latitudes in spring, *Geophys. Res. Lett.*, 30, 2298, 10.1029/2003GL018587, 2003.

Zeng, T., Y. Wang, K. Chance, N. Blake, D. Blake, and B. Ridley, Halogen-driven low altitude O<sub>3</sub> and hydrocarbon losses in spring at northern high latitudes, *J. Geophys. Res.*, 111, D17313, doi:10.1029/2005JD006706, 2006.

Zhang, X., *et al.*, Numerical modeling of lightning-produced NO<sub>x</sub> using an explicit lightning scheme:1. Two-dimensional simulation as a "proof of concept", *J. Geophys. Res.*, 108(D18), 4579, 2003.

Zhang D. and Anthes R. A., A high-resolution model of the planetary boundary layer: sensitivity tests and comparisons with SESAME-79 data, *J. Appl. Meteor.*, 21, 1594-1609, 1982.

Ziemke, J. R., *et al.*, Tropospheric ozone determined from Aura OMI and MLS: Evaluation of measurements and comparison with the Global Initiative's Chemical Transport Model, *J. Geophys. Res.*, 111, D19303, doi:10.1029/2006JD007089, 2006.